UNIVERSIDADE FEDERAL DE PERNAMBUCO
DEPARTAMENTO DE FÍSICA – CCEN
PROGRAMA DE PÓS-GRADUAÇÃO EM FÍSICA

VICTOR MANUEL MARTINEZ ALVAREZ

TOPOLOGICAL AND STRONGLY CORRELATED PHASES IN LOW-DIMENSIONAL SYSTEMS

Recife
2019

VICTOR MANUEL MARTINEZ ALVAREZ

TOPOLOGICAL AND STRONGLY CORRELATED PHASES IN LOW-DIMENSIONAL SYSTEMS

Tese apresentada ao Programa de Pós-Graduação em Física da Universidade Federal de Pernambuco, como requisito parcial para a obtenção do título de Doutor em Física.

Área de Concentração: Física Teórica e Computacional

Orientador: Prof. Maurício Domingues Coutinho Filho

Recife
2019

Catalogação na fonte
Bibliotecária Elaine Freitas CRB4-1790

M385t Martinez Alvarez, Victor Manuel
Topological and strongly correlated phases in low-dimensional systems/ Victor Manuel Martinez Alvarez. – 2019.
104 f.: fig.

Orientador: Maurício Domingues Coutinho Filho.
Tese (Doutorado) – Universidade Federal de Pernambuco. CCEN. Física. Recife, 2019.
Inclui referências e apêndices.

1. Fisíca Teórica. 2. Ferrimagnetismo. 3. Sistemas de baixa dimensionalidade. I. Coutinho Filho, Maurício Domingues (orientador). II. Título.

530.1 CDD (22. ed.) UFPE-FQ 2019-14

VICTOR MANUEL MARTINEZ ALVAREZ

TOPOLOGICAL AND STRONGLY CORRELATED PHASES IN LOW-DIMENSIONAL SYSTEMS

Tese apresentada ao Programa de Pós-Graduação em Física da Universidade Federal de Pernambuco, como requisito parcial para a obtenção do título de Doutor em Física.

Aprovada em: 22/02/2019.

BANCA EXAMINADORA

_____
Prof. Maurício Domingues Coutinho Filho
Orientador
Universidade Federal de Pernambuco

_____
Prof. Ernesto Carneiro Pessoa Raposo
Examinador Interno
Universidade Federal de Pernambuco

_____
Prof. Renê Rodrigues Montenegro Filho
Examinador Externo
Universidade Federal de Pernambuco

_____
Prof. Fernando Jorge Sampaio Moraes
Examinador Externo
Universidade Federal Rural de Pernambuco

_____
Prof. Mucio Amado Continentino
Examinador Externo
Centro Brasileiro de Pesquisas Físicas

In memory of my beloved grandmother and favorite person.
Asunción Carmona (La Niña).

1929 – 2015

I would like to dedicate this thesis to the two most incredible mothers I know, mamá and mivi. Without you, none of this would be possible.
Especially to my son, Victor Manuel Martinez Leon, the light of my life.

ACKNOWLEDGEMENTS

First I would like to thank Prof. Mauricio D. Coutinho Filho for giving me the opportunity to work in his group. I thank him for teaching me the meaning of being a Physicist! I admire him for his willingness to share and inspire with his unending enthusiasm for physics.

I wish to thank Prof. Renê Montenegro, for interesting discussions on various topics of this Thesis.

Also, I wish to thanks Prof. Luis E. F. Foa Torres from Departamento de Física, Universidad de Chile. Thanks for sharing your time and knowledge to teach me how to be a good theoretical physicist; I can say that I have benefited greatly from your advice. Luis, thank you so much for all!

I would like to thank all the staff of the Department of Physics at UFPE, for supporting this work with their valuable time and energy. Thanks also to all my colleagues (past and present) at the Department of Physics, UFPE. It was a pleasure to work with you all.

My special words of thanks should also go to my colleagues and friends during my Ph.D. studies. Your presence make this environment more pleasant for me.

My special thanks to Alexis and Yoandris, "*el Pikete*", for more than 10 years of friendship. Thank you for all the days you be there for me.

I am also very thankful to my friends all over the world. You know that you are always present in my heart.

I wish to thank Thais, for all the support and understanding during the completion of this Thesis.

My whole heart and love go to my mom, Ana Luisa Alvarez Carmona for all love and support in every moment of my life no matter if we're close or far. Her infallible love and support have always been my strength. Your sacrifice will remain my inspiration throughout my life.

Especially my grandmother, Asunción Carmona, there are no words to express everything I feel for you.

I am also very much grateful to all my family members, in special my brother Pedro Pablo and my uncle Alberto Calletano.

I am also very much grateful to Iraida and Aylin, who are part of my family forever. Thank you for your love, support and understanding during all this time.

Last but not least, I dedicate this thesis to my son, Victor Manuel, the most special person in my life.

ABSTRACT

In the first part of the present Thesis, the ground state (GS) properties of the quasi-one-dimensional AB_2 Hubbard model are investigated taking the effects of charge and spin quantum fluctuations on equal footing. Using a functional integral approach, combined with a perturbative expansion in the strong-coupling regime, we obtain the Lagrangian density associated with the charge (Grassmann fields) and spin [$SU(2)$ gauge fields] degrees of freedom. In the strong-coupling regime, we derive a perturbative low-energy theory suitable to describe the ferrimagnetic phase at half filling and the phases in the hole-doped regime. At half filling, a perturbative spin-wave analysis allows us to find the GS energy, sublattice magnetizations, and total spin per unit cell in the Lieb ferrimagnetic GS of the effective quantum Heisenberg model, in very good agreement with previous results. In the challenging hole doping regime away from half filling, we derive the corresponding *t-J* Hamiltonian. Under the assumption that charge and spin quantum correlations are decoupled, the evolution of the second-order spin-wave modes in the doped regime unveils the occurrence of spatially modulated spin structures and the emergence of phase separation in the presence of resonating-valence-bond (RVB) states. We also calculate the doping-dependent GS energy and total spin per unit cell, including both Zeeman and orbital contributions, in which case it is shown that the spiral ferrimagnetic order collapses at a critical hole concentration. Notably, our analytical results in the doped regime are in very good agreement with density matrix renormalization group (DMRG) studies, where our assumption of spin-charge decoupling is numerically supported by the formation of charge-density waves in anti-phase with the modulation of the magnetic structure. In the second part, motivated by analogy with photonic lattices, we examine the edge states of a one-dimensional trimer lattice in the phases with and without inversion symmetry protection. In contrast to the Su-Schrieffer-Heeger model, we show that the edge states in the inversion-symmetry broken phase of the trimer model turn out to be chiral, i.e., instead of appearing in pairs localized at opposite edges they can appear at a single edge. Interestingly, these chiral edge states remain robust to large amounts of disorder. In addition, we use the Zak phase to characterize the emergence of degenerate edge states in the inversion-symmetric phase of the trimer model. Furthermore, we capture the essentials of the whole family of trimers through a mapping onto the commensurate off-diagonal Aubry-André-Harper model, which allows us to establish a direct connection between chiral edge modes in the two models, including the calculation of Chern numbers. We thus suggest that the chiral edge modes of the trimer lattice have a topological origin inherited from this effective mapping. Also, we find a nontrivial connection between the topological phase transition point in the trimer lattice and the one in its associated two-dimensional parent system, in agreement with results in the

context of Thouless pumping in photonic lattices.

Keywords: Ferrimagnetism. Low-dimensional systems. Strongly-correlated electron systems. Edge states. Topological insulator.

RESUMO

Na primeira parte da presente Tese, as propriedades do estado fundamental do modelo de Hubbard na rede quase-unidimensional AB_2 foram investigadas considerando os efeitos das flutuações quânticas de carga e spin em pé de igualdade. Usando uma abordagem de integral funcional, combinada com uma expansão perturbativa no limite de acoplamento forte, obtivemos a densidade de Lagrangiana associada aos graus de liberdade de carga (campos de Grassmann) e de spin [campos de calibre $SU(2)$]. No regime de acoplamento forte derivamos uma teoria perturbativa de baixa energia, adequada para descrever a fase ferrimagnética no regime de banda semi-cheia e as fases no regime dopado por buracos (ausência de elétrons). No regime de banda semi-cheia, uma análise perturbativa das ondas de spin (excitações magnéticas) nós permitiu encontrar a energia do estado fundamental, as magnetizações das subredes e o spin total por célula unitária no estado fundamental ferrimagnético de Lieb do modelo efetivo quântico de Heisenberg, em muita boa concordância com resultados anteriores. No desafiante regime dopado por buracos fora da banda semi-cheia derivamos o correspondente Hamiltoniano *t-J*. Sob a hipótese de que as correlações quânticas de carga e spin estão desacopladas, a evolução dos modos de ondas de spin, em segunda ordem de perturbação no regime dopado, revela a ocorrência de estruturas de spin espacialmente moduladas e o surgimento da separação de fases na presença de estados de ligação de valência ressonante (RVB). Também calculamos a energia do estado fundamental dependente da dopagem e o spin total por célula unitária, incluindo tanto as contribuições tipo Zeeman quanto as orbitais, caso em que é mostrado que a ordem espiral magnética colapsa em uma concentração crítica de buracos. Destacamos que nossos resultados analíticos no regime dopado estão em muita boa concordância com estudos numéricos de grupos de renormalização de matriz de densidade (DMRG), onde nossa suposição de desacoplamento de spin-carga é evidenciada pela formação de ondas de densidade de carga em anti-fase com a modulação da estrutura ferrimagnética. Na segunda parte, com motivação na analogia com redes fotônicas, examinamos os estados de borda de uma rede unidimensional trimerizada nas fases com e sem proteção de simetria de inversão. Em contraste com o modelo Su-Schrieffer-Heeger, mostramos que os estados de borda na fase com quebra de simetria de inversão do modelo do trímero se revelam quirais, ou seja, em vez de aparecerem em pares localizados em bordas opostas eles podem aparecer em uma borda só. Destacamos que esses estados de borda quirais permanecem robustos a fortes amplitudes de desordem aleatória. Além disso, usamos a fase de Zak para caracterizar o surgimento de estados de borda degenerados na fase com simetria de inversão do modelo de trímeros. Por outro lado, nós capturamos os fundamentos de toda a família de trímeros através de um mapeamento no modelo de Aubry-André-Harper não diagonal, que permite estabelecer uma conexão direta entre

os modos de borda quirais nos dois modelos, incluindo o cálculo dos números de Chern. Neste contexto, sugerimos que os modos de borda quirais da rede trimerizada têm uma origem topológica herdada deste mapeamento efetivo. Além disso, encontramos uma conexão não trivial entre o ponto de transição da fase topológica na rede trimerizada e aquela do sistema bidimensional associado, em concordância com resultados no contexto de bombeamento de Thouless em redes fotônicas.

Palavras-chaves: Ferrimagnetismo. Sistemas de baixa dimensionalidade. Sistemas de elétrons fortemente correlacionados. Estados da borda. Isolante topológico.

LIST OF FIGURES

CONTENTS

1 STRONGLY CORRELATED PHASES IN AB_2 HUBBARD CHAINS

1.1 Strongly correlated many-particle systems

Understanding the novel properties of different phases of matter and explaining the new collective behaviors that emerge when many degrees of freedom interact is a central goal of condensed matter physics. However, despite the great technological and experimental advances achieved so far, the study of many-body systems remains an extremely difficult task, mainly because of the large number of quantum particles interfering with each other, which in consequence produces states that are much more than the simple sum of its constituent parts. From this point of view, fundamentally new types of phenomena emerge within complex assemblies of particles which cannot be predicted from an *a priori* knowledge of the quantum laws of nature. The essence of the concept of emergence was captured in the influential paper entitled "More is different", written in 1972 (1) by the Nobel laureate in Physics, Philip W. Anderson, where he wrote:

> "The behavior of large and complex aggregations of elementary particles, it turns out, is not to be understood in terms of a simple extrapolation of the properties of a few particles. Instead, at each level of complexity entirely new properties appear, and the understanding of the new behaviors requires research which I think is as fundamental in its nature as any other".

In addition, it is known that phase transitions are a key sign of emergent behavior. During the last decades, much attention has been given to a special class of phase transitions that occur at absolute zero temperature, known as quantum phase transitions (QPT) (2, 3, 4). These are phenomena characterized by the change of the nature of the ground state (GS) driven by a non-thermal parameter such as: pressure, magnetic field, doping, Coulomb repulsion, or competitive interactions. More specifically, they are driven by quantum fluctuations since there are no thermal fluctuations at $T = 0\,\mathrm{K}$.

Quantum fluctuations become increasingly important as the dimensionality of the system is reduced. In this context, low-dimensional systems, in which one or more spatial dimensions are small enough to consider the quantum mechanical wave function restricted or confined, exhibit some of the most diverse and fascinating physical phenomena seen in all of condensed matter physics. Furthermore, low-dimensional models are the perfect place to explore the effects of strong correlations.

Now, because our daily experience shows us that we live in a three-dimensional world, the study of low-dimensional systems was initially seen as a "laboratory" for the development of theories that would later be applied to three-dimensional systems. However, these systems present several symmetries that their low-dimensional analogs do not; hence exhibiting some different characteristics. As an example, we can mention the Fermi liquid theory (5), which describes most metals in three dimensions, but fails when applied to one-dimensional systems (6) due to the infrared divergence. Also, as mentioned before, quantum and thermal fluctuations are more pronounced in low-dimensional systems, which favors the appearance of new phenomena and phases, with remarkable experimental realizations, that have no counterpart in three-dimensional systems.

On the other hand, even with the simplicity of one-dimensional (1D) systems, exact solutions of many-body models are not always possible, and in some cases, when obtained, the connection with the observed characteristics is not a trivial task. This limitation encouraged the development of various analytical and numerical techniques to investigate the properties of these systems, which we will explore in the next sections.

1.2 Low-dimensional ferrimagnets

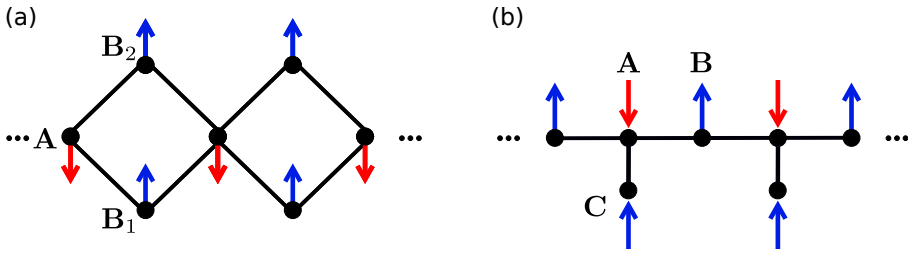

Figura 1 – Scheme representing a finite section of the chains with (a) AB_2 and (b) ABC unit cell topologies (each unit cell contains three sites), as well as the ferrimagnetic order of both chains. The black circles represent the magnetic centers of spin-1/2, whereas the lines illustrate the antiferromagnetic coupling interaction.

The study of low-dimensional systems with ferrimagnetic characteristics (7, 8) has attracted considerable theoretical and experimental interest over the years because of their unique physical properties and very rich phase diagrams (9). Ferrimagnets belong to a class of magnets in which, below a certain critical temperature, spontaneous magnetization is reached due to the antiparallel alignment of magnetic moments in different sublattices and to the near-neighbor antiferromagnetic exchange coupling. We can usually distinguish two major categories of ferrimagnets: those containing different magnetic ions in each sublattice, and ferrimagnets of topological origin, also called topological ferrimagnets, resulting from the topological structure of the unit cell, which has

different number of magnetic sites (see Fig. 1). The majority of these low-dimensional systems are also subject to a strong topological connection, that is, their elements can not change places between them. This fact acquires important consequences in quantum systems, where elementary excitations can be treated as both fermionic or bosonic excitations. In this case, some strongly-interacting boson systems can be mapped onto fermionic systems with simpler interactions and vice versa. This connection can be achieved through bosonization and quasi-particle fermionization techniques (3).

In particular, the GS of quasi-one-dimensional (quasi-1D) quantum ferrimagnets with AB_2 or ABC unit cell topologies (diamond or trimer chains, see illustration in Fig. 1) described by the Heisenberg or Hubbard models (10) exhibit unsaturated spontaneous magnetization, ferromagnetic and antiferromagnetic spin-wave modes, and field-dependent magnetization plateaus, among several other features of interest which we are going to explore next.

Of special interest is the topological origin of the long-range ordered magnetic GS associated with the unit cell structure of the lattice (10, 11, 12, 13, 14, 15, 16, 17, 18). These studies have been motivated and supported by exact solutions and rigorous results (19, 20, 21, 22, 23, 24, 25); in particular, at half filling the total spin per unit cell obeys Lieb-Mattis (19) (Heisenberg model) or Lieb's theorem (21) (Hubbard model). On the other hand, it has been verified that the ferrimagnetic GS of spin-1/2 Heisenberg and Hubbard/t-J AB_2 chains, under the effect of frustration (26, 27, 28, 29, 30) or doping (12, 17, 31, 9), are strongly affected by quantum fluctuations that might cause its destruction and the occurrence of new exotic phases: spiral incommensurate (IC) spin structures, Nagaoka ($U \to \infty$) and resonating-valence-bond (RVB) states, phase separation (PS), and Luttinger-liquid behavior. These features can enhance the phenomenology in comparison with a linear chain, which is dominated by the nontrivial Luttinger-liquid behavior that exhibits fractional excitations (3, 32), emergent fractionalized particles (33), and fractional-exclusion statistic properties (34, 35) in the spin-incoherent regime (36), in which case the Bethe ansatz and the bosonization procedures play a significant role. It is important to remark that a broad class of 1D systems with quantum critical ground state can be described by the mentioned Luttinger quantum liquid theory (34, 35). Last but not least, we mention that the investigations of transport properties in AB_2 chains and related structures (37, 38), as well as exactly solved hybrid diamond chain with localized Ising spins and mobile electrons (39), have also unveiled very interesting features.

1.3 Phenomenological motivation

Over the years a number of compounds have been synthesized which have atoms arranged in the form of quasi-one-dimensional chains. The development of optical

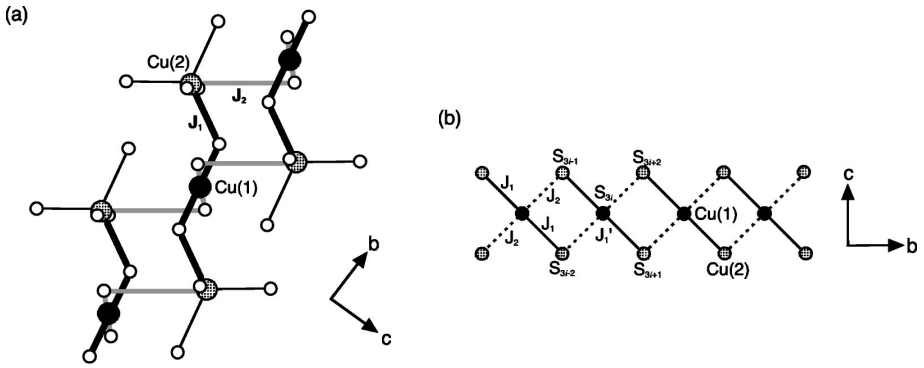

Figura 2 – (a) Trimer chains found in compounds of the family $A_3Cu_3(PO_4)_4$ (A = Ca, Sr, Pb). The large and filled circles represent the Cu^{+2} magnetic moments. The small and open circles represent the oxygen ions. (b) Schematic view of magnetic interactions between copper ions: the intertrimer interaction J_2 is much smaller than the intratimer interactions J_1 and $J_1^{'}$, however, the ferrimagnetic order is observed in these compounds, and the ground state is a state with $S = 1/2$. Taken from Ref. (40).

lattices has also provided several experimental realizations of these low-dimensional systems (7). For instance, in magnetic systems the interactions are determined by the compounds' characteristics: distance between magnetic sites, the superposition between the orbitals, and so on. In this way, each compound represents a system with specific couplings that may undergo some change with the variation of external parameters. Moreover, in optical lattices the interaction between the confined atoms is controlled in a finer way, allowing the study of theoretically predicted phase transitions. Some compounds may have in their crystalline structure 1D chains weakly coupled in comparison with those couplings within the chains, thus allowing the formation of the aforementioned quasi-1D systems.

Experimental studies (41, 42, 40) of the magnetic properties of homometallic phosphate compounds of the family $A_3Cu_3(PO_4)_4$ (A = Ca, Sr, Pb) suggest that in these materials the line of trimers formed by spin-1/2 Cu^{+2} ions antiferromagnetically coupled, as shown in Fig. 2, do exhibit ferrimagnetism of topological origin. Although the intertrimer coupling is much weaker than the intratrimer interaction, the former is sufficient to establish a ferrimagnetic ground state (40). Further, compounds $Ca_3M_3(PO_4)_4$(M = Ni,Co) with a wave-like layer structure built by zigzag M-chains exhibit antiferromagnetic ordering (M = Ni) or paramagnetic behavior (M = Co) (43).

On the other hand, bimetallic compounds, such as $CuMn(S_2C_2O_2)_2 \cdot 7.5H_2O$ (44) shown in Fig. 3, can be modeled (44, 45, 46, 47) by alternate spin-1/2 - spin-5/2 chains and support interesting field-induced quantum critical points and Luttinger-liquid phase (45). In addition, frustrated diamond (AB_2 topology) chains can properly model the compound azurite, $Cu_3(CO_3)_2(OH)_2$ (see Fig. 4), in which case the occurrence of the 1/3 magnetization plateau is verified at high fields (48, 49, 50) in agreement with

topological arguments (51) akin to those invoked in the quantum Hall effect.

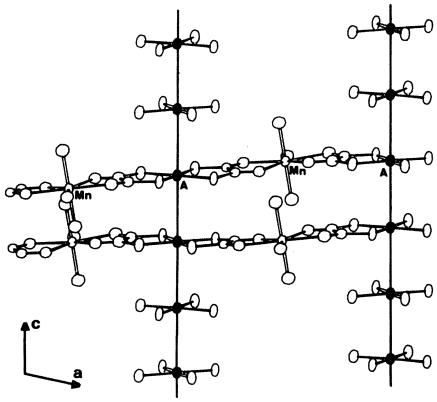

Figura 3 – A partial view of a layer of stacked $\cdots \mathrm{A}\,(\mathrm{S_2C_2O_2})\,\mathrm{Mn}\,(\mathrm{H_2O})_3\,(\mathrm{S_2C_2O_2})\cdots$ chains, emphasizing the structure generated by the AS_4 fragments. A atoms (Cu or Pd) are shown as black ellipsoids. Taken from Ref. (44).

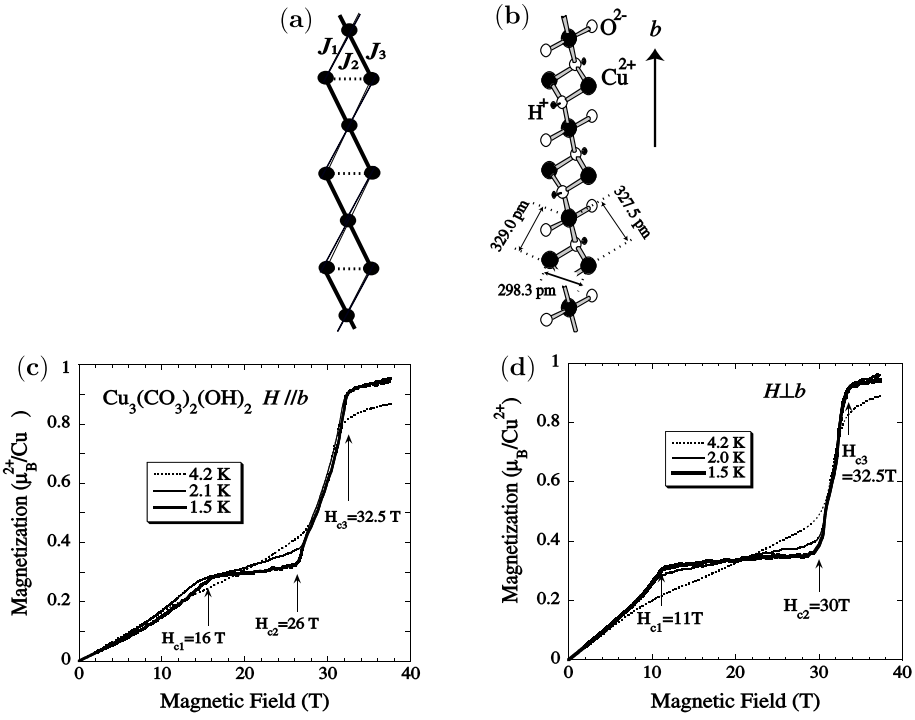

Figura 4 – (a) Schematic view of the distorted diamond chain, where the solid circles represent spin-1/2 coupled by the exchange interactions. (b) Scheme representing the crystal structure of the compound azurite $Cu_3(CO_3)_2(OH)_2$. The panels below show the high field magnetization curves of this compound measured below 4.2 K. The magnetic field was applied along the *b* axis (c) and perpendicular to the *b* axis (d), respectively. Taken from Ref. (48).

The spin-1/2 trimer chain compound $Cu_3(P_2O_6OH)_2$, with antiferromagnetic interactions only, also display the 1/3 magnetization plateau (53). Interestingly, it has been established that in azurite the magnetization plateau is a dimer-monomer state (52) (see

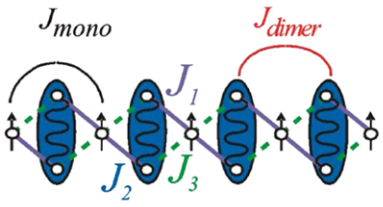

Figura 5 – Dimer-monomer model with microscopic couplings J_1, J_2, J_3, and effective couplings J_{mono}, J_{dimer}, characterizing the plateau phase. Taken from Ref. (52).

Fig 5), i.e., the chain is formed by pairs of $S = 1/2$ monomers and $S = 0$ dimers, with a small local polarization of the diamond spins (54), in agreement with reliable electronic structure calculations using density functional theory (DFT) combined with density matrix renormalization group (DMRG) results (55). These dimer-monomer states have been found previously in the context of modeling frustrated AB_2 chains (56, 57, 58), and confirmed through a modeling using quantum rotors (59).

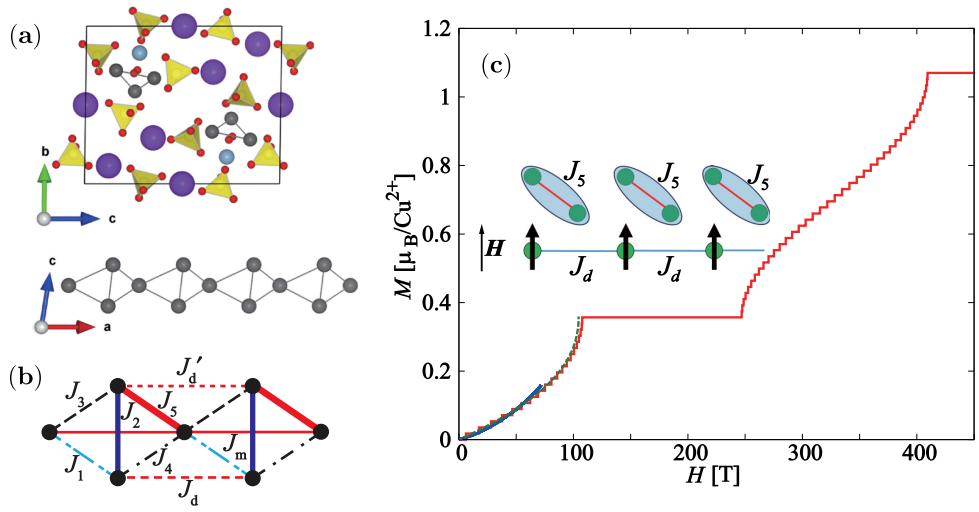

Figura 6 – (a) Schematic view of the crystal structure of $A_3Cu_3AlO_2(SO_4)_4$ (A = K,Rb,Cs). The gray, purple, light blue, and red circles denote Cu, A, Al, and O atoms, respectively. The inequilateral diamond chains run along the a axis. (b) Effective spin model of this compound. The circles represent Cu^{+2} ions with spin $1/2$. The blue broken, dark blue solid, black broken, black dashed-dotted, red thick solid, red thin solid, red dashed, and red dotted lines denote the exchange interactions J_1, J_2, J_3, J_4, J_5, J_m, J_d, and $J_d^{'}$, respectively. (c) Magnetization curve for $K_3Cu_3AlO_2(SO_4)_4$. The red jagged solid line is a calculated curve by density matrix renormalization group (DMRG) at zero temperature for a 120-site periodic chain with the exchange interactions estimated from the spin susceptibility. The blue solid line represents the experimental result under the magnetic field up to 72 T at 4.2 K (60). The green dashed line is the exact magnetization curve for the 1D Heisenberg model. The inset is a schematic view of the spin configuration at the 1/3 plateau with the dimers formed by J_5 and the 1D chain with J_d whose spins are ferromagnetically aligned with the direction of the applied magnetic-field H. Taken from Ref. (61).

In contrast to azurite, whose dimers appear perpendicular to the chain direction, as shown in Fig. 5, in the spin-1/2 inequilateral diamond-chain compounds (61) $A_3Cu_3AlO_2(SO_4)_4$ (A = K,Rb,Cs), the magnetic exchange interactions force the dimers to lie along the sides of the diamond cells and the monomers form a 1D Heisenberg chain, (see Fig. 6 and 7). In fact, the low-energy excitations of these new compounds have been probed and a Tomonaga-Luttinger spin liquid behavior identified (60). It is worth mentioning that strongly frustrated AB_2 chains can exhibit ladder-chain decoupling (27), in which case the ladder is formed via the coupling between dimer spins in neighboring AB_2 unit cells.

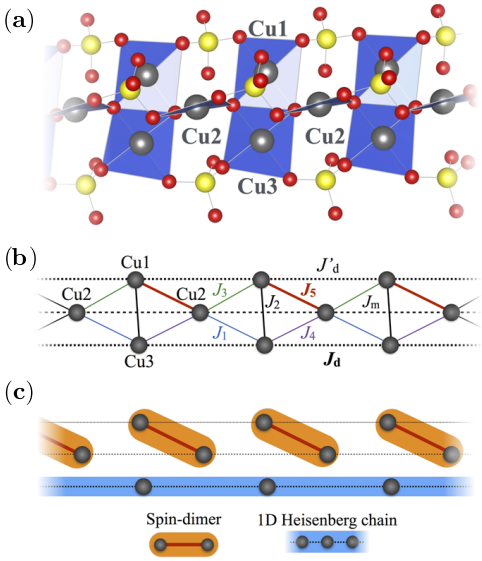

Figura 7 – (a) The diamond chain of $K_3Cu_3AlO_2(SO_4)_4$, which consists of Cu^{+2} ions (grey spheres) along the a-axis with nearby oxygen (red spheres) and sulfur ions (yellow spheres). (b) Effective spin model of this compound with the nearest-neighbor exchange couplings J_i ($i = 1$ to 5), and the next nearest-neighbor exchange couplings of J_m, J_d, and $J_d^{'}$. (c) Schematic view of the spin dimer-monomer ground state configuration for $K_3Cu_3AlO_2(SO_4)_4$. Taken from Ref. (60).

On the other hand, besides the above-mentioned quasi-1D compounds and related magnetic properties, considerable efforts have been devoted to the study of superconductivity and intriguing magnetic/charge ordered phases in doped materials (62, 63), in particular the formation of spin-gapped states in compounds such as the family of doped $(La,Sr,Ca)_{14}Cu_{24}O_{41}$. This compound is formed by one-dimensional CuO_2 diamond chains, (Sr,Ca) layers, and two-leg Cu_2O_3 ladders (64). These results certainly stimulate experimental and theoretical investigations of quasi-1D compounds in the hole-doped regime, which is the main focus of Part I of this Thesis.

Lastly, it is worth mentioning that the effect of quantum fluctuations is most effectively appreciated in a recent study of the Kagome lattice compound $ZnCu_3(OH)_6Cl_2$ (65) under electron doping, in which case, and against theoretical expectations (66, 67), the

quantum spin-liquid phase is robust up to the observed doping-induced systematic suppression of magnetic behavior. More recently, a report (63) on optical doping-induced stable and metastable hidden phases in pristine and doped TaS_2 made possible the in situ visualization through femtosecond electron crystallography. Very interesting features underlying the observed optical-induced charge density wave transitions are discussed in the light of similar thermodynamic transitions induced by chemical doping, pressure and, in particular, temperature. These general trends are corroborated by the observation (68) of hole-doping induced melting of spin-state ordering in the compound $PrBaCo_2O_{5.5+x}$, in concurrence with an insulator metal transition. In fact, the results show that the electronic change is quite the same regardless of whether it is driven by temperature or hole doping.

1.4 General properties of the AB_2 chains

Particular interest centers on the physical properties of low-dimensional strongly-correlated electron systems with AB_2 unit-cell topology, which exhibit unique phases and behaviors with no linear chain (AB) counterparts. In this context, the main purpose of this section is to summarize the most fundamental characteristics of low-dimensional AB_2 chains. The source of information discussed in this Section is mainly from Ref. (9), where the authors studied the magnetic and nonmagnetic phases in doped AB_2 t-J Hubbard chains using data from density matrix renormalization group and exact diagonalization techniques.

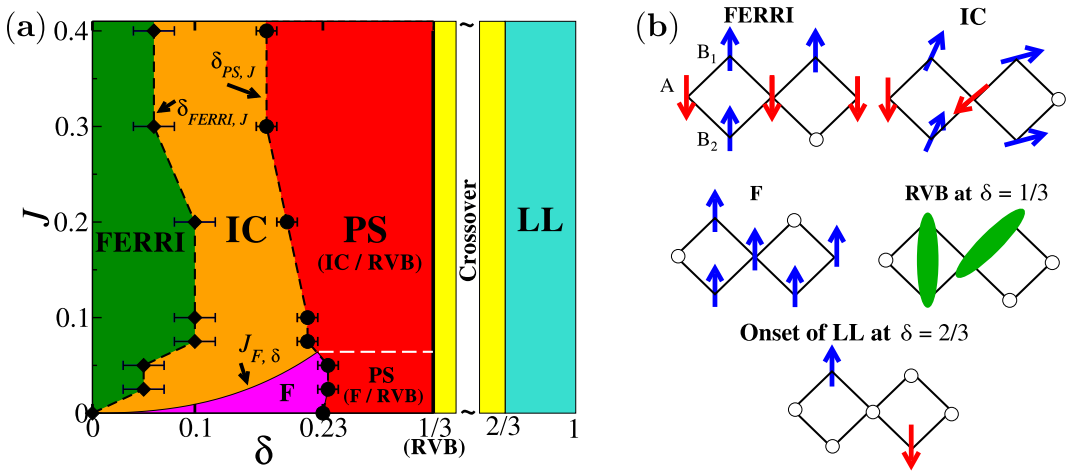

Figura 8 – (a) GS phase diagram for the AB_2 t-J model. The different phases are illustrated in panel (b): modulated ferrimagnetism (FERRI), incommensurate (IC), Nagaoka ferromagnetism (F), short-range resonating valence bond (RVB) states, phase separation (PS), and Luttinger liquid (LL). The estimated transition lines $\delta_{FERRI,J}$, $\delta_{PS,J}$, and $J_{F,\delta}$ are also pointed out. Taken from Ref. (9).

Due to the special unit-cell topology of the AB_2 chain, this system displays a very rich phase diagram (see Fig. 8), as a function of two parameters:

- $J = 4t^2/U$, i.e., the exchange coupling which measures the relative strength between the on-site repulsive Coulomb interaction U and the first-neighbor hopping amplitude t,
- the hole doping concentration, $\delta = 1 - N_e/N = N_h/N$, where N_e (N_h) is the number of electrons (holes) present in the system, such that $N_h = N - N_e$. As a special case, at half filling ($N_e = N$), the hole doping concentration $\delta = 0$.

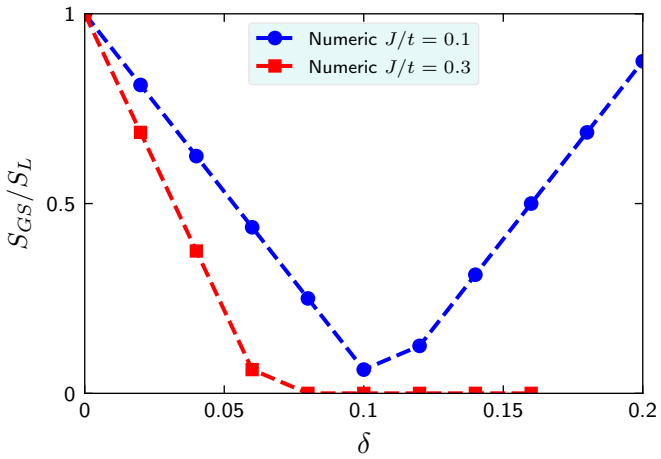

Figura 9 – Ground-state total spin S_{GS} normalized by its value in the undoped regime: $S_L \equiv (N_c/2) - 0.5$, as function of δ for the indicated values of J and $N = 3N_c + 1 = 100$. Adapted from Ref. (9).

As shown in Fig. 8, the rich J vs δ phase diagram of AB_2 chains exhibits regions of modulated ferrimagnetism (FERRI), incommensurate (IC), Nagaoka ferromagnetism (F), short-range resonating valence bond (RVB) states, phase separation (PS), and Luttinger liquid (LL) physics. Notice that at $\delta = 0$ and for any value of J, the insulating Lieb ferrimagnetic state was detected with total spin quantum number $S_{GS} = S_L \equiv N_c/2 - 0.5$, under open boundary conditions and with an A site on each side, where N_c is the number of unit cells. In addition, they also calculated S_{GS} as a function of δ from the energy degeneracy in S^z, with the interest of assessing the stability of this state against doping.

In Fig. 9 we plot the evolution of S_{GS}, normalized by S_L, as a function of δ, using numerical data from DMRG and Lanczos techniques (9), for $J = 0.3$ (red squares) and $J = 0.1$ (blue circles). In the latter (former) case, the system undergoes a phase transition, at a critical value $\delta = \delta_{FERRI,J}$, from the modulated ferrimagnetic phase to an incommensurate phase with zero (nonzero) S_{GS}. In both cases, the transition is characterized by a practically linear decrease of S_{GS} from S_L to 0 or to a residual value, regardless of the value that S_{GS} takes after the transition. However, for low-enough J, S_{GS} of the IC phase increases linearly with δ up to $\delta = \delta_{PS,J}$, the line at which PS occurs [see Fig. 8(a)], or up to the boundary, $J_{F,\delta}$, of the Nagaoka F phase.

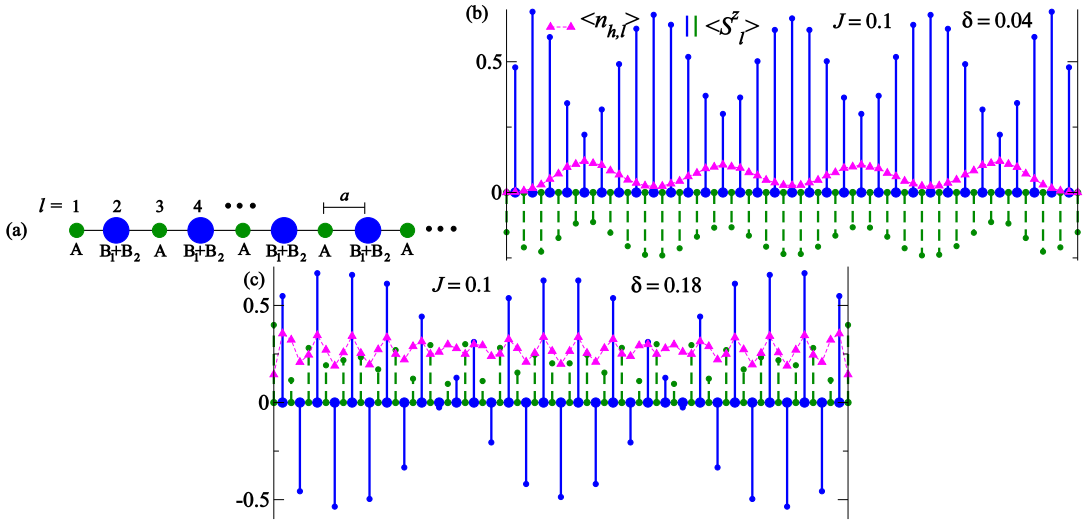

Figura 10 – (a) Effective linear chain (spacing $a \equiv 1$) associated with $N = 3N_c + 1 = 100$ sites for $J = 0.1$ used to illustrate the hole, $\langle\, n_{h,l} \,\rangle$, and spin, $\langle\, S^z_l \,\rangle$, profiles. (b) $\delta = 4/100$ (ferrimagnetic phase) and (c) $\delta = 18/100$ (IC phase). Taken from Ref. (9).

The profiles of the magnetization, $\langle\, S^z_l \,\rangle$, in the spin sector $S^z = S_{GS}$, and of the hole density, $\langle\, n_{h,l} \,\rangle$, were calculated for $J = 0.1$. Thus identifying a modulated itinerant ferrimagnetic phase in the underdoped regime, i.e., for $\delta = 0.04$ the holes distort the ferrimagnetic structure, which displays a modulation with wavelength $\lambda \approx 17$, in antiphase with that exhibited by the hole (charge) density wave, as shown in Fig. 10(b). Note that for $\delta = 0.18$ the magnetization profile displays local maxima in correspondence with those of the hole-density profile, as shown in Fig. 10(c). Therefore, the presence of ferromagnetic Nagaoka spin polarons (due to a hole-density wave with $\lambda \approx 4$) characterizes the IC phase.

In order to better understand the rich variety of doping-induced phases in this system, in Fig. 11 we show the numerical magnetic structure factor:

$$S(q) = \frac{1}{S_L(S_L+1)} \sum_{l,m}^{2N_c+1} e^{iq(l-m)} \langle\, \mathbf{S}_l \cdot \mathbf{S}_m \,\rangle\,, \tag{1.1}$$

where l, m, and $\mathbf{S}$ refer to the lattice representation shown in Fig. 10(a), for $J = 0.3$ and doping ranging from $\delta = 0$ up to $\delta = 0.12$. In a long-range-ordered ferrimagnetic state, sharp maxima at $q = 0$ (ferromagnetism) and $q = \pi$ (antiferromagnetism) were observed in the curve $S(q)$ for $\delta = 0$. By adding only two holes to the undoped state, sharp maxima at $q = 0$ and π are also observed, while at $\delta = 0.04$, these maxima are strongly reduced, thus indicating weak ferrimagnetic order which evolves to the IC phase by increasing hole doping, before phase separation (IC-RVB) at the line $\delta = \delta_{PS,J}$. In the inset of Fig. 11(b) it is shown the departure of the maximum of $S(q)$ from $q = \pi$.

In the next Chapters, we will adopt a functional integral approach to study a doped Hubbard model in the regime of strong correlations on the quasi-one-dimensional

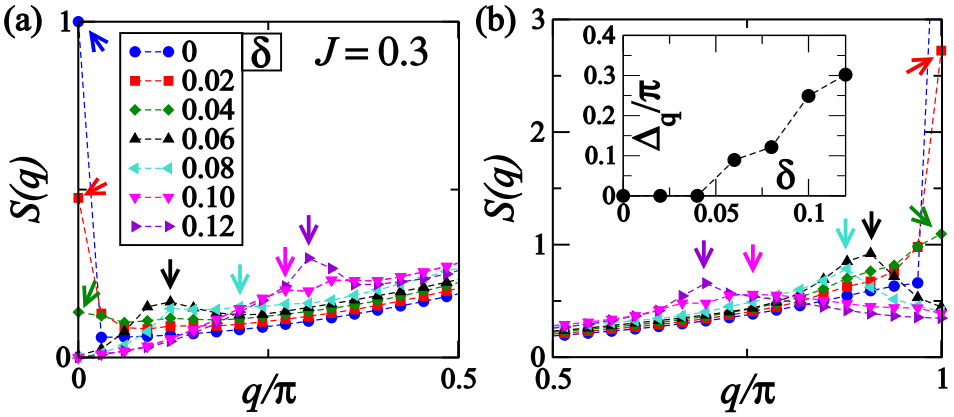

Figura 11 – Chain with $N = 3N_c + 1 = 100$ and $J = 0.3$. (a), (b) Magnetic structure factor $S(q)$ for the indicated values of δ. Inset of panel (b) uses $\Delta_q = q_{\max} - \pi$, where $q_{\max}$ is the value of q at which the local maximum of $S(q)$ near $q = \pi$ is observed. Taken from Ref. (9).

AB_2 lattice. Then, we will present a detailed comparison with the numerical data obtained through DMRG, which is among the most popular numerical methods for one-dimensional quantum systems. Remarkably, this approach well captures the physical picture in the strong correlation regime, both at half filling and in the doped case.

1.5 Outline of Part I of the Thesis

Part I of this Thesis is organized as follows. In Chapter 2, we derive the functional integral representation of the Hubbard Hamiltonian in terms of Grassmann fields (charge degrees of freedom) and spin $SU(2)$ gauge fields (spin degrees of freedom). Further, we diagonalize the Hamiltonian associated with the charge degree of freedom and obtain a perturbative low-energy theory suitable to describe the ferrimagnetic phase at half filling and the phases in the hole-doped regime. In Chapter 3, we show that the resultant Hamiltonian at half filling and large-U, maps onto the spin-1/2 quantum Heisenberg model. In this regime, a perturbative series expansion in powers of $1/S$ of the low-lying excitations of the referred Hamiltonian is presented, which allows us to calculate the GS energy, sublattice magnetizations, and Lieb GS total spin per unit cell in very good agreement with previous estimates. In Chapter 4, we derive the low-energy effective t-J Hamiltonian, which accounts for both charge and spin quantum fluctuations. We also present the evolution of the second-order spin-wave modes, GS energy and total spin per unit cell as a function of the hole doping, thus identifying the occurrence of spatially modulated spin structures, with non-zero and zero GS total spin, and phase separation involving the previous spin structure and RVB states at hole concentration 1/3. Remarkably, these predictions are in very good agreement with the DMRG data reported in Ref. (9), particularly in the regime where the Nagaoka phenomenon is not manifested.

2 FUNCTIONAL INTEGRAL APPROACH TO THE AB_2 HUBBARD MODEL

The goal of this Chapter is to derive a low-energy perturbative functional integral approach to the AB_2 Hubbard model. In Section 2.1, we review the functional integral representation of the Hubbard Hamiltonian in terms of Grassmann fields (charge degrees of freedom) and spin $SU(2)$ gauge fields (spin degrees of freedom). In Section 2.2, we diagonalize the Hamiltonian associated with the charge degree of freedom and obtain a perturbative low-energy theory suitable to describe the ferrimagnetic phase at half filling and the phases in the hole-doped regime.

2.1 Functional integral representation

The Hubbard model is one of the most simple ways to get insight into how the interactions between electrons give rise to insulating, magnetic, and even novel superconducting and superfluid effects in condensed matter physics. Moreover, the Hubbard model is the simplest many-particle model one can write down, which cannot be reduced to a single-particle theory, and with a well-known exact solution (20).

The Hamiltonian of the one-band Hubbard model on chains with AB_2 unit cell topology is given by (12, 13, 15, 16):

$$\mathcal{H} = -\sum_{\langle i\alpha, j\beta\rangle\sigma} \{t_{ij}^{\alpha\beta} \hat{c}_{i\alpha\sigma}^{\dagger} \hat{c}_{j\beta\sigma} + \text{H.c.}\} + U \sum_{i\alpha} \hat{n}_{i\alpha\uparrow} \hat{n}_{i\alpha\downarrow}, \tag{2.1}$$

where $i = 1, \ldots, N_c\,(= N/3)$ is the specific position of the unit cell, N_c (N) is the number of cells (sites), α,$\beta = A, B_1, B_2$ denote the type of site within the unit cell, $\hat{c}_{i\alpha\sigma}^{\dagger}$ ($\hat{c}_{i\alpha\sigma}$) is the creation (annihilation) operator of electrons with spin σ ($=\uparrow, \downarrow$) at site α of cell i, and $\hat{n}_{i\alpha\sigma} = \hat{c}_{i\alpha\sigma}^{\dagger} \hat{c}_{i\alpha\sigma}$ is the occupancy number operator. The first term in Eq. (2.1) describes electron hopping, with energy $t_{ij}^{\alpha\beta} \equiv t$, allowed only between nearest neighbors A-B_1 and A-B_2 linked sites of sublattices A and B (bipartite lattice), and the second one is the on-site Coulombian repulsive interaction $U > 0$, which contributes only in the case of double occupancy of the site $i\alpha$.

At this point, it is instructive to digress on some fundamental aspects of the formalism used in our work (69, 70, 71, 72). With regard to the large-U doped Hubbard chain (69, 70), $U = \infty$ AB_2 Hubbard chain (71) and the Hubbard model on the honeycomb lattice (72), it has been shown that the particle density product in Eq. (2.1) can

be treated through the use of a decomposition procedure, which consist in expressing $\hat{n}_{i\alpha\uparrow}\hat{n}_{i\alpha\downarrow}$ in terms of charge and spin operators:

$$\hat{n}_{i\alpha\uparrow}\hat{n}_{i\alpha\downarrow} = \frac{1}{2}\hat{\rho}_{i\alpha} - 2\left(\hat{\boldsymbol{S}}_{i\alpha}\cdot\boldsymbol{n}_{i\alpha}\right)^2, \tag{2.2}$$

where

$$\hat{\boldsymbol{S}}_{i\alpha} = 1/2\sum_{\sigma\sigma'}\hat{c}^{\dagger}_{i\alpha\sigma'}\boldsymbol{\sigma}_{\sigma'\sigma}\hat{c}_{i\alpha\sigma}, \tag{2.3}$$

and

$$\hat{\rho}_{i\alpha} = \hat{n}_{i\alpha\uparrow} + \hat{n}_{i\alpha\downarrow}, \tag{2.4}$$

are the spin-1/2 and charge-density operators, respectively, $\boldsymbol{\sigma}_{\sigma'\sigma}$ denotes the Pauli matrix elements ($\hbar \equiv 1$), and $\mathbf{n}_{i\alpha}$ is an arbitrary unit vector at site $i\alpha$. Notice that, Eq. (2.2) follows from the identity:

$$\frac{1}{2}\hat{\rho}_{i\alpha} - \hat{n}_{i\alpha\uparrow}\hat{n}_{i\alpha\downarrow} = 2(\hat{S}^{x,y,z}_{i\alpha})^2 = 2(\hat{\mathbf{S}}_{i\alpha}\cdot\mathbf{n}_{i\alpha})^2. \tag{2.5}$$

The convenience of using the decomposition defined in Eq. (2.2) with explicit spin-rotational invariance for the large-U Hubbard model, was discussed at length in Refs. (69, 70, 71, 72).

We start by using the Trotter-Suzuki formula (73, 74), which allows us to write the partition function, $\mathcal{Z} = \mathrm{Tr}\left[\exp(-\beta\mathcal{H})\right]$, at a temperature $k_BT \equiv 1/\beta$, as

$$\mathcal{Z} = \mathrm{Tr}\{\hat{T}\prod_{r=1}^{M}\exp[-\delta\tau\mathcal{H}(\tau_r)]\}, \tag{2.6}$$

where $\hat{T}$ denotes the time-ordering operator, the total imaginary time interval is formally sliced into M discrete intervals of equal size $\delta\tau = \tau_r - \tau_{r-1}$, $r = 1,2,...,M$, with $\tau_0 = 0$, and $\tau_M = \beta = M\delta\tau$, under the limits $M \to \infty$ and $\delta\tau \to 0$. We shall now introduce, between each discrete time interval, an overcomplete basis of fermionic coherent states (73, 74)

$$\int\prod_{i\alpha\sigma}dc^{\dagger}_{i\alpha\sigma}dc_{i\alpha\sigma}\exp(-\sum_{i\alpha\sigma}c^{\dagger}_{i\alpha\sigma}c_{i\alpha\sigma})|\{c_{i\alpha\sigma}\}\rangle\langle\{c_{i\alpha\sigma}\}| = 1, \tag{2.7}$$

where $\{c^{\dagger}_{i\alpha\sigma}, c_{i\alpha\sigma}\}$ denotes a set of Grassmann fields satisfying anti-periodic boundary conditions: $c^{\dagger}_{i\alpha\sigma}(0) = -c^{\dagger}_{i\alpha\sigma}(\beta)$ and $c_{i\alpha\sigma}(0) = -c_{i\alpha\sigma}(\beta)$; while the set of unit vectors defines the vector field $\{\mathbf{n}_{i\alpha}\}$, satisfying periodic ones: $\mathbf{n}_{i\alpha}(0) = \mathbf{n}_{i\alpha}(\beta)$, under a weight functional (see below).

Thereby, following standard procedure (73, 74), the partition function reads:

$$\mathcal{Z} = \int\prod_{i\alpha\sigma}\mathcal{D}c^{\dagger}_{i\alpha\sigma}\mathcal{D}c_{i\alpha\sigma}\prod_{i\alpha}\mathcal{D}^2\mathbf{n}_{i\alpha}W(\{\mathbf{n}_{i\alpha}\})e^{-\int_0^{\beta}\mathcal{L}(\tau)d\tau}, \tag{2.8}$$

where the corresponding measures are defined by

$$\mathcal{D}c^{\dagger}_{i\alpha\sigma}\mathcal{D}c_{i\alpha\sigma} \equiv \lim_{M\to\infty,\delta\tau\to 0}\prod_{r=1}^{M-1}dc^{\dagger}_{i\alpha\sigma}(\tau_r)dc_{i\alpha\sigma}(\tau_r), \tag{2.9}$$

$$\mathcal{D}^2\mathbf{n}_{i\alpha} \equiv \lim_{M\to\infty,\delta\tau\to 0}\prod_{r=1}^{M-1} d^2\mathbf{n}_{i\alpha}(\tau_r), \tag{2.10}$$

the weight functional, $W(\{\mathbf{n}_{i\alpha}\})$, satisfies a normalization condition at each discrete imaginary time τ_r:

$$\int\prod_{i\alpha} d^2\mathbf{n}_{i\alpha} W(\{\mathbf{n}_{i\alpha}(\tau_r)\}) = 1, \tag{2.11}$$

and the Lagrangian density $\mathcal{L}(\tau)$ is written in the form:

$$\mathcal{L}(\tau) = \sum_{i\alpha\sigma} c^{\dagger}_{i\alpha\sigma}\partial_\tau c_{i\alpha\sigma} - \sum_{ij\alpha\beta\sigma}(t^{\alpha\beta}_{ij} c^{\dagger}_{i\alpha\sigma}c_{j\beta\sigma} + \text{H.c.}) + U\sum_{i\alpha}[\frac{\rho_{i\alpha}}{2} - 2(\mathbf{S}_{i\alpha}\cdot\mathbf{n}_{i\alpha})^2]. \tag{2.12}$$

In order to fix $W(\{\mathbf{n}_{i\alpha}\})$ one should notice that, in the electron operator formalism:

$$\hat{\rho}^2_{i\alpha} = \hat{\rho}_{i\alpha} + 2\hat{n}_{i\alpha\uparrow}\hat{n}_{i\alpha\downarrow}. \tag{2.13}$$

To prove the above equation, we use the anticommutation relation, $\hat{c}^{\dagger}_{i\alpha\sigma}\hat{c}_{i\alpha\sigma} = 1 - \hat{c}_{i\alpha\sigma}\hat{c}^{\dagger}_{i\alpha\sigma}$, so that

$$\begin{aligned}\hat{n}^2_{i\alpha\sigma} &= (\hat{c}^{\dagger}_{i\alpha\sigma}\hat{c}_{i\alpha\sigma})^2 = 1 - 2\hat{c}_{i\alpha\sigma}\hat{c}^{\dagger}_{i\alpha\sigma} + \hat{c}_{i\alpha\sigma}\hat{c}^{\dagger}_{i\alpha\sigma}\hat{c}_{i\alpha\sigma}\hat{c}^{\dagger}_{i\alpha\sigma}\\ &= 1 - 2\hat{c}_{i\alpha\sigma}\hat{c}^{\dagger}_{i\alpha\sigma} + \hat{c}_{i\alpha\sigma}(1 - \hat{c}_{i\alpha\sigma}\hat{c}^{\dagger}_{i\alpha\sigma})\hat{c}^{\dagger}_{i\alpha\sigma}\\ &= 1 - \hat{c}_{i\alpha\sigma}\hat{c}^{\dagger}_{i\alpha\sigma} = \hat{c}^{\dagger}_{i\alpha\sigma}\hat{c}_{i\alpha\sigma} = \hat{n}_{i\alpha\sigma},\end{aligned} \tag{2.14}$$

thus, using the Eq. (2.4) is straightforward to find

$$\hat{\rho}^2_{i\alpha} = (\hat{n}_{i\alpha\uparrow} + \hat{n}_{i\alpha\downarrow})^2 = \hat{n}^2_{i\alpha\uparrow} + \hat{n}^2_{i\alpha\downarrow} + 2\hat{n}_{i\alpha\uparrow}\hat{n}_{i\alpha\downarrow} = \hat{\rho}_{i\alpha} + 2\hat{n}_{i\alpha\uparrow}\hat{n}_{i\alpha\downarrow}. \tag{2.15}$$

Therefore, using Eq. (2.2), the following identity holds (69, 70):

$$2(\hat{\mathbf{S}}_{i\alpha}\cdot\mathbf{n}_{i\alpha})^2 = \frac{\hat{\rho}_{i\alpha}(2-\hat{\rho}_{i\alpha})}{2}, \tag{2.16}$$

which means that the square of the spin component operator along the $\mathbf{n}_{i\alpha}$ direction has zero eigenvalues if the site is vacant or doubly occupied, and a nonzero value only for singly occupied sites, i.e., $(\hat{\mathbf{S}}_{i\alpha}\cdot\mathbf{n}_{i\alpha})^2 = 1/4$. Now, taking advantage of our choice of $\mathbf{n}_{i\alpha}$, the local spin-polarization and spin-quantization axes are both chosen along the $\mathbf{n}_{i\alpha}$ direction. Therefore, for singly occupied sites, we find

$$\mathbf{S}_{i\alpha}\cdot\mathbf{n}_{i\alpha} = p_{i\alpha}/2, \tag{2.17}$$

with $p_{i\alpha} = \pm 1$, corresponding to the two possible spin-1/2 states. Further, by incorporating vacancy and double occupancy possibilities, corresponding to the four possible local states of the Hubbard model, one can write (69, 70)

$$p_{i\alpha}\hat{\mathbf{S}}_{i\alpha}\cdot\mathbf{n}_{i\alpha} = \frac{\hat{\rho}_{i\alpha}(2-\hat{\rho}_{i\alpha})}{2}, \tag{2.18}$$

with $p_{i\alpha}^2 = (\pm 1)^2$. We stress that, due to fermion operator properties, the square of Eq. (2.18) reproduces Eq. (2.16), and a comparison between them implies, at arbitrary doping and U value, the formal equivalence between $2(\hat{\mathbf{S}}_{i\alpha} \cdot \mathbf{n}_{i\alpha})^2$ and $p_{i\alpha}(\hat{\mathbf{S}}_{i\alpha} \cdot \mathbf{n}_{i\alpha})$. In this context, we remark that the original Coulomb repulsion term of the Hubbard Hamiltonian in Eq. (2.1) is formally and energetically (eigenvalues) equivalent to both that in Eq. (2.12) or in its linear version through the following replacement: $2(\hat{\mathbf{S}}_{i\alpha} \cdot \mathbf{n}_{i\alpha})^2 \to p_{i\alpha}(\hat{\mathbf{S}}_{i\alpha} \cdot \mathbf{n}_{i\alpha})$. Indeed, using the constraint in Eq. (2.18) we find,

$$U\sum_{i\alpha}[\frac{\rho_{i\alpha}}{2} - p_{i\alpha}(\mathbf{S}_{i\alpha} \cdot \mathbf{n}_{i\alpha})] = U\sum_{i\alpha}[\frac{\rho_{i\alpha}}{2} - \frac{1}{2}\rho_{i\alpha}(2 - \rho_{i\alpha})], \tag{2.19}$$

which is zero for $\rho_{i\alpha} = 0,1$; whereas, as expected, for double occupied sites, $\rho_{i\alpha} = 2$, the local energy is U. Therefore, Eq. (2.18) in its Grassmann version, can be enforced by a proper choice of the normalized weight functional:

$$\begin{aligned} W(\{\mathbf{n}_{i\alpha}\}) &= \lim_{M\to\infty,\delta\tau\to 0}\prod_{r=1}^{M} W(\{\mathbf{n}_{i\alpha}(\tau_r)\}) \\ &= \mathcal{C}\exp\Big\{ -\int_0^\beta d\tau\gamma\sum_{i\alpha}[p_{i\alpha}\mathbf{S}_{i\alpha} \cdot \mathbf{n}_{i\alpha} - \frac{\rho_{i\alpha}}{2}(2 - \rho_{i\alpha})]^2\Big\}, \end{aligned} \tag{2.20}$$

where $\gamma \to \infty$ in the continuum limit ($M \to \infty$, $\delta\tau \to 0$), with delta-function peaks at the four local states of the Hubbard model, and $\mathcal{C}$ is a normalization factor such that Eq. (2.11) holds. In fact, the product of $W(\{\mathbf{n}_{i\alpha}(\tau_r)\})$ in Eq. (2.20) generates a sum in r in the exponential of the suitable chosen Gaussian function, i.e., $W(\{\mathbf{n}_{i\alpha}\})$ is such that in the continuum limit, $M \to \infty$,$\delta\tau \to 0$, Eq. (2.20) obtains with a diverging γ, as pointed out in Ref. (70). In this way, using Eq. (2.20) for the weight functional in Eq. (2.8) for the partition function $\mathcal{Z}$, and integrating over $\{\mathbf{n}_{i\alpha}\}$, the Lagrangian density $\mathcal{L}(\tau)$ in Eq. (2.12) can thus be written in the following linearized form (69):

$$\begin{aligned} \mathcal{L}(\tau) &= \sum_{i\alpha\sigma} c_{i\alpha\sigma}^\dagger \partial_\tau c_{i\alpha\sigma} - \sum_{ij\alpha\beta\sigma}(t_{ij}^{\alpha\beta} c_{i\alpha\sigma}^\dagger c_{j\beta\sigma} + \text{H.c.}) \\ &\quad + U\sum_{i\alpha}[\frac{\rho_{i\alpha}}{2} - p_{i\alpha}(\mathbf{S}_{i\alpha} \cdot \mathbf{n}_{i\alpha})], \end{aligned} \tag{2.21}$$

where the constraint in Eq. (2.18) was explicitly used.

Now, since we are interested in studying the GS properties of the AB_2 Hubbard chains, we choose the staggered factor $p_{i\alpha} = +1\ (-1)$ at sites $\alpha = B_1, B_2\ (A)$, consistent with the long-range ferrimagnetic GS predicted by Lieb's theorem at half filling and for any U value (21, 12, 13), in which case we assume broken rotational symmetry along the z-axis. In this context, by considering the symmetry exhibited by the ferrimagnetic order, let us define the $SU(2)/U(1)$ unitary rotation matrix (75)

$$U_{i\alpha} = \begin{bmatrix} \cos\left(\frac{\theta_{i\alpha}}{2}\right) & -\sin\left(\frac{\theta_{i\alpha}}{2}\right)e^{-i\phi_{i\alpha}} \\ \sin\left(\frac{\theta_{i\alpha}}{2}\right)e^{i\phi_{i\alpha}} & \cos\left(\frac{\theta_{i\alpha}}{2}\right) \end{bmatrix}, \tag{2.22}$$

where $\theta_{i\alpha}$ is the polar angle between the z-axis and the unit local vector $\mathbf{n}_{i\alpha}$ and $\phi_{i\alpha} \in [0,2\pi)$ is an arbitrary azimuth angle due to the $U(1)$ gauge freedom of choice for $U_{i\alpha}$. Moreover, a new set of Grassmann fields, $\{a^{\dagger}_{i\alpha\sigma}, a_{i\alpha\sigma}\}$ can be obtained, according to the transformation:

$$c_{i\alpha\sigma} = \sum_{\sigma'} (U_{i\alpha})_{\sigma\sigma'} a_{i\alpha\sigma'}, \tag{2.23}$$

that locally rotates each unit vector $\mathbf{n}_{i\alpha}$ to the z-direction. On the other hand, if we express the product $\boldsymbol{\sigma} \cdot \mathbf{n}_{i\alpha}$ in matrix form (76):

$$\boldsymbol{\sigma} \cdot \mathbf{n}_{i\alpha} = \begin{bmatrix} \cos(\theta_{i\alpha}) & \sin(\theta_{i\alpha})\, e^{-i\phi_{i\alpha}} \\ \sin(\theta_{i\alpha})\, e^{i\phi_{i\alpha}} & -\cos(\theta_{i\alpha}) \end{bmatrix}, \tag{2.24}$$

we obtain, after using Eq. (2.22),

$$U^{\dagger}_{i\alpha} (\boldsymbol{\sigma} \cdot \mathbf{n}_{i\alpha}) U_{i\alpha} = \sigma^z, \tag{2.25}$$

which explicitly manifest the broken rotational symmetry along the z-axis. In this way, by substituting Eqs. (2.22) and (2.23) into Eq. (2.3), and using the above result, we find

$$\begin{aligned} \mathbf{S}_{i\alpha} \cdot \mathbf{n}_{i\alpha} &= \frac{1}{2} \sum_{\sigma\sigma'} a^{\dagger}_{i\alpha\sigma} [U^{\dagger}_{i\alpha} (\boldsymbol{\sigma} \cdot \mathbf{n}_{i\alpha}) U_{i\alpha}]_{\sigma\sigma'} a_{i\alpha\sigma'} \\ &= \frac{1}{2} \sum_{\sigma\sigma'} a^{\dagger}_{i\alpha\sigma} (\sigma_z)_{\sigma\sigma'} a_{i\alpha\sigma'} \equiv S^z_{i\alpha}; \end{aligned} \tag{2.26}$$

thereby, the constraint in Eq. (2.18) can be written in the form

$$\mathbf{S}_{i\alpha} \cdot \mathbf{n}_{i\alpha} = p_{i\alpha} \frac{\rho_{i\alpha}(2 - \rho_{i\alpha})}{2} = \frac{1}{2} (a^{\dagger}_{i\alpha\uparrow} a_{i\alpha\uparrow} - a^{\dagger}_{i\alpha\downarrow} a_{i\alpha\downarrow}), \tag{2.27}$$

where $p_{i\alpha} = +1\ (-1)$ at sites $\alpha = B_1, B_2\ (A)$. The choice of $p_{i\alpha}$ above implies Lieb's ferrimagnetic ordering with the set $\{\theta_{iA} = \theta_{iB_1} = \theta_{iB_2} = 0\}$, for all i, at half filling. However, in the hole doped regime away from half filling, the $\theta_{i\alpha}$'s can be nonzero (e.g., $\theta_{i\alpha} = \pi$ for a spin flip, leading to a change in the sign of $S^z_{i\alpha}$). Further, $S^z_{i\alpha}$ can be zero either by the presence of holes or doubly occupied sites ($a^{\dagger}_{i\alpha\uparrow} a_{i\alpha\uparrow} = a^{\dagger}_{i\alpha\downarrow} a_{i\alpha\downarrow}$). Lastly, using Eqs. (2.23) and (2.27) into the Lagrangian, Eq. (2.21), we find, after suitable rearrangement of terms,

$$\mathcal{L}(\tau) = \mathcal{L}_0(\tau) + \mathcal{L}_n(\tau), \tag{2.28}$$

where

$$\begin{aligned} \mathcal{L}_0(\tau) = &\sum_{i\alpha\sigma} a^{\dagger}_{i\alpha\sigma} \partial_\tau a_{i\alpha\sigma} - \sum_{i\alpha j\beta\sigma} (t^{\alpha\beta}_{ij} a^{\dagger}_{i\alpha\sigma} a_{j\beta\sigma} + \text{H.c.}) \\ &+ \frac{U}{2} \sum_{i\alpha\sigma} (1 - p_{i\alpha}\sigma) a^{\dagger}_{i\alpha\sigma} a_{i\alpha\sigma}, \end{aligned} \tag{2.29}$$

and

$$\mathcal{L}_n(\tau) = \sum_{i\alpha\sigma\sigma'} a^{\dagger}_{i\alpha\sigma'}(U^{\dagger}_{i\alpha}\partial_\tau U_{i\alpha})_{\sigma'\sigma}a_{i\alpha\sigma} - \sum_{i\alpha j\beta\sigma\sigma'} t^{\alpha\beta}_{ij}[a^{\dagger}_{i\alpha\sigma'}(U^{\dagger}_{i\alpha}U_{j\beta}-1)_{\sigma'\sigma}a_{j\beta\sigma} + \text{H.c.}], \tag{2.30}$$

with the first term in both Eqs. (2.29) and (2.30) being originated from the first term in Eq. (2.21), the second ones come from the hopping term in Eq. (2.21), after a rearrangement of terms, while the last one in Eq. (2.29) (proportional to U) is obtained by using Eq. (2.27) in the last term of Eq. (2.21). It is worth mentioning that only charge degrees of freedom (Grassmann fields) appear in $\mathcal{L}_0(\tau)$, and spin degrees of freedom under the constraint in Eq. (2.27) [$SU(2)$ gauge fields $\{U^{\dagger}_{i\alpha}, U_{i\alpha}\}$, which carry all the information on the vector field $\{\mathbf{n}_{i\alpha}\}$] are now restricted to $\mathcal{L}_n(\tau)$, which includes both spin and charge degrees of freedom.

In the large-U regime, double occupancy is energetically unfavorable and the factor $2-\rho_{i\alpha}$ is no longer needed in Eq. (2.27), i.e., $\mathbf{S}_{i\alpha}\cdot\mathbf{n}_{i\alpha} = p_{i\alpha}\frac{\rho_{i\alpha}}{2}$, with $\rho_{i\alpha}=0$ or 1. In this case, a proper perturbative analysis will allow us to study hole doping effects in Chapter. 4 in a macroscopic fashion, so we define

$$\delta = 1 - \frac{1}{N}\sum_{i\alpha}\langle\rho_{i\alpha}\rangle, \tag{2.31}$$

which measures the thermodynamic average of hole doping away from half filling.

2.2 Charge degrees of freedom and strong-coupling limit

In this Section, we shall first diagonalize the Hamiltonian associated with the Lagrangian $\mathcal{L}_0(\tau)$ through the use of a special symmetry property of the AB_2 chains and a canonical transformation in reciprocal space. Then, by introducing a perturbative expansion in the strong-coupling regime, a low-energy effective Lagrangian for the AB_2 Hubbard chains at half filling and in the doped regime will be obtained.

2.2.1 Charge degrees of freedom

We begin our discussion by considering the Lagrangian $\mathcal{L}_0$ in Eq. (2.29), and its corresponding Hamiltonian $\mathcal{H}_0$, free of the $SU(2)$ gauge fields. By performing the Legendre transformation:

$$\mathcal{H}_0 = -\sum_{i\alpha\sigma}\frac{\partial\mathcal{L}_0}{\partial(\partial_\tau a_{i\alpha\sigma})}\partial_\tau a_{i\alpha\sigma} + \mathcal{L}_0, \tag{2.32}$$

where

$$\frac{\partial\mathcal{L}_0}{\partial(\partial_\tau a_{i\alpha\sigma})} = a^{\dagger}_{i\alpha\sigma}, \tag{2.33}$$

the resulting $\mathcal{H}_0$ is given by

$$\mathcal{H}_0 = -\sum_{\langle i\alpha, j\beta\rangle\sigma} (t_{ij}^{\alpha\beta} a_{i\alpha\sigma}^{\dagger} a_{j\beta\sigma} + \text{H.c.}) + \frac{U}{2}\sum_{i\alpha\sigma}(1 - p_{i\alpha}\sigma) a_{i\alpha\sigma}^{\dagger} a_{i\alpha\sigma}. \tag{2.34}$$

The special AB_2 unit cell topology exhibits a symmetry (14, 17, 31, 71, 9) under the exchange of the labels of the B sites in a given unit cell. Thus, we can construct a new set of Grassmann fields possessing this symmetry, i.e., either symmetric or antisymmetric with respect to the exchange operation $B_1 \leftrightarrow B_2$:

$$\begin{aligned} d_{i\sigma} &= \frac{1}{\sqrt{2}}(a_{iB_1\sigma} + a_{iB_2\sigma}), \\ e_{i\sigma} &= \frac{1}{\sqrt{2}}(a_{iB_1\sigma} - a_{iB_2\sigma}), \\ b_{i\sigma} &= a_{iA\sigma}. \end{aligned} \tag{2.35}$$

Because we are interested in diagonalize Eq. (2.34) in momentum space, it is useful to perform a Fourier transform for the above Grassmann fields as follows

$$\begin{aligned} d_{i\sigma} &= \frac{1}{\sqrt{N_c}}\sum_k e^{ikx_i} d_{k\sigma}, \\ e_{i\sigma} &= \frac{1}{\sqrt{N_c}}\sum_k e^{ikx_i} e_{k\sigma}, \\ b_{i\sigma} &= \frac{1}{\sqrt{N_c}}\sum_k e^{ikx_i} b_{k\sigma}, \end{aligned} \tag{2.36}$$

where $k = 2\pi j(\frac{3}{N})$, with $j = 1,\ldots,N/3$, and $x_i = i$, with $i = 1,\ldots,N/3$ is the position of the i-th unit cell along the x-axis (where the length of the unit cell is set to unity). Then, we can rewrite $\mathcal{H}_0$ as

$$\begin{aligned} \mathcal{H}_0 = &-\sqrt{2}t\sum_{k\sigma}(b_{k\sigma}^{\dagger} d_{k\sigma} + e^{ik} d_{k\sigma}^{\dagger} b_{k\sigma} + \text{H.c.}) \\ &+ \frac{U}{2}\sum_{k\sigma}[(1+\sigma) b_{k\sigma}^{\dagger} b_{k\sigma} + (1-\sigma)(d_{k\sigma}^{\dagger} d_{k\sigma} + e_{k\sigma}^{\dagger} e_{k\sigma})], \end{aligned} \tag{2.37}$$

which is not a diagonal Hamiltonian, even for $U = 0$. As a signature of the quasi-1D structure of the AB_2 chains, we notice that the B_1 and B_2 sites are located at a distance $1/2$ (in the unit of length used) ahead of the A site. Thus, we can make use of this feature to properly introduce a phase factor $e^{\frac{ik}{2}}$ through the following transformation (71):

$$\begin{aligned} A_{k\sigma} &= \frac{1}{\sqrt{2}}(d_{k\sigma} + e^{\frac{ik}{2}} b_{k\sigma}), \\ B_{k\sigma} &= \frac{1}{\sqrt{2}}(d_{k\sigma} - e^{\frac{ik}{2}} b_{k\sigma}), \end{aligned} \tag{2.38}$$

and $\mathcal{H}_0$ in Eq. (2.37) thus becomes

$$\mathcal{H}_0 = \sum_{k\sigma} \varepsilon_k [A^\dagger_{k\sigma} A_{k\sigma} - B^\dagger_{k\sigma} B_{k\sigma}] + \frac{U}{2} \sum_{k\sigma} (1-\sigma) e^\dagger_{k\sigma} e_{k\sigma} + \frac{U}{2} \sum_{k\sigma} [A^\dagger_{k\sigma} A_{k\sigma} + B^\dagger_{k\sigma} B_{k\sigma} - \sigma (A^\dagger_{k\sigma} B_{k\sigma} + B^\dagger_{k\sigma} A_{k\sigma})], \tag{2.39}$$

where

$$\varepsilon_k = -2\sqrt{2} t \cos(k/2). \tag{2.40}$$

We can now exactly diagonalize $\mathcal{H}_0$ through the following Bogoliubov transformation:

$$\begin{aligned} A_{k\sigma} &= u_k \alpha_{k\sigma} - \sigma v_k \beta_{k\sigma}, \\ B_{k\sigma} &= \sigma v_k \alpha_{k\sigma} + u_k \beta_{k\sigma}, \end{aligned} \tag{2.41}$$

with u_k and v_k satisfying the canonical constraint: $(u_k)^2 + (v_k)^2 = 1$, to maintain the anticommutation relations of the Grassmann fields. Due to the ferrimagnetic order of the GS, the above transformation is subject to a 4π periodicity of the functions (fields) $\{u_k, v_k\}$ and $\{\alpha_{k\sigma}, \beta_{k\sigma}\}$. The diagonalized $\mathcal{H}_0$ thus reads:

$$\mathcal{H}_0 = -\sum_{k\sigma} (E_k - \frac{U}{2}) \alpha^\dagger_{k\sigma} \alpha_{k\sigma} + \sum_{k\sigma} (E_k + \frac{U}{2}) \beta^\dagger_{k\sigma} \beta_{k\sigma} + \frac{U}{2} \sum_{k\sigma} (1-\sigma) e^\dagger_{k\sigma} e_{k\sigma}, \tag{2.42}$$

where

$$\begin{aligned} u_k &= \frac{1}{\sqrt{2}} \left(1 + \frac{|\varepsilon_k|}{E_k} \right)^{1/2}, \\ v_k &= \frac{1}{\sqrt{2}} \left(1 - \frac{|\varepsilon_k|}{E_k} \right)^{1/2}, \end{aligned} \tag{2.43}$$

and

$$E_k = \sqrt{\varepsilon_k^2 + U^2/4}. \tag{2.44}$$

As one can see from Eq. (2.42), the non-interacting tight binding ($U = 0$) spectrum of $\mathcal{H}_0$ present three electronic bands: a nondispersive flat band (related to the Grassmann fields $\{e^\dagger_{k\sigma}, e_{k\sigma}\}$, macroscopically degenerate and containing $1/3$ of the energy levels), and two dispersive ones. In AB_2 chains, flat bands are closely associated with ferrimagnetism (unsaturated ferromagnetism) (12, 13, 10) at half filling, in agreement with Lieb's theorem (21, 22), or fully polarized ferromagnetism (24) associated with the flat lowest band. In fact, the mechanism for ferromagnetism works most effectively when this flatband is nearly "saturated" but becomes ineffective when the electron filling factor is too small (12). We also stress that even at this level of approximation and in the weak coupling regime ($U = 2t$), it was shown (12) that hole doping [parametrized by δ defined in Eq. (2.31)] can destroy the ferrimagnetic order and/or induce phase separation in AB_2 chains. As depicted in Fig. 12 (a), the $U = 0$ spin degeneracy of the flat bands is removed by the Coulombian repulsive interaction, in which case a gap

U opens between the $e_{k\sigma}$ modes: $e_{k\uparrow} = 0$, where spins at sites B_1 and B_2 are up, and $e_{k\downarrow} = U$, where these spins are down. On the other hand, the two dispersive bands are spin degenerated, and also display a Hubbard gap U separating the low $(\alpha_{k\sigma})$-energy and high $(\beta_{k\sigma})$-energy modes (71).

2.2.2 Strong-coupling limit

In this subsection, we shall introduce a perturbative expansion in the strong-coupling regime ($U \gg t$) in order to obtain a low-energy effective Lagrangian for the AB_2 Hubbard chain at half filling and in the doped regime. Thereby, we first expand Eq. (2.43) in power of t/U as follows

$$(u_k, v_k) \approx \frac{1}{\sqrt{2}}\left[1 \pm \frac{|\varepsilon_k|}{U} + \mathcal{O}\left(\frac{t^2}{U^2}\right)\right]. \tag{2.45}$$

Next, it will prove useful to define a set of auxiliary spinless Grassmann fields (69, 70, 71) in direct space associated with $d_{i\sigma}$ and $b_{i\sigma}$:

$$\begin{aligned}(\alpha_i, \beta_i) &= \sqrt{\frac{1}{N_c}}\sum_{k,\sigma}\theta(\pm\sigma)e^{ikx_i}(\alpha_{k\sigma}, \beta_{k\sigma}),\\ (\alpha_i^{\frac{1}{2}}, \beta_i^{\frac{1}{2}}) &= \sqrt{\frac{1}{N_c}}\sum_{k,\sigma}\theta(\mp\sigma)e^{ikx_i}e^{-\frac{ik}{2}}(\alpha_{k\sigma}, \beta_{k\sigma}),\end{aligned} \tag{2.46}$$

while for the antisymmetric component, one has

$$e_{i,\sigma} = \sqrt{\frac{1}{N_c}}\sum_{k} e^{ikx_i}e_{k,\sigma},$$

where $\theta(\sigma)$ is the Heaviside function and again, the phase factor $e^{-\frac{ik}{2}}$ signalizes the quasi-1D AB_2 structure. Now, by using the Eqs. (2.36), (2.38) and (2.41), we can write the Grassmann fields $d_{i\sigma}$ and $b_{i\sigma}$ in terms of the Bogoliubov fields $\alpha_{k\sigma}$ and $\beta_{k\sigma}$:

$$d_{i\sigma} = \frac{1}{\sqrt{2N_c}}\sum_{k} e^{ikx_i}[(u_k + \sigma v_k)\alpha_{k\sigma} + (u_k - \sigma v_k)\beta_{k\sigma}], \tag{2.47}$$

$$b_{i\sigma} = \frac{1}{\sqrt{2N_c}}\sum_{k} e^{ik(x_i - \frac{1}{2})}[(u_k - \sigma v_k)\alpha_{k\sigma} - (u_k + \sigma v_k)\beta_{k\sigma}]. \tag{2.48}$$

Lastly, by substituting Eq. (2.45) into the Eqs. (2.47) and (2.48), and using the inverse transformation of (2.46), we can derive a perturbative expansion in powers of t/U for the Grassmann fields $d_{i\sigma}$ and $b_{i\sigma}$ in terms of the spinless Grassmann fields (2.46) up to order (t^2/U^2) as follows:

$$\begin{aligned}d_{i\sigma} = {}& \theta(\sigma)\alpha_i + \theta(-\sigma)\beta_i + \sqrt{2}\frac{t}{U}\theta(-\sigma)(\alpha_i^{\frac{1}{2}} + \alpha_{i+1}^{\frac{1}{2}})\\ &+ \frac{t}{U}\theta(\sigma)[\sqrt{2}(\beta_i^{\frac{1}{2}} + \beta_{i+1}^{\frac{1}{2}}) - \frac{t}{U}(2\alpha_i + \alpha_{i+1} + \alpha_{i-1})]\\ &- \frac{t^2}{U^2}\theta(-\sigma)(2\beta_i + \beta_{i+1} + \beta_{i-1}),\end{aligned} \tag{2.49}$$

$$
\begin{aligned}
b_{i\sigma} = {} & \theta(-\sigma)\alpha_i^{\frac{1}{2}} - \theta(\sigma)\beta_i^{\frac{1}{2}} + \sqrt{2}\frac{t}{U}\theta(\sigma)(\alpha_i + \alpha_{i-1}) \\
& - \frac{t}{U}\theta(-\sigma)[\sqrt{2}(\beta_i + \beta_{i-1}) + \frac{t}{U}(2\alpha_i^{\frac{1}{2}} + \alpha_{i+1}^{\frac{1}{2}} + \alpha_{i-1}^{\frac{1}{2}})] \\
& + \frac{t^2}{U^2}\theta(\sigma)(2\beta_i^{\frac{1}{2}} + \beta_{i+1}^{\frac{1}{2}} + \beta_{i-1}^{\frac{1}{2}}). \qquad (2.50)
\end{aligned}
$$

In the above derivation we have used that $\theta(\sigma)\theta(\sigma') = \theta(\sigma)\delta_{\sigma,\sigma'}$. Notice that, if we let $U \to \infty$ in Eqs. (2.49) and (2.50), a Néel order is found in the half filling regime, where we identify the fields $\alpha_i^{\frac{1}{2}} \approx a_{iA\downarrow}$ and $\alpha_i \approx (a_{iB_1\uparrow} + a_{iB_2\uparrow})/\sqrt{2}$, a result fully consistent with the low-energy spin configuration of the ferrimagnetic state discussed previously. Analogously, for the high-energy bands, the opposite spin configuration is observed, with spin up (down) present at sites A (B_1, B_2).

Introducing Eqs. (2.49) and (2.50) into Eq. (2.34), with the aid of Eq. (2.35), we obtain a perturbative expression for $\mathcal{H}_0$ (low-energy sector) in terms of the spinless Grassmann fields up to order $J = 4t^2/U$:

$$
\begin{aligned}
\mathcal{H}_0 \;=\; & -J\sum_i [\alpha_i^\dagger \alpha_i + \alpha_i^{(\frac{1}{2})\dagger}\alpha_i^{\frac{1}{2}} - \beta_i^\dagger\beta_i - \beta_i^{(\frac{1}{2})\dagger}\beta_i^{\frac{1}{2}}] \\
& -\frac{J}{2}\sum_i [\alpha_i^\dagger \alpha_{i+1} + \alpha_i^{(\frac{1}{2})\dagger}\alpha_{i+1}^{\frac{1}{2}} - \beta_i^\dagger\beta_{i+1} - \beta_i^{(\frac{1}{2})\dagger}\beta_{i+1}^{\frac{1}{2}} + \text{H.c.}] \\
& +U\sum_i [\beta_i^\dagger\beta_i + \beta_i^{(\frac{1}{2})\dagger}\beta_i^{\frac{1}{2}} + e_{i\downarrow}^\dagger e_{i\downarrow}]. \qquad (2.51)
\end{aligned}
$$

By applying Fourier transform to the above expression and rearranging the terms, we obtain

$$
\begin{aligned}
\mathcal{H}_0 \;=\; & -\sum_k 2J\cos^2(k/2)(\alpha_k^\dagger\alpha_k + \alpha_k^{(\frac{1}{2})\dagger}\alpha_k^{\frac{1}{2}}) \\
& +\sum_k [2J\cos^2(k/2) + U](\beta_k^\dagger\beta_k + \beta_k^{(\frac{1}{2})\dagger}\beta_k^{\frac{1}{2}}) \\
& +\frac{U}{2}\sum_{k\sigma}(1-\sigma)e_{k\sigma}^\dagger e_{k\sigma}. \qquad (2.52)
\end{aligned}
$$

In Fig. 12 we plot the electronic spectrum of the Hamiltonian $\mathcal{H}_0$, both in the weak and strong-coupling regime: (a) Eq. (2.42) for $U = 2t$ and (b) Eqs. (2.42) and (2.52) for $U = 12t$ ($J = 4t^2/U = 1/3$), respectively, with $t \equiv 1$. We can notice the presence of the shrinking phenomenon (12) as U increases from $2t$ to $12t$ (strong-coupling regime) and that, for $U = 12t$, Eq. (2.52) is a very good approximation to Eq. (2.42). Noticeably, the $t \ll U$ expansion of the fields allow us to identify $\alpha_k^{\frac{1}{2}} \approx a_{kA\downarrow}$, $\alpha_k \approx (a_{kB_1\uparrow} + a_{kB_2\uparrow})/\sqrt{2}$ (triplet state) and $e_{k\uparrow} \approx (a_{kB_1\uparrow} - a_{kB_2\uparrow})/\sqrt{2}$ (singlet state), as the low-energy spin configuration of the ferrimagnetic state with single occupancy, where spins at sites A (B_1,B_2) are down (up), in agreement with Lieb's theorem (21, 12, 13).

In order to describe the most relevant low-energy processes that take place in this regime, one has to additionally project out the high-energy bands from $\mathcal{H}_0$, that is,

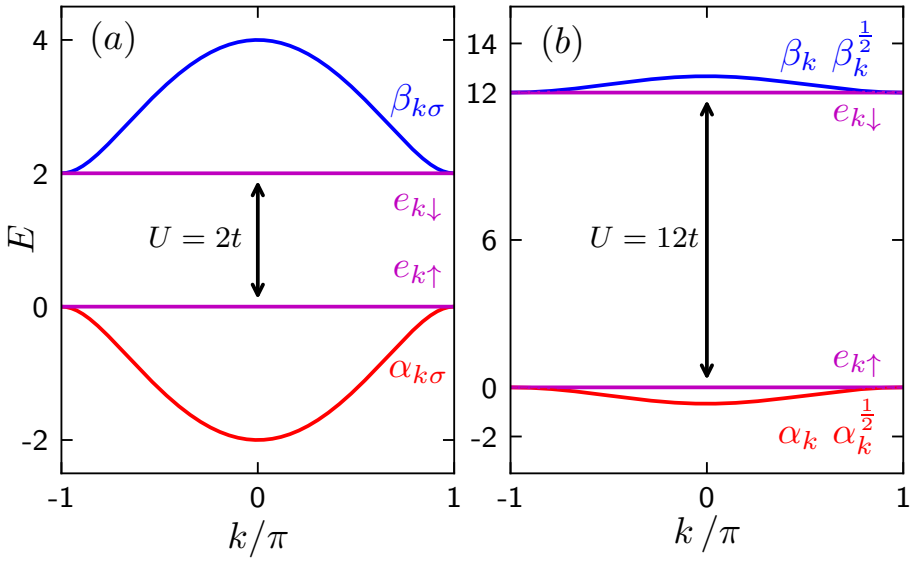

Figura 12 – Electronic spectrum of the Hamiltonian $\mathcal{H}_0$: (a) Eq. (2.42) for $U = 2t$ and (b) Eqs. (2.42) and (2.52) for $U = 12t$ ($J = 4t^2/U = 1/3$), with $t \equiv 1$. Notice the band shrinking phenomenon as U increases from $2t$ to $12t$ (strong-coupling regime). The $t \ll U$ expansion of the fields identifies $\alpha_k^{\frac{1}{2}} \approx a_{kA\downarrow}$, $\alpha_k \approx (a_{kB_1\uparrow} + a_{kB_2\uparrow})/\sqrt{2}$ and $e_{k\uparrow} \approx (a_{kB_1\uparrow} - a_{kB_2\uparrow})/\sqrt{2}$, where spins at sites A (B_1,B_2) are down (up), in agreement with Lieb's theorem.

terms containing only fields related to the high-energy bands: β_i,$\beta_i^{\frac{1}{2}}$,$e_{i\downarrow}^\dagger$, are excluded. Therefore, after the Legendre transformation

$$\mathcal{H}_0 = -\sum_{i,\eta_i} \frac{\partial \mathcal{L}_0}{\partial(\partial_\tau \eta_i)} \partial_\tau \eta_i + \mathcal{L}_0, \tag{2.53}$$

where $\eta_i = \alpha_i$,$\alpha_i^{\frac{1}{2}}$,$e_{i\uparrow}$ (fields related to the low-energy bands), with $\frac{\partial \mathcal{L}_0}{\partial(\partial_\tau \eta_i)} = \eta_i^\dagger$, the Lagrangian associated with $\mathcal{H}_0$ (up to order J) is given by

$$\begin{aligned} \mathcal{L}_0 \;=\; & \sum_i [\alpha_i^\dagger \partial_\tau \alpha_i + \alpha_i^{(\frac{1}{2})\dagger} \partial_\tau \alpha_i^{\frac{1}{2}} + e_{i\uparrow}^\dagger \partial_\tau e_{i\uparrow}] \\ & - J \sum_i [\alpha_i^\dagger \alpha_i + \alpha_i^{(\frac{1}{2})\dagger} \alpha_i^{\frac{1}{2}}] - \frac{J}{2} \sum_i [\alpha_i^\dagger \alpha_{i+1} + \alpha_i^{(\frac{1}{2})\dagger} \alpha_{i+1}^{\frac{1}{2}} + \text{H.c.}]. \end{aligned} \tag{2.54}$$

We shall now focus on the $U \gg t$ perturbative expansion of $\mathcal{L}_n$, Eq. (2.30), which amounts to consider the most significant low-energy processes. For the sake of clarity and completeness, the full derivation of the perturbative expansion of $\mathcal{L}_n$ is given in the Appendix A. Here we restrict ourselves to present the main results. In this view, and after the use of Eqs. (2.49) and (2.50) for $d_{i\sigma}$ and $b_{i\sigma}$ in terms of the spinless Grassmann fields, however, terms allowing interband transitions between low- and high-energy bands still exist in $\mathcal{L}_n$. In consequence, we apply a suitable second-order Rayleigh-Schrödinger perturbation theory (69, 71), consistent with the strong-coupling expansion, so that the modes associated with the high-energy bands are eliminated. Lastly, by

adding $\mathcal{L}_0$ to the perturbative expansion of $\mathcal{L}_n$, which leads to the cancellation of the exchange terms in Eq. (2.54), the effective low-energy Lagrangian density of the AB_2 Hubbard model in the strong-coupling limit (up to order J) reads:

$$\mathcal{L}_{eff}(\tau) = \mathcal{L}^{(I)} + \mathcal{L}^{(II)} + \mathcal{L}^{(III)} + \mathcal{L}^{(IV)}, \tag{2.55}$$

where

$$\mathcal{L}^{(I)} = \sum_i \alpha_i^\dagger \partial_\tau \alpha_i + \sum_i \alpha_i^{(\frac{1}{2})\dagger} \partial_\tau \alpha_i^{(\frac{1}{2})} + \sum_i e_{i\uparrow}^\dagger \partial_\tau e_{i\uparrow}, \tag{2.56a}$$

$$\begin{aligned}\mathcal{L}^{(II)} = \sum_{i\sigma} \Big\{ & \theta(-\sigma)(U_i^{(b)\dagger}\partial_\tau U_i^{(b)})_{\sigma,\sigma}\alpha_i^{(\frac{1}{2})\dagger}\alpha_i^{(\frac{1}{2})} \\ & + \theta(\sigma)\frac{1}{2}[(U_i^{(d)\dagger}\partial_\tau U_i^{(d)})_{\sigma,\sigma} + (U_i^{(e)\dagger}\partial_\tau U_i^{(e)})_{\sigma,\sigma}] \\ & \times (\alpha_i^\dagger \alpha_i + e_{i\uparrow}^\dagger e_{i\uparrow}) + \Big[\theta(\sigma)\frac{1}{2}[(U_i^{(d)\dagger}\partial_\tau U_i^{(e)})_{\sigma,\sigma} \\ & + (U_i^{(e)\dagger}\partial_\tau U_i^{(d)})_{\sigma,\sigma}]\alpha_i^\dagger e_{i\uparrow} + \text{H.c.}\Big]\Big\},\end{aligned} \tag{2.56b}$$

$$\begin{aligned}\mathcal{L}^{(III)} = -t\sum_{i\sigma} \Big\{ & \theta(-\sigma)(U_i^{(b)\dagger}U_i^{(d)})_{\sigma,-\sigma}\alpha_i^{(\frac{1}{2})\dagger}\alpha_i \\ & + \theta(\sigma)(U_i^{(d)\dagger}U_{i+1}^{(b)})_{\sigma,-\sigma}\alpha_i^\dagger\alpha_{i+1}^{(\frac{1}{2})} \\ & + \theta(-\sigma)(U_i^{(b)\dagger}U_i^{(e)})_{\sigma,-\sigma}\alpha_i^{(\frac{1}{2})\dagger}e_{i\uparrow} \\ & + \theta(\sigma)\left(U_i^{(e)\dagger}U_{i+1}^{(b)}\right)_{\sigma,-\sigma} e_{i\uparrow}^\dagger\alpha_{i+1}^{(\frac{1}{2})} + \text{H.c.}\Big\},\end{aligned} \tag{2.56c}$$

$$\begin{aligned}\mathcal{L}^{(IV)} = & -\frac{J}{4}\sum_{i;i'=i,i+1;\sigma}\theta(\sigma)|(U_i^{(d)\dagger}U_{i'}^{(b)})_{\sigma,\sigma}|^2\alpha_i^\dagger\alpha_i \\ & -\frac{J}{4}\sum_{i;i'=i,i+1;\sigma}\theta(\sigma)|(U_i^{(e)\dagger}U_{i'}^{(b)})_{\sigma,\sigma}|^2 e_{i\uparrow}^\dagger e_{i\uparrow} \\ & -\frac{J}{4}\sum_{i;i'=i,i-1;\sigma}\theta(-\sigma)[|(U_i^{(b)\dagger}U_{i'}^{(d)})_{\sigma,\sigma}|^2 \\ & + (U_i^{(b)\dagger}U_{i'}^{(e)})_{\sigma,\sigma}|^2]\alpha_i^{(\frac{1}{2})\dagger}\alpha_i^{(\frac{1}{2})},\end{aligned} \tag{2.56d}$$

where

$$\begin{aligned}U_i^{(b)} &= U_{iA}, \\ U_i^{(d,e)} &= \frac{1}{\sqrt{2}}(U_{iB_1} \pm U_{iB_2}),\end{aligned} \tag{2.57}$$

in which case we took advantage of the symmetry of the AB_2 chain under the exchange operation $B_1 \leftrightarrow B_2$, in correspondence with Eq. (2.35). From the above equations, we see that the kinetic term is represented by $\mathcal{L}^{(I)}$ and is related to the charge degrees of

freedom only, whereas $\mathcal{L}^{(II)}$ describes the dynamics of the spin degrees of freedom coupled to the charge fields. On the other hand, $\mathcal{L}^{(III)}$ exhibit first-neighbor hopping contributions between charge degrees of freedom in the presence of $SU(2)$ gauge fields, while $\mathcal{L}^{(IV)}$ is the spin exchange term in the presence of the charge Grassmann fields.

3 THE AB_2 CHAIN AT HALF FILLING

This Chapter deals with the AB_2 chain at half filling, more specifically, its spin degrees of freedom and the underlying spin quantum fluctuations. In Section 3.1, we show that the resultant Hamiltonian at half filling and large-U maps onto the spin-1/2 quantum Heisenberg model. Then, in Section 3.2 we present a perturbative series expansion in powers of $1/S$ of the spin-wave modes, which allows us to calculate the GS energy, sublattice magnetizations, and Lieb GS total spin per unit cell in very good agreement with previous estimates.

3.1 Half filling regime: Heisenberg model

Let us now discuss some basic aspects of the localized magnetic properties related to the spin degrees of freedom. At half filling, i.e., $\delta = 0$, we have $\langle \alpha_i^\dagger \alpha_i \rangle = 1$, $\langle \alpha_i^{(1/2)\dagger} \alpha_i^{(1/2)} \rangle = 1$, $\langle e_{i\uparrow}^\dagger e_{i\uparrow} \rangle = 1$, and $\langle \alpha_i^\dagger e_{i\uparrow} \rangle = 0$ (no band hybridization) as the electrons tend to fill up the lower-energy bands, whereas the higher-energy ones remain empty. As a consequence, a ferrimagnetic configuration of localized spins emerges, i.e., the charge degrees of freedom are completely frozen, such that $\langle \alpha_i^\dagger \partial_\tau \alpha_i \rangle = \langle \alpha_i^{(1/2)\dagger} \partial_\tau \alpha_i^{(1/2)} \rangle = \langle e_{i\uparrow}^\dagger \partial_\tau e_{i\uparrow} \rangle = 0$, with forbidden hopping. Therefore, only terms from $\mathcal{L}^{II}$ and $\mathcal{L}^{IV}$ in Eqs. (2.56*b*) and (2.56*d*), respectively, give nonzero contributions. Thus, the resulting strong-coupling effective Lagrangian at half filling, as defined in Eq. (2.55), reads:

$$\begin{aligned}\mathcal{L}_{eff}^{J} =& \sum_{i\alpha\sigma} \theta(p_{i\alpha}\sigma)(U_{i\alpha}^\dagger \partial_\tau U_{i\alpha})_{\sigma,\sigma} - \frac{J}{4} \sum_{i;i'=i,i+1;\sigma} \theta(\sigma) |(U_i^{(d)\dagger} U_{i'}^{(b)})_{\sigma,\sigma}|^2 \alpha_i^\dagger \alpha_i \\ & - \frac{J}{4} \sum_{i;i'=i,i-1;\sigma} \theta(-\sigma) [|(U_i^{(b)\dagger} U_{i'}^{(d)})_{\sigma,\sigma}|^2 + (U_i^{(b)\dagger} U_{i'}^{(e)})_{\sigma,\sigma}|^2] \alpha_i^{(\frac{1}{2})\dagger} \alpha_i^{(\frac{1}{2})} \\ & - \frac{J}{4} \sum_{i;i'=i,i+1;\sigma} \theta(\sigma) |(U_i^{(e)\dagger} U_{i'}^{(b)})_{\sigma,\sigma}|^2 e_{i\uparrow}^\dagger e_{i\uparrow}, \end{aligned} \tag{3.1}$$

or in a more compact form:

$$\mathcal{L}_{eff}^{J} = \sum_{i\alpha\sigma} \theta(p_{i\alpha}\sigma)(U_{i\alpha}^\dagger \partial_\tau U_{i\alpha})_{\sigma,\sigma} - \frac{J}{4} \sum_{\langle i\alpha, j\beta \rangle \sigma} \theta(p_{i\alpha}\sigma) \left| (U_{i\alpha}^\dagger U_{j\beta})_{\sigma,\sigma} \right|^2, \tag{3.2}$$

where the staggered factor $p_{i\alpha}$ was defined in Eq. (2.18), and use was made of the matrix transformations defined in Eq. (2.57) in order to sum up the squares of the $SU(2)$ gauge-field products in the exchange contribution from $\mathcal{L}^{IV}$ in Eq. (2.56*d*). Now, using

the following Legendre transform:

$$\mathcal{H}^J_{eff} = -\sum_{i\alpha\sigma} \frac{\partial \mathcal{L}^J_{eff}}{\partial(\partial_\tau U_{i\alpha})_{\sigma,\sigma}} (\partial_\tau U_{i\alpha})_{\sigma,\sigma} + \mathcal{L}^J_{eff}, \tag{3.3}$$

where

$$\frac{\partial \mathcal{L}^J_{eff}}{\partial(\partial_\tau U_{i\alpha})_{\sigma,\sigma}} = \theta(p_{i\alpha}\sigma)(U^\dagger_{i\alpha})_{\sigma,\sigma}, \tag{3.4}$$

we get the respective quantum Heisenberg Hamiltonian written in terms of the $SU(2)$ gauge fields

$$\mathcal{H}^J_{eff} = -\frac{J}{4} \sum_{\langle i\alpha, j\beta\rangle\sigma} \theta(p_{i\alpha}\sigma) \left| (U^\dagger_{i\alpha} U_{j\beta})_{\sigma,\sigma} \right|^2. \tag{3.5}$$

Further, using the definition of the $SU(2)/U(1)$ unitary rotation matrix Eq. (2.22), it is possible to write (69, 70, 71, 72)

$$U_{i\alpha} = \cos(\frac{\theta_{i\alpha}}{2})\mathbb{I} - i\sin(\frac{\theta_{i\alpha}}{2}) \left[\cos(\phi_{i\alpha})\sigma^y - \sin(\phi_{i\alpha})\sigma^x\right], \tag{3.6}$$

and by making use of the properties of the Pauli matrices: $(\sigma^x)_{\sigma,\sigma} = 0$, $(\sigma^y)_{\sigma,\sigma} = 0$ and $(\sigma^z)_{\sigma,\sigma} = \sigma$, the matrix product in Eq. 3.5 can be written as

$$\begin{aligned} \left| (U^\dagger_{i\alpha} U_{j\beta})_{\sigma,\sigma} \right|^2 =& \cos^2(\frac{\theta_{i\alpha}}{2})\cos^2(\frac{\theta_{j\beta}}{2}) + \sin^2(\frac{\theta_{i\alpha}}{2})\sin^2(\frac{\theta_{j\beta}}{2}) \\ &+ 2\cos(\frac{\theta_{i\alpha}}{2})\cos(\frac{\theta_{j\beta}}{2})\sin(\frac{\theta_{i\alpha}}{2})\sin(\frac{\theta_{j\beta}}{2})\cos(\phi_{j\beta} - \phi_{i\alpha}), \end{aligned} \tag{3.7}$$

which implies that

$$\left| (U^\dagger_{i\alpha} U_{j\beta})_{\sigma,\sigma} \right|^2 = \frac{1}{2}(1 + \mathbf{n}_{i\alpha} \cdot \mathbf{n}_{j\beta}), \tag{3.8}$$

where we have used the trigonometric identities $2\sin(\frac{\theta}{2})\cos(\frac{\theta}{2}) = \sin(\theta)$, $\sin^2(\frac{\theta}{2}) = \frac{1}{2}(1 - \cos\theta)$ and $\cos^2(\frac{\theta}{2}) = \frac{1}{2}(1 + \cos\theta)$, while $\mathbf{n}_{i\alpha} = \sin(\theta_{i\alpha})\left[\cos(\phi_{i\alpha})\hat{\mathbf{x}} + \sin(\phi_{i\alpha})\hat{\mathbf{y}}\right] + \cos(\theta_{i\alpha})\hat{\mathbf{z}}$ is the unit vector pointing along the local spin direction. Lastly, by using the constraint as given in Eq. (2.27), we can identify the spin field $\{\mathbf{S}_{i\alpha}\}$ at the single occupied sites:

$$\mathbf{S}_{i\alpha} = \frac{1}{2} p_{i\alpha} \mathbf{n}_{i\alpha}, \tag{3.9}$$

where $p_{i\alpha} = +1\ (-1)$ at sites $\alpha = B_1, B_2\ (A)$, in order to obtain

$$\mathcal{H}^J_{eff} = J \sum_i \left[(\mathbf{S}^{B_1}_i + \mathbf{S}^{B_2}_i) \cdot (\mathbf{S}^A_i + \mathbf{S}^A_{i+1}) \right] - JN_c. \tag{3.10}$$

The above expression is indeed that of the quantum antiferromagnetic Heisenberg spin-1/2 model on the AB_2 chain in zero-field, which takes into account the effects of zero-point quantum spin fluctuations.

3.2 Spin-wave excitations

At half filling ($\delta = 0$) and in the strong-coupling regime $U \gg t$, the itinerant electrons tend to be highly localized, so that the ground state of the AB_2 chain exhibit an unsaturated ferromagnetic or ferrimagnetic long-range order. As mentioned before, the origin of this non-saturation is the presence of a local Néel order inside the unit cell which causes the spins at sites B_1 and B_2 to align in the opposite direction to the spin of the site A. This assertion is rigorously supported by Lieb's theorem(21) and several numerical techniques (12, 10, 9).

In order to take into account the effects of zero-point quantum spin fluctuations, we will analyze the Heisenberg Hamiltonian by means of the spin-wave theory, which has proved very successful in describing the properties of the ground state and low-lying excited states of spin models. Moreover, the predicted results provide a check of the consistency of our approach and will be fully used in our description of the doped regime. In our derivation we will use the Holstein-Primakoff approximation for the operators associated with spin deviations in relation to the Néel configuration.

We first introduce boson creation and annihilation operators via the Holstein-Primakoff (73) transformation:

$$\begin{aligned} S_i^{A,z} &= -S + a_i^\dagger a_i, \\ S_i^{A,+} &= \sqrt{2S} a_i^\dagger \left(1 - \frac{1}{2S} a_i^\dagger a_i\right)^{\frac{1}{2}} = \sqrt{2S} a_i^\dagger f_A(S), \\ S_i^{A,-} &= \sqrt{2S} \left(1 - \frac{1}{2S} a_i^\dagger a_i\right)^{\frac{1}{2}} a_i = \sqrt{2S} f_A(S) a_i, \end{aligned} \tag{3.11}$$

for a down-spin on the A site, and

$$\begin{aligned} S_i^{B_l,z} &= S - b_{li}^\dagger b_{li}, \\ S_i^{B_l,+} &= \sqrt{2S} \left(1 - \frac{1}{2S} b_{li}^\dagger b_{li}\right)^{\frac{1}{2}} b_{li} = \sqrt{2S} f_B(S) b_{li}, \\ S_i^{B_l,-} &= \sqrt{2S} b_{li}^\dagger \left(1 - \frac{1}{2S} b_{li}^\dagger b_{li}\right)^{\frac{1}{2}} = \sqrt{2S} b_{li}^\dagger f_B(S), \end{aligned} \tag{3.12}$$

for an up-spin on the B_l site, with $l = 1,2$, and

$$f_r(S) = \left(1 - \frac{1}{2S} n_r\right)^{1/2} = 1 - \frac{1}{2}\frac{n_r}{2S} + \ldots, \tag{3.13}$$

where S is the spin magnitude, and $n_r = a_i^\dagger a_i$ or $b_{li}^\dagger b_{li}$. The operators $a_i^\dagger$ and a_i (or $b_{li}^\dagger$, b_{li}) satisfy the boson commutation rules $[a_i, a_{i'}^\dagger] = \delta_{ii'}$. Using the known relation between spin operators:

$$\mathbf{S}_i^A \cdot \mathbf{S}_j^B = S_i^{A,z} S_j^{B,z} + \frac{1}{2}(S_i^{A,+} S_j^{B,-} + S_i^{A,-} S_j^{B,+}), \tag{3.14}$$

and after some straightforward but slightly tedious algebra, the spin Hamiltonian, Eq. (3.10), is mapped onto the equivalent boson Hamiltonian:

$$\mathcal{H}^{J}_{eff} = E_0 - JN_c + \mathcal{H}_1 + \mathcal{H}_2 + \mathcal{O}(S^{-1}), \tag{3.15}$$

where

$$E_0 = -4S^2 JN_c, \tag{3.16}$$

is the classical ground state energy, whereas

$$\mathcal{H}_1 = 2JS\sum_i (2a_i^\dagger a_i + \sum_{l=1,2} b_{li}^\dagger b_{li}) + JS\sum_{i,l}\left(a_i^\dagger b_{li}^\dagger + a_i b_{li} + b_{li}^\dagger a_{i+1}^\dagger + b_{li}a_{i+1}\right), \tag{3.17}$$

and

$$\begin{aligned}\mathcal{H}_2 = &- J\sum_{i,l}\left(a_i^\dagger a_i b_{li}^\dagger b_{li} + a_{i+1}^\dagger a_{i+1} b_{li}^\dagger b_{li}\right)\\ &- \frac{J}{4}\sum_{i,l}\left(a_i^\dagger b_{li}^\dagger b_{li}^\dagger b_{li} + a_{i+1}^\dagger b_{li}^\dagger b_{li}^\dagger b_{li} + a_i^\dagger a_i^\dagger a_i b_{li}^\dagger + a_{i+1}^\dagger a_{i+1}^\dagger a_{i+1} b_{li}^\dagger + \text{H.c.}\right).\end{aligned} \tag{3.18}$$

are the quadratic and quartic (interacting) terms of the boson Hamiltonian, suitable to describe the quantum AB_2 Heisenberg model via a perturbative series expansion in powers of $1/S$. Now, we introduce the Bloch-type operator a_k, b_{lk} through the Fourier transformation

$$a_i = \sqrt{\frac{3}{N}}\sum_k e^{ikx_i} a_k, \tag{3.19}$$

$$b_{li} = \sqrt{\frac{3}{N}}\sum_k e^{-ik(x_i+\frac{1}{2})} b_{lk}, \tag{3.20}$$

where k varies over $N/3$ wave vectors in the first Brillouin zone (BZ), and $e^{-\frac{ik}{2}}$ is the phase factor introduced in Eq. (2.38). Thus, the quadratic boson Hamiltonian is then given by

$$\mathcal{H}_1 = 2JS\sum_k (2a_k^\dagger a_k + \sum_l b_{lk}^\dagger b_{lk}) + \sum_{k,l=1,2} 2JS\gamma_k (a_k^\dagger b_{lk}^\dagger + a_k b_{lk}), \tag{3.21}$$

where we have defined the lattice structure factor as

$$\gamma_k = \frac{1}{z}\sum_\rho e^{ik\rho} = \cos(\frac{k}{2}), \tag{3.22}$$

with z denoting the coordination number ($z = 4$ for the AB_2 chain), while $\rho = \pm 1/2$ connects the nearest neighbors A-B_1 and A-B_2 linked sites of sublattices A and B, and

$$\begin{aligned}\mathcal{H}_2 = -\frac{3J}{2N}\sum_{1234,l=1,2}\delta_{12,34}\Big\{&4\gamma_{1-4} a_1^\dagger a_4 b_{l3}^\dagger b_{l2}\\ &+(\gamma_1 a_1^\dagger b_{l4}^\dagger b_{l3}^\dagger b_{l2} + \gamma_{1+2-3} a_1^\dagger a_2^\dagger a_3 b_{l4}^\dagger + \text{H.c.})\Big\},\end{aligned} \tag{3.23}$$

is the quartic boson interacting Hamiltonian in momentum space. For simplicity we use the convention 1 for k_1, 2 for k_2, and so on. Also, the $\delta_{12,34} = \delta(k_1 + k_2 - k_3 - k_4)$ is the Kronecker δ function, and expresses the conservation of momentum to within a reciprocal-lattice vector G.

First, we shall consider $\mathcal{H}_1$, which is the term leading to linear spin-wave theory (LSWT). In fact, $\mathcal{H}_1$ can be diagonalized by the following Bogoliubov transformation:

$$\begin{aligned} a_k &= u_k \beta_k - v_k \alpha_k^\dagger, \\ b_{1,2k} &= \frac{1}{\sqrt{2}}(u_k \alpha_k - v_k \beta_k^\dagger \mp \xi_k), \end{aligned} \tag{3.24}$$

where

$$\begin{aligned} u_k &= \frac{3 + \sqrt{9 - 8\gamma_k^2}}{\sqrt{\left(3 + \sqrt{9 - 8\gamma_k^2}\right)^2 - 8\gamma_k^2}}, \\ v_k &= \frac{2\sqrt{2}\gamma_k}{\sqrt{\left(3 + \sqrt{9 - 8\gamma_k^2}\right)^2 - 8\gamma_k^2}}, \end{aligned} \tag{3.25}$$

satisfy the constraint $u_k^2 - v_k^2 = 1$. Thus,

$$\mathcal{H}_1 = E_1 + \sum_k (\epsilon_k^{0(\alpha)} \alpha_k^\dagger \alpha_k + \epsilon_k^{0(\beta)} \beta_k^\dagger \beta_k + \epsilon_k^{0(\xi)} \xi_k^\dagger \xi_k); \tag{3.26}$$

with

$$E_1 = JS \sum_k (\sqrt{9 - 8\gamma_k^2} - 3), \tag{3.27}$$

and

$$\epsilon_k^{0(\alpha,\beta)} = JS(\sqrt{9 - 8\gamma_k^2} \mp 1), \quad \epsilon_k^{0(\xi)} = 2JS, \tag{3.28}$$

where E_1 is the $\mathcal{O}(S^1)$ quantum correction to the GS energy, and $\epsilon_k^{0(\alpha,\beta)}$, $\epsilon_k^{0(\xi)}$ are the three spin-wave branches provided by LSWT, both in agreement with previous results (77, 26). In fact, it is well known that systems with a ferrimagnetic GS naturally have ferromagnetic and antiferromagnetic spin-wave modes as their elementary magnetic excitations (magnons). For the AB_2 chain, there are three spin-wave branches: an antiferromagnetic mode ($\epsilon_k^{0(\beta)}$) and two ferromagnetic ones ($\epsilon_k^{0(\alpha)}$ and $\epsilon_k^{0(\xi)}$). The mode $\epsilon_k^{0(\alpha)}$ is gapless at $k = 0$, i.e., the Goldstone mode, with a quadratic (ferromagnetic) dispersion relation $\epsilon_k^{0(\alpha)} \sim k^2$. The other two modes are gapped. Notice that the gapped ferromagnetic mode $\epsilon_k^{0(\xi)}$ is flat, and is closely associated with ferrimagnetic properties at half filling (12, 24). Since the dispersive modes preserve the local triplet bond, they are identical to those found in the spin-1/2 - spin-1 chains (78, 79, 80, 81). These chains also exhibit interesting field-induced Luttinger liquid behavior (82).

3.2.1 Quartic interactions

Now, our aim is to obtain the leading corrections to LSWT, i.e., second-order spin-wave theory to the GS energy, sublattice magnetizations and Lieb GS total spin per unit cell. In doing so, we develop a perturbative scheme for the description of this quartic term. First, we decompose the two-body terms by means of the Wick theorem, via normal-ordering protocol for boson operators. Conservation of momentum to within a reciprocal-lattice vector, implies: $k_1 = k+q$, $k_2 = p-q$, $k_3 = k$ and $k_4 = p$. Then, we need to look at the possible pairings of the 4 operators, as for example, in the first term of Eq. (3.23):

$$a^\dagger_{k+q}a_p b^\dagger_{l,k}b_{l,p-q},\ a^\dagger_{k+q}a_p b^\dagger_{l,k}b_{l,p-q},\ a^\dagger_{k+q}a_p b^\dagger_{l,k}b_{l,p-q}.$$

Under this procedure, and by substituting the Bogoliubov transformation, Eqs. (3.24)-(3.25), into Eq. (3.23), we find

$$\mathcal{H}_2 = E_2 + \sum_k (\delta\epsilon_k^{(\alpha)}\alpha_k^\dagger\alpha_k + \delta\epsilon_k^{(\beta)}\beta_k^\dagger\beta_k + \delta\epsilon_k^{(\xi)}\xi_k^\dagger\xi_k), \tag{3.29}$$

where

$$E_2/N_c = -2J(q_1^2 + q_2^2 - \frac{3}{\sqrt{2}}q_1q_2), \tag{3.30}$$

and the corresponding corrections for the spin-wave dispersion relations read:

$$\begin{aligned}\delta\epsilon_k^{(\alpha)} &= J[u_k^2(\sqrt{2}q_2 - 2q_1) + 2v_k^2(\sqrt{2}q_2 - q_1)] \\ &\quad + 4J\gamma_k u_k v_k\left[\frac{3}{2\sqrt{2}}q_1 - q_2\right] + \mathcal{O}(S^{-1}),\end{aligned} \tag{3.31}$$

$$\begin{aligned}\delta\epsilon_k^{(b)} &= J[v_k^2(\sqrt{2}q_2 - 2q_1) + 2u_k^2(\sqrt{2}q_2 - q_1)] \\ &\quad + 4J\gamma_k u_k v_k\left[\frac{3}{2\sqrt{2}}q_1 - q_2\right] + \mathcal{O}(S^{-1}),\end{aligned} \tag{3.32}$$

note that $\delta\epsilon_k^{(\beta)}$ can be obtained from $\delta\epsilon_k^{(\alpha)}$ through the exchange of $u_k \leftrightarrow v_k$, and

$$\delta\epsilon_k^{(\xi)} = J(\sqrt{2}q_2 - 2q_1) + \mathcal{O}(S^{-1}). \tag{3.33}$$

In Eqs. (3.30)-(3.33) above, the quantities q_1 and q_2 are defined by (thermodynamic limit)

$$\begin{aligned}q_1 &= \frac{1}{2\pi}\int_{-\pi}^{\pi} dk(v_k^2), \\ q_2 &= \frac{1}{2\pi}\int_{-\pi}^{\pi} dk(\gamma_k u_k v_k).\end{aligned} \tag{3.34}$$

We remark that in deriving Eqs. (3.30)-(3.33), we have neglected terms containing anomalous products, such as, $\alpha_k^\dagger\beta_k^\dagger$ and vertex corrections.

Lastly, the above results of our perturbative $1/S$ series expansion lead to the effective Hamiltonian:

$$\mathcal{H}^J_{eff} = E^J_{GS} - JN_c + \sum_k (\epsilon^{\alpha}_k \alpha^{\dagger}_k \alpha_k + \epsilon^{(\beta)}_k \beta^{\dagger}_k \beta_k + \epsilon^{(\xi)}_k \xi^{\dagger}_k \xi_k), \tag{3.35}$$

where

$$E^J_{GS} = E_0 + E_1 + E_2, \tag{3.36}$$

which can be read from Eqs. (3.16), (3.27), and (3.30), respectively, is the second-order result up to $\mathcal{O}(1/S)$ for the GS energy, and

$$\epsilon^{(s)}_k = \epsilon^{0(s)}_k + \delta\epsilon^{(s)}_k, \text{ with } s = \alpha, \beta, \xi, \tag{3.37}$$

are the corresponding second-order spin-wave modes, where the linear and the second-order correction terms are given by Eq. (3.28) and Eqs. (3.31)-(3.34), respectively.

3.2.2 Second-order spin-wave analysis

Our perturbative $1/S$ series expansion approach is able to improve the LSWT result for the gap $\Delta = J$ of the antiferromagnetic mode, which should be compared with the second-order result derived from $\epsilon^{(\beta)}_k$, Eqs. (3.28), (3.31) and (3.37), at $k = 0$: $\Delta = (1 + \sqrt{2}q_2)J \simeq 1.676J$, in full agreement with similar spin-wave calculations for AB_2 (26) and spin-1/2-spin-1 (80, 81) chains, and in agreement with numerical estimates using exact diagonalization, $\Delta = 1.759J$, for both AB_2 (10) and spin-1/2-spin-1 (79) chains [see Fig. 13(a) and 13(b)]. On the other hand, the LSWT predicts a gap $\Delta_{flat} = J$ for the flat ferromagnetic mode ($\epsilon^{(\xi)}_k$) in AB_2 chain, whereas our second-order spin-wave theory finds, using Eqs. (3.28), (3.33) and (3.37): $\Delta_{flat} = (1 - 2q_1 + \sqrt{2}q_2)J \simeq 1.066J$, in full agreement with a similar spin-wave procedure (26). Surprisingly, the estimated value from Exact Diagonalization (ED) (10): $\Delta_{flat} = 1.0004J$, lies between these two theoretical values. In fact, analytical approaches are still unable to reproduce the observed level crossing found in numerical calculations (10, 26) for the two ferromagnetic modes [see Fig 13(b)]. This is probably due to the fact that the different symmetries exhibited by the localized excitation (flat mode) and the ferromagnetic dispersive mode are not explicitly manifested in the analytical approaches, so the levels avoid the crossing.

3.2.3 Ground state energy

In the thermodynamic limit, the second-order result for the GS energy of the AB_2 chain per unit cell reads:

$$\frac{E^J_{GS}}{N_c} = -4JS^2 + \frac{JS}{2\pi}\int_{-\pi}^{\pi} dk \left(\sqrt{9 - 8\gamma_k^2} - 3\right) - 2J(q_1^2 + q_2^2 - \frac{3}{\sqrt{2}}q_1 q_2). \tag{3.38}$$

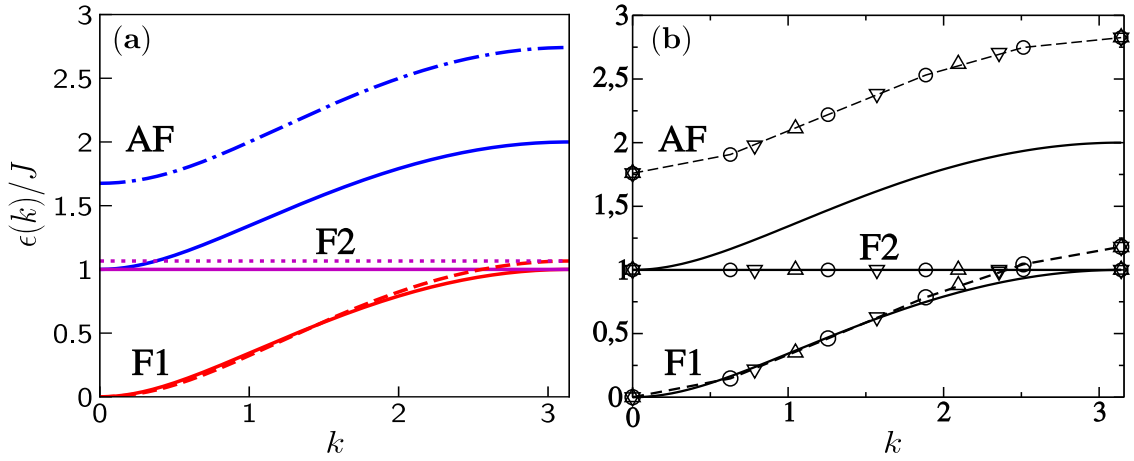

Figura 13 – Ferromagnetic (dispersive F1 and flat F2) and antiferromagnetic (AF) spin-wave modes of the AB_2 chain. (a) Our analytical results, where the solid lines represent the LSWT results from our calculations, whereas the dashed, dotted, and dash-dotted lines are the F1, F2 and AF second-order spin-wave modes, respectively. (b) Numerical results using exact diagonalization techniques, where the dashed lines are guides for the eye. Notice in panel (b) the level crossing found in the numerical calculations for the two ferromagnetic modes. Panel (b), adapted from Ref. (10).

We remark that, at half filling, we shall not consider the constant term $-JN_c$ in Eq. (3.15), with the purpose of comparison with preceding results. Performing the integration over the first BZ and taking $S = 1/2$, we obtain that the GS energy per site at zero-field is given by $-0.4869J$. This result agrees very well with values obtained using exact diagonalization (56) ($-0.485J$) and DMRG (83) ($-0.4847J$) techniques. For the spin-1/2 - spin-1 chain, the value obtained using DMRG (78) is $-0.72704J$. To compare it with our finding, we need to multiply this value by 2/3 (ratio between the number of sites of the two chains), yielding $-0.48469J$.

3.2.4 Sublattice magnetizations and Lieb GS total spin per unit cell

In order to derive results beyond LSWT, we introduce staggered magnetic fields coupled to spins $S_i^{A,z}$ and $S_i^{B_l,z}$, with $l = 1,2$, through the Zeeman terms: $-h_A \sum_i S_i^{A,z}$ and $-h_{B_l} \sum_i S_i^{B_l,z}$, which are added to $\mathcal{H}_{eff}^J$ in Eq. (3.10). Thus, $\langle S^{A,z} \rangle$ and $\langle S^{B_l,z} \rangle$ corresponding to sublattices A and B_l are obtained from

$$\langle S^{A,z} \rangle = -(1/N_c) \sum_{i=1,2} [\partial E_i(h_A)/\partial h_A]|_{h_A=0}, \tag{3.39}$$

and an analogous equation for $\langle S^{B_l,z} \rangle$ using Eqs. (3.27) and (3.30), such that

$$\langle S^{A,z} \rangle = -S + \frac{1}{2\pi} \int_{-\pi}^{\pi} dk v_k^2 - \left(\frac{1}{2S}\right) \frac{q_1}{\pi} \int_{-\pi}^{\pi} dk \frac{\gamma_k^2}{(9 - 8\gamma_k^2)^{3/2}} + \mathcal{O}(\frac{1}{S^2}), \tag{3.40}$$

and

$$\langle S^{B_l,z} \rangle = S - \frac{1}{4\pi}\int_{-\pi}^{\pi} dk v_k^2 + \left(\frac{1}{2S}\right)\frac{q_1}{2\pi}\int_{-\pi}^{\pi} dk \frac{\gamma_k^2}{(9-8\gamma_k^2)^{3/2}} + \mathcal{O}(\frac{1}{S^2}). \tag{3.41}$$

Carrying out the above integration, we obtain $\langle S^{A,z} \rangle = -0.316343$ and $\langle S^{B_l,z} \rangle = 0.408172$. These results are in good agreement with those obtained using DMRG (17) and ED (10) techniques: $\langle S^{A,z} \rangle = -0.2925$ and $\langle S^{B_l,z} \rangle = 0.3962$, respectively, and with values for $\langle S^{A,z} \rangle$ and $2\langle S^{B_l,z} \rangle$ for the spin-1/2 - spin-1 chain (78, 79, 80, 81). Although at zero temperature, the sublattice magnetizations are strongly reduced by quantum fluctuations, as compared with their classical values, the unit cell magnetization remains $S_L \equiv 1/2$, where S_L is the Lieb GS total spin per unit cell, in full agreement with Lieb's theorem (21, 10) for bipartite lattices:

$$S_L = \frac{1}{2}\left\|N_A - N_B\right\|, \tag{3.42}$$

with $N_A(N_B)$ denoting the total number of spins in sublattice $A(B)$ per unit cell. The predicted results provide a check of the consistency of our approach and will be fully used in our description of the doped regime.

4 THE t-J HAMILTONIAN: DOPING-INDUCED PHASES, GROUND STATE ENERGY AND TOTAL SPIN PER UNIT CELL

The goal of this Chapter is to derive, using the previously developed approach, the corresponding *t-J* Hamiltonian suitable to describe the strongly correlated AB_2 Hubbard chain in the doped regime, in which case both charge (Grassmann fields) and spin ($SU(2)$ gauge fields) quantum fluctuations are considered on an equal footing.

4.1 The AB_2 *t-J* Hubbard Hamiltonian

The *t-J* model was derived many years ago by Bulaevskii and coworkers (84) to describe the strong-coupling limit of the single-band Hubbard model. But, only after Anderson's proposal (85) that is was the appropriate model to describe the basic mechanics underlying high-T_c superconductivity in copper oxide compounds (CuO_2), the study of this model became very active. Notice that, although this question remains open, the suggestion has intensified the research of many related fundamental topics, such as: itinerant electron magnetism, Mott metal-insulating transition, and critical quantum phenomena.

Continuing with our approach, the *t-J* Hamiltonian can be derived by means of the following Legendre transformation to Eq. (2.55):

$$\mathcal{H}_{eff}^{t\text{-}J} = -\sum_{i,\mu=b,d,e} \frac{\partial \mathcal{L}_{eff}}{\partial(\partial_\tau U_i^{(\mu)})_{\sigma,\sigma}} (\partial_\tau U_i^{(\mu)})_{\sigma,\sigma} - \sum_{i,\nu_i} \frac{\partial \mathcal{L}_{eff}}{\partial(\partial_\tau \nu_i)} \partial_\tau \nu_i + \mathcal{L}_{eff}, \tag{4.1}$$

where

$$\frac{\partial \mathcal{L}_{eff}}{\partial(\partial_\tau \nu_i)} = \nu_i^\dagger, \text{ with } \nu_i = \alpha_i, \alpha_i^{\frac{1}{2}}, e_{i\uparrow}, \tag{4.2}$$

whereas

$$\frac{\partial \mathcal{L}_{eff}}{\partial(\partial_\tau U_i^{(b)})_{\sigma,\sigma}} = \theta(-\sigma)(U_i^{(b)\dagger})_{\sigma,\sigma} \alpha_i^{(\frac{1}{2})\dagger} \alpha_i^{(\frac{1}{2})}, \tag{4.3}$$

and

$$\frac{\partial \mathcal{L}_{eff}}{\partial(\partial_\tau U_i^{(d,e)})_{\sigma,\sigma}} = \theta(\sigma)\frac{1}{2}[(U_i^{(d,e)\dagger})_{\sigma,\sigma}(\alpha_i^\dagger \alpha_i + e_{i\uparrow}^\dagger e_{i\uparrow}) + (U_i^{(e,d)\dagger})_{\sigma,\sigma}(\alpha_i^\dagger e_{i\uparrow} + e_{i\uparrow}^\dagger \alpha_i)], \tag{4.4}$$

from which we can write the effective *t-J* Hamiltonian as

$$\mathcal{H}^{t\text{-}J}_{eff} = \mathcal{H}^{t} + \mathcal{H}^{J}, \tag{4.5}$$

where

$$\begin{aligned}\mathcal{H}^{t} = &- t\sum_{i\sigma}\{\theta(-\sigma)(U_i^{(b)\dagger}U_i^{(d)})_{\sigma,-\sigma}\alpha_i^{(1/2)\dagger}\alpha_i + \theta(\sigma)(U_i^{(d)\dagger}U_{i+1}^{(b)})_{\sigma,-\sigma}\alpha_i^{\dagger}\alpha_{i+1}^{(1/2)} \\ &+ \theta(-\sigma)(U_i^{(b)\dagger}U_i^{(e)})_{\sigma,-\sigma}\alpha_i^{(1/2)\dagger}e_{i\uparrow} + \theta(\sigma)(U_i^{(e)\dagger}U_{i+1}^{(b)})_{\sigma,-\sigma}e_{i\uparrow}^{\dagger}\alpha_{i+1}^{(1/2)} + \text{H.c.}\},\end{aligned} \tag{4.6}$$

and

$$\begin{aligned}\mathcal{H}^{J} = &- \frac{J}{4}\sum_{i;i'=i,i+1;\sigma}\theta(\sigma)|(U_i^{(d)\dagger}U_{i'}^{(b)})_{\sigma,\sigma}|^2\alpha_i^{\dagger}\alpha_i \\ &- \frac{J}{4}\sum_{i;i'=i,i+1;\sigma}\theta(\sigma)|(U_i^{(e)\dagger}U_{i'}^{(b)})_{\sigma,\sigma}|^2e_{i\uparrow}^{\dagger}e_{i\uparrow} \\ &- \frac{J}{4}\sum_{i;i'=i,i-1;\sigma}\theta(-\sigma)[|(U_i^{(b)\dagger}U_{i'}^{(d)})_{\sigma,\sigma}|^2 \\ &+ |(U_i^{(b)\dagger}U_{i'}^{(e)})_{\sigma,\sigma}|^2]\alpha_i^{(\frac{1}{2})\dagger}\alpha_i^{(\frac{1}{2})}.\end{aligned} \tag{4.7}$$

Notice that Eqs. (4.6) and (4.7) are identical to Eqs. (2.56c) and (2.56d), since Eqs. (2.56a) and (2.56b) were eliminated through the Legendre transformation.

Some digression on $\mathcal{H}^{t\text{-}J}_{eff}$ is in order. One of the key properties of quasi-1D interacting quantum systems is the phenomenon of spin-charge separation, leading to the formation of spin and charge-density waves, which move independently and with different velocities. It has been demonstrated (31) that for $\delta > 2/3$ the low-energy physics of the doped AB_2 Hubbard chain in the $U = \infty$ coupling limit is described in terms of the Luttinger-liquid model, with the spin and charge degrees of freedom decoupled. Most importantly, recently it has been shown that for the AB_2 *t-J* Hubbard chains (9) charge and spin quantum fluctuations are practically decoupled, as suggested by the emergence of charge-density waves in anti-phase with the modulation of the ferrimagnetic order. In this context, one can make use of this feature to formally split each term of the *t-J* Hamiltonian, Eqs. (4.5)-(4.7), into a product of two independent terms acting on different Hilbert spaces, i.e., we can enforce spin-charge separation and calculate the charge and spin correlation functions in a decoupled fashion. In order to further proceed with the calculations, it is important to establish the regime of relevance to our model. We focus on the underdoped regime and values of $J > 0$, where electrons tend to become itinerant. In this regime, the formation of ferromagnetic polarons, a signature of Nagaoka phenomenon, is strongly reduced for not very low values of J (9).

Therefore, from the above discussion, we will consider that the charge correlation functions are well described by an effective spinless tight-binding model (31, 71, 86), since the hole (charge) density waves develop along the x-axis in anti-phase with the

modulation of the ferrimagnetic structure, as numerically observed (9) (see Fig. 10 (b), Chapter. 1). So, using Eqs. (2.46), with $a/2 \to a$ (effective lattice spacing of the linear chain: distance between A and B sites, see Fig. 10 (a) in Chapter. 1, we find

$$\langle\, \alpha_i^{(1/2)\dagger}\alpha_i \,\rangle = \frac{1}{N_c}\sum_{kk'} e^{-ik(x_i-1)}e^{ik'x_i}\,\langle \Psi_0\,|\alpha_k^\dagger\alpha_{k'}|\,\Psi_0\rangle = \frac{1}{\pi}\int_{-k_F(\delta)}^{k_F(\delta)} e^{ik}dk = \frac{2}{\pi}\sin[k_F(\delta)], \quad (4.8)$$

with $|\Psi_0\rangle$ being the hole-doped ferrimagnetic GS, whereas

$$k_F(\delta) = \pi\frac{N_h}{N} \equiv \pi\delta, \quad (4.9)$$

is the Fermi wave vector of the spinless tight-binding holes. In the same fashion:

$$\langle\, \alpha_i^\dagger\alpha_{i+1}^{(1/2)} \,\rangle = \frac{2}{\pi}\sin[k_F(\delta)], \quad (4.10)$$

and $\langle\, \alpha_i^{(1/2)\dagger}e_{i\uparrow} \,\rangle = \langle\, e_{i\uparrow}^\dagger\alpha_{i+1}^{(1/2)} \,\rangle = 0$, while

$$\langle\, \alpha_i^\dagger\alpha_i \,\rangle = \langle\, \alpha_i^{(1/2)\dagger}\alpha_i^{(1/2)} \,\rangle = \langle\, e_{i\uparrow}^\dagger e_{i\uparrow} \,\rangle = (1 - \frac{1}{2\pi}\int_{-k_F(\delta)}^{k_F(\delta)} dk) = (1-\delta). \quad (4.11)$$

Here, we remark that the itinerant holes (away from half filling) are associated with the lower-energy dispersive α_k and $\alpha_k^{(1/2)}$ bands [see Fig. 12 (b)], thus contributing to the kinetic Hamiltonian in Eq. (4.6). On the other hand, the local correlations related to the lower-energy bands α_k, $\alpha_k^{(1/2)}$ and $e_{k\uparrow}$, contribute equally to the exchange Hamiltonian in Eq. (4.7).

Thereby, using the above tight-binding results for the charge correlation functions, $\mathcal{H}_{eff}^{t\text{-}J}$ in Eqs. (4.5)-(4.7) gives rise to the δ-dependent Hamiltonian

$$\mathcal{H}_{eff}^{t\text{-}J}(\delta) = \mathcal{H}_{eff}^{t}(\delta) + \mathcal{H}_{eff}^{J}(\delta), \quad (4.12)$$

which can be written as

$$\begin{aligned}\mathcal{H}_{eff}^{t\text{-}J}(\delta) = &-t\frac{2}{\pi}\sin[k_F(\delta)]\sum_i[(U_i^{(b)\dagger}U_i^{(d)})_{\downarrow\uparrow} + (U_i^{(d)\dagger}U_{i+1}^{(b)})_{\uparrow\downarrow} + \text{H.c.}] \\ &- \frac{J(1-\delta)}{4}\sum_{\langle i\alpha, j\beta\rangle\sigma}\theta(p_{i\alpha}\sigma)|(U_{i\alpha}^\dagger U_{j\beta})_{\sigma,\sigma}|^2, \end{aligned} \quad (4.13)$$

where the sum over σ was evaluated in Eq. (4.6) and the square of the $SU(2)$ gauge-field products in the exchange contribution have been summed up in Eq. (4.7), so that this contribution is just $(1-\delta)$ times $\mathcal{H}_{eff}^{J}$ at half filling, Eq. (3.5), or alternatively, in terms of spin fields, Eq. (3.10), or spin-waves, Eqs. (3.35)-(3.37).

On the other hand, the $SU(2)$ gauge fields matrix elements: $\left(U_i^{(b)\dagger}U_i^{(d)}\right)_{\downarrow\uparrow}$ and $\left(U_i^{(d)\dagger}U_{i+1}^{(b)}\right)_{\uparrow\downarrow}$, that appears in the kinetic contribution to Eq. (4.13), can be written in

terms of the spin fields (71, 72) as

$$(U_i^{(b)\dagger}U_i^{(d)})_{\downarrow\uparrow}+\text{H.c.}=\sum_l\frac{1}{\sqrt{2}}\left(\sqrt{1-2S_i^{B_l,z}+2S_i^{A,z}-4S_i^{A,z}S_i^{B_l,z}}\right.$$
$$\left.+\sqrt{1-2S_i^{A,z}+2S_i^{B_l,z}-4S_i^{A,z}S_i^{B_l,z}}\right), \tag{4.14}$$

and similarly

$$(U_i^{(d)\dagger}U_{i+1}^{(b)})_{\uparrow\downarrow}+\text{H.c.}=\sum_l\frac{1}{\sqrt{2}}\left(\sqrt{1-2S_i^{B_l,z}+2S_{i+1}^{A,z}-4S_{i+1}^{A,z}S_i^{B_l,z}}\right.$$
$$\left.+\sqrt{1-2S_{i+1}^{A,z}+2S_i^{B_l,z}-4S_{i+1}^{A,z}S_i^{B_l,z}}\right). \tag{4.15}$$

Note that, the above term, $\left(U_i^{(d)\dagger}U_{i+1}^{(b)}\right)_{\uparrow\downarrow}$, can be obtained from Eq. (4.14) through the replacement $S_i^{A,z}\to S_{i+1}^{A,z}$. Also notice that these square-root matrix elements depend on z-spin components only.

At this stage, it will prove useful, in the calculation of the GS total spin in the doped regime, to consider $\mathcal{H}_{eff}^{t\text{-}J}(\delta,h)$ which describes the system in the presence of a homogeneous magnetic field $\mathbf{h}=h\hat{\mathbf{z}}=(-h_A+h_{B_1}+h_{B_2})\hat{\mathbf{z}}$, where the staggered fields point along the local corresponding magnetizations in the ferrimagnetic phase have the same magnitude h. The magnetic field couples with the spin fields through the Zeeman term (see Section 3.2.4) and with the charge degrees of freedom through the magnetic orbital coupling in the Landau gauge: $\mathbf{A}=hx\hat{\mathbf{y}}$. Since our aim is to study doping effect on the magnetization, we shall assume vanishingly small magnetic field in the context of linear response theory and perturbative expansion in the strong-coupling regime. Additionally, the magnetic orbital coupling can be considered through the so-called Peierls substitution (32, 87, 88):

$$t\to te^{i\int_{i\alpha}^{j\beta}\mathbf{A}\cdot d\mathbf{l}}, \tag{4.16}$$

where $i\alpha$ and $j\beta$ are first-neighbor sites, and the flux quantum $\phi_0=hc/e\equiv 1$. If one consider that the carrier is at the site iA, we have four hopping possibilities: $iA\to iB_{1,2}$ and $iA\to(i+1)B_{1,2}$, so the total phase ϕ acquired by the carrier in this prescription satisfies Stokes' theorem: $\phi=\oint_{\text{unit cell}}\mathbf{A}\cdot d\mathbf{l}=\iint_S\mathbf{h}\cdot d\mathbf{S}=ha^2$ $(a\equiv 1)$. We also remark that, in order to obtain real values for the zero-field staggered magnetizations, we have considered, for convenience, an imaginary gauge transformation (72, 89): $\mathbf{A}\to i\mathbf{A}$. Therefore, by placing Eq. (4.14) and the similar matrix element into the kinetic term in Eq. (4.13), making the above Peierls substitution, and using the Holstein-Primakoff and Bogoliubov transformations introduced in Eqs. (3.11)-(3.13) and Eqs. (3.24)-(3.25), respectively, up to order $\mathcal{O}(S^{-1})$, we arrive at the following diagonalized kinetic Hamiltonian $\mathcal{H}_{eff}^{t}(\delta,h)$:

$$\mathcal{H}_{eff}^{t}(\delta,h)=\ -\frac{4\sqrt{2}}{\pi}te^{-(-h_A+h_{B_1}+h_{B_2})}\sin[k_F(\delta)]\sum_k[4S-3v_k^2$$
$$-(u_k^2+2v_k^2)\alpha_k^\dagger\alpha_k-(2u_k^2+v_k^2)\beta_k^\dagger\beta_k-\xi_k^\dagger\xi_k], \tag{4.17}$$

where the doping-induced contributions for the spin dispersion relations are evidenced in the last three terms. On the other hand, by adding the Zeeman terms (see Section 3.2.4) to the exchange contribution $\mathcal{H}^{J}_{eff}(\delta)$, given in Eq. (4.13), we obtain $\mathcal{H}^{J}_{eff}(\delta,h)$. Lastly, by combining the kinetic and the exchange contributions, we arrive at the effective *t-J* Hamiltonian in the presence of a magnetic field:

$$\begin{aligned}\mathcal{H}^{t\text{-}J}_{eff}(\delta,h) = &-\frac{4\sqrt{2}}{\pi}te^{-(-h_A+h_{B_1}+h_{B_2})}\sin(\frac{k_F}{2})\sum_k(4S-3v_k^2)+J(1-\delta)(E^J_{GS}-JN_c)\\ &+\sum_k[\epsilon_k^{(\alpha)}(\delta)\alpha_k^\dagger\alpha_k+\epsilon_k^{(\beta)}(\delta)\beta_k^\dagger\beta_k+\epsilon_k^{(\xi)}(\delta)\xi_k^\dagger\xi_k]\\ &-h_A\sum_i S_i^{A,z}-h_{B_1}\sum_i S_i^{B_1,z}-h_{B_2}\sum_i S_i^{B_2,z},\end{aligned} \tag{4.18}$$

where E^J_{GS} is given by Eq. (3.36) and (3.38), and the corresponding spin-wave modes [see Eqs. (4.17), (3.28), (3.31)-(3.34), and (3.37)] of the doped AB_2 *t-J* chain read:

$$\epsilon_k^{(\alpha)}(\delta)=\frac{4\sqrt{2}}{\pi}t\sin(\pi\delta)[u_k^2+2v_k^2]+(1-\delta)(\epsilon_k^{0(\alpha)}+\delta\epsilon_k^{(\alpha)}), \tag{4.19}$$

$$\epsilon_k^{(\beta)}(\delta)=\frac{4\sqrt{2}}{\pi}t\sin(\pi\delta)[v_k^2+2u_k^2]+(1-\delta)(\epsilon_k^{0(\beta)}+\delta\epsilon_k^{(\beta)}), \tag{4.20}$$

note that $\epsilon_k^{(\beta)}(\delta)$ can also be obtained from $\epsilon_k^{(\alpha)}(\delta)$ through the exchange of $u_k \leftrightarrow v_k$ and the replacements: $\alpha \rightarrow \beta$, and

$$\epsilon_k^{(\xi)}(\delta)=\frac{4\sqrt{2}}{\pi}t\sin(\pi\delta)+(1-\delta)(\epsilon_k^{0(\xi)}+\delta\epsilon_k^{(\xi)}). \tag{4.21}$$

We find it instructive to comment on the analytical structure of the above equations. Firstly, we mention the presence of the Bogoliubov parameters [see Eqs. (3.25)] in a symmetric form in the kinetic terms of Eqs. (4.19) and (4.20). Second, although the flat mode is strongly affected by the presence of holes, note that it remains dispersionless. In addition, using Eqs. (4.18) and (3.34), the total GS energy (no spin-wave excitations) per unit cell in the thermodynamic limit is readily obtained:

$$\begin{aligned}E^{t\text{-}J}_{GS}(\delta,h)/N_c = &-\frac{4\sqrt{2}}{\pi}te^{-(-h_A+h_{B_1}+h_{B_2})}\sin(\pi\delta)(4S-3q_1)\\ &+(1-\delta)(E^J_{GS}/N_c-J)-\langle\, S^{A,z}\,\rangle h_A-\sum_{l=1,2}\langle\, S^{B_l,z}\,\rangle h_{B_l},\end{aligned} \tag{4.22}$$

where $\langle\, S^{A,z}\,\rangle$ and $\langle\, S^{B_l,z}\,\rangle$ are the calculated sublattice magnetizations, at half filling and zero-field, given by Eqs. (3.40) and (3.41).

In Sections 4.2, 4.3, and 4.4, we will show that the underlying competing physical mechanisms: the magnetic orbital response and the Zeeman contribution embedded in Eqs. (4.18)-(4.22) will dramatically affect the behavior of the system under hole doping

and, in particular, will lead to spiral IC spin structures, the breakdown of the spiral ferrimagnetic GS at a critical value of the hole doping, a region of phase separation, and RVB states at $\delta \approx 1/3$.

4.2 Doped regime: Spin-wave modes

Before we go one step further to discuss relevant macroscopic quantities, i.e., the GS energy and total spin in the doped regime, we shall first undertake a detailed study, at a microscopic level, of the hole-doping effect on the calculated spin-wave branches given by Eqs. (4.19)-(4.21).

Figure. 14 depicts the second-order spin-wave dispersion relations at $J/t = 0.3$ and for the indicated values of δ. Without loss of generality, we set $t = 1$ in our numerical computations. At half filling, the antiferromagnetic mode $\epsilon_k^{(\beta)}$, together with the two ferromagnetic modes: the dispersive $\epsilon_k^{(\alpha)}$ and the flat one $\epsilon_k^{(\tilde{\xi})}$, are shown in Fig. 14(a), which are defined in Eq. (3.37), and can be plotted using Eqs. (3.28) and (3.31)-(3.34).

As the hole doping increases slightly, the abrupt decrease of the peaks at $k = 0$ and $k = \pi$ of the numerical DRMG structure factor (see Fig. 11), associated with the ferrimagnetic order, manifests itself here through the opening of a gap in the ferromagnetic Goldstone mode $\epsilon_k^{(\alpha)}$, as seen in Fig. 14(b), thus indicating that the system loses its long-range order. Note that the antiferromagnetic mode $\epsilon_k^{(\beta)}$ is also similarly shifted. On the other hand, although the dispersion relation is modified for small values of the wave vector k, the minimum value of $\epsilon_k^{(\alpha)}$ still remains at $k = 0$ up to the onset of the formation of spiral IC spin structures at $\delta_c(\mathrm{IC}) = 0.043$ (a value that should be compared with the numerical DMRG estimate of $\delta \approx 0.055 \pm 0.012$), characterized by the flattening of the dispersive spin-wave branches around zero. Upon further increase of δ, two minima form (around $k = 0$) and move away from each other as one enhances the hole doping. This behavior is the signature of the occurrence of spiral IC spin structures (see Fig. 11).

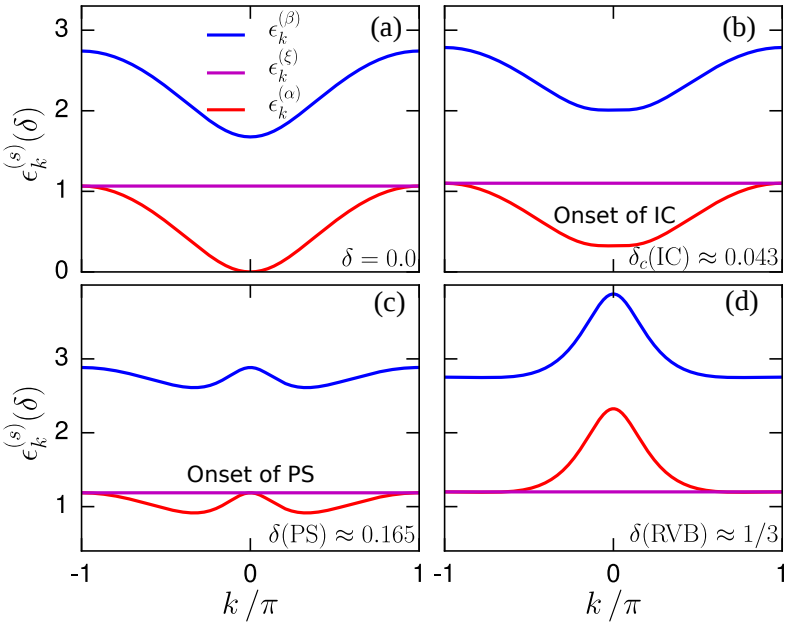

Figura 14 – Evolution of the zero-field second-order spin-wave dispersion relations of the AB_2 t-J chain at $J/t = 0.3$ as a function of hole doping (δ): dispersive ferromagnetic $\epsilon_k^{(\alpha)}$ and antiferromagnetic $\epsilon_k^{(\beta)}$ modes and the flat ferromagnetic one $\epsilon_k^{(\xi)}$, at (a) half filling; (b) the onset of the spiral IC spin structures at $\delta_c(\mathrm{IC}) = 0.043$, in which case the flattening of the gap of $\epsilon_k^{(\alpha)}$ around $k = 0$ is observed; (c) the onset of PS at $\delta(\mathrm{PS}) = 0.165$, characterized by the overlap of the two ferromagnetic modes at $k = 0$ and by the spatial coexistence of two phases: spiral IC spin structures, with modulation fixed at $\delta(\mathrm{PS})$, and RVB states at $\delta \approx 1/3$. (d) At $\delta = 1/3$ the flat mode presents the lowest energy, thus indicating that the short-range RVB state is the stable phase.

Figure. 14(c) shows the onset of phase separation (PS) at $\delta(\mathrm{PS}) = 0.165$, which is characterized by the overlap of the two ferromagnetic modes at $k = 0$. The signature of this regime is the spatial coexistence of two phases: spiral IC spin structures at $\delta(\mathrm{PS}) = 0.165$ and RVB states at $\delta \approx 1/3$, in very good agreement with the numerical estimate of $\delta_{\mathrm{IC-PS}} \approx 0.16$ (9). At $\delta \approx 1/3$, the flat mode has the lowest energy, as illustrated in Fig. 14(d). This behavior indicates that the RVB state is the stable phase at $\delta \approx 1/3$ and $J/t = 0.3$ (9), and also in agreement with the numerical DMRG studies (17, 31) and analytical prediction at $U = \infty$ (71).

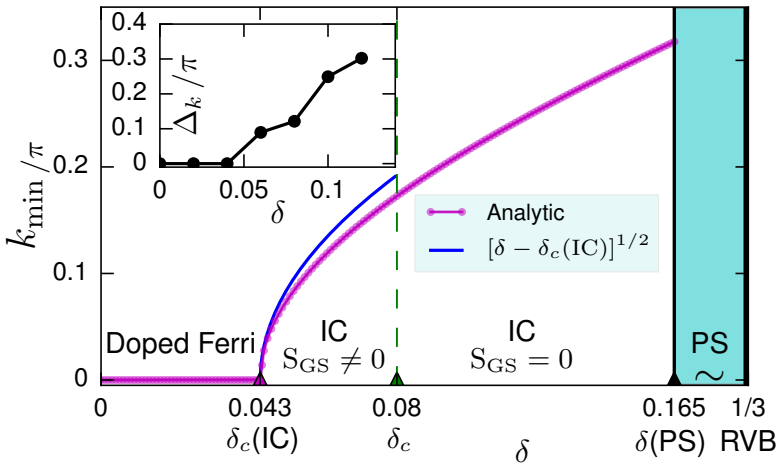

Figura 15 – Evolution of $k_{\min}$ (value of k at the local minimum of $\epsilon_k^{(\alpha)}(\delta)$ near $k=0$) at $J/t=0.3$ as a function of δ: doped ferrimagnetism for $0<\delta<\delta_c(\mathrm{IC})\approx 0.043$; spiral IC spin structures with non-zero (zero) S_{GS} for $\delta_c(\mathrm{IC})<\delta<\delta_c\approx 0.08$ ($\delta_c<\delta<\delta(\mathrm{PS})\approx 0.165$), with a second-order quantum phase transition at $\delta_c(\mathrm{IC})$ characterized by a square-root behavior $[\delta-\delta_c(\mathrm{IC})]^{1/2}$ (blue line), and a first-order transition at $\delta(\mathrm{PS})$ involving the IC spin structure, with modulation fixed at $\delta(\mathrm{PS})$, and short-range RVB states at hole concentration $1/3$. The inset shows DMRG data from Ref. (9) for $\Delta_k\equiv k_{\max}-\pi$ as a function of δ, where $k_{\max}$ is the value of k at the local maximum of the structure factor $S(k)$ near $k=\pi$, in qualitative agreement with the second-order transition at $\delta_c(\mathrm{IC})$.

In order to better understand the rich variety of doping-induced phases in this system at $J/t=0.3$, in Fig. 15 we plot the evolution of the wave vector $k_{\min}$ corresponding to the local minimum of $\epsilon_k^{(\alpha)}(\delta)$, upon increasing the hole doping δ from 0 to $1/3$. The wave vector $k_{\min}$ remains zero until it hits the onset doping value $\delta_c(\mathrm{IC})=0.043$, beyond which a square-root growth behavior takes place (90): $[\delta-\delta_c(\mathrm{IC})]^{1/2}$ (blue line), for δ close to $\delta_c(\mathrm{IC})$. The square-root growth behavior is the signature of the occurrence of a second order quantum phase transition from the doped ferrimagnetic phase to the IC state with a non-zero value of the total GS spin, S_{GS}. This result is supported by the behavior of $\Delta_k\equiv k_{\max}-\pi$ at which the local maximum of the numeric DMRG structure factor $S(k)$ near $k=\pi$ is observed, as shown in the inset of Fig. 15 [taken from the inset of Fig. 11(b)]. For further increase of hole doping our result deviates from the square-root growth behavior and some very interesting features are to be noticed. The value of $\delta_c=0.08$ indicates the breakdown of the total S_{GS} in the IC phase, as will be confirmed by the explicit calculation of S_{GS}, a macroscopic quantity, in Section 4.4. Thus, for $0.08<\delta<0.165$ the system displays an IC phase with zero S_{GS}, in agreement with the DMRG data (see Fig. 1(c) of Ref. (9)). At $\delta(\mathrm{PS})=0.165$ the system exhibits a first-order transition accompanied by the spatially phase separation regime: the IC phase with zero S_{GS} and modulation fixed by $\delta(\mathrm{PS})$ in coexistence with the short-range

RVB states at $\delta \approx 1/3$, also consistent with the DMRG data plotted in Fig. 4 of Ref. (9).

Lastly, we emphasize that, despite the occurrence of several doping-induced phases in the DMRG studies (9): Lieb ferrimagnetism, spiral IC spin structures, RVB states with finite spin gap, phase separation, and Luttinger-liquid behavior, it is surprising and very interesting that the second-order spin-wave modes remain stable up to $\delta \approx 1/3$, with predictions in very good agreement with the DMRG studies (9). In this context, it is worth mentioning the long time studied case of rare earth metals (91, 92), where an external magnetic field can induce non-trivial phase transitions involving spiral spin structures, well described by spin-wave theory. Further, it is worth mentioning that the DMRG results clearly indicate that, for $\delta > 2/3$ (onset at $\delta = 2/3$) the system behaves as a Luttinger liquid (31, 27), which is outside of the scope of the spin-wave approach used in this work. In fact, in this regime the system can be mapped onto an effective linear Hubbard chain and the original approach devised in Ref. (69, 70) using a perturbative scheme based on a soliton representation, including finite hole doping, allows the derivation of results compatible with those of the Bethe ansatz.

4.3 Doped regime: Ground state energy

Performing the integration over the first BZ in Eqs. (3.34) and (3.38) and by setting $S = 1/2$ in Eq. (4.22), we find the AB_2 t-J ground state energy per unit cell as a function of hole doping in zero-field:

$$E_{GS}^{t\text{-}J}(\delta)/JN_c = -1.9543\frac{t}{J}\sin(\pi\delta) - 2.4608(1-\delta). \tag{4.23}$$

We shall now examine the case of small hole doping away from half filling, i.e., with hole concentration ranging from $\delta = 0$ up to $\delta = 0.2$ for two values of J/t: 0.1 and 0.3. In Fig. 16, we show the evolution of the GS energy per unit cell of the AB_2 t-J model as a function of hole doping for both mentioned values of J/t, and the comparison was made with the numerical DMRG data (9). From the two results at $J/t = 0.3$, the only quantitative difference induced by the increase of the hole concentration is a crossing feature around $\delta \approx 0.1$, where our analytical result slightly change its behavior by lowering the energy with respect to the numerical data (9). In fact, because our model assumes a ferrimagnetic state as starting point, this change of behavior suggests that we have entered in a region of strong magnetic instabilities, and possibly indicating a smooth transition to an incommensurate phase with zero GS total spin beyond $\delta \approx 0.1$, as confirmed by the numerical data in Ref. (9) and illustrated in Fig. 15. On the other hand, at $J/t = 0.1$, although our results reproduce the numerical data with acceptable agreement, we observe a discrepancy that increases with δ. The cause of such discrepancy will be discussed in the next section.

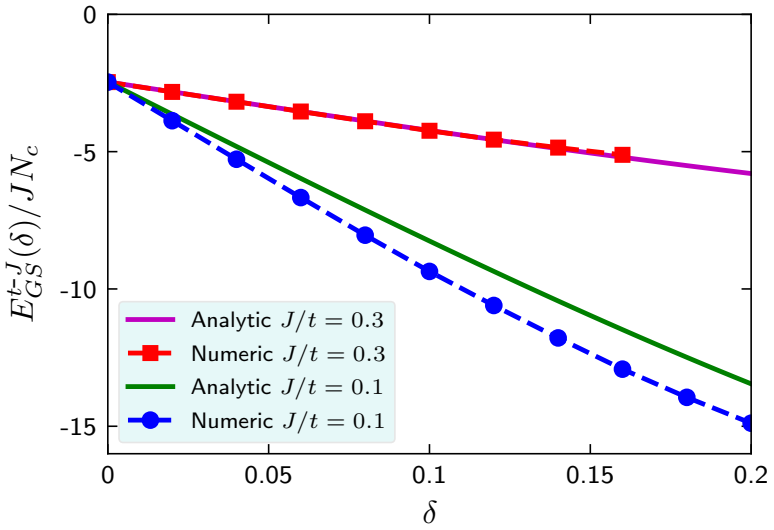

Figura 16 – Analytical prediction for the ground state energy per unit cell of the doped AB_2 t-J chain as a function of doping, and comparison with numerical data from DMRG technique for $J/t = 0.1$ and $J/t = 0.3$ (9). At half filling ($\delta = 0$), both results meet at the expected prediction (9): ≈ -2.4678. Note that we have added the term $-JN_c$ with the intention of comparison with numerical calculation.

Now, with the purpose of determining the interplay between the contribution of magnetic exchange and the itinerant kinetic energy to the zero-field GS energy, Eq. (4.22), we take $J/t = 0.3$ and show its evolution as a function of hole doping in Fig. 17. We can see in the insets, Fig. 17(a) and Fig. 17(b), the competitive behavior of the two energetic contributions, i.e., the contribution of the exchange energy increases linearly with δ, while a practically linear decrease of the hopping term is observed as one enhances the hole doping. This competition indicates that a phase transition to a paramagnetic phase should occur at some critical concentration value.

4.4 Doped regime: Ground state total spin

The existence of a transition from an IC spiral ferrimagnetic phase to an IC paramagnetic one is a most interesting feature observed numerically in doped AB_2 t-J Hubbard chains (9). In order to firmly corroborate the mentioned transition, we have calculated the GS total spin per unit cell as a function of the hole doping concentration,

$$S_{GS}(\delta) = \langle S^{A,z} \rangle(\delta) + \langle S^{B_1,z} \rangle(\delta) + \langle S^{B_2,z} \rangle(\delta), \tag{4.24}$$

by means of the zero-field derivative of Eq. (4.22):

$$\langle S^{\alpha,z} \rangle(\delta) = -(1/N_c)[\partial E_{GS}^{t\text{-}J}(\delta,h)/\partial h_\alpha]|_{h_\alpha=0}, \quad \alpha = A,B_1,B_2. \tag{4.25}$$

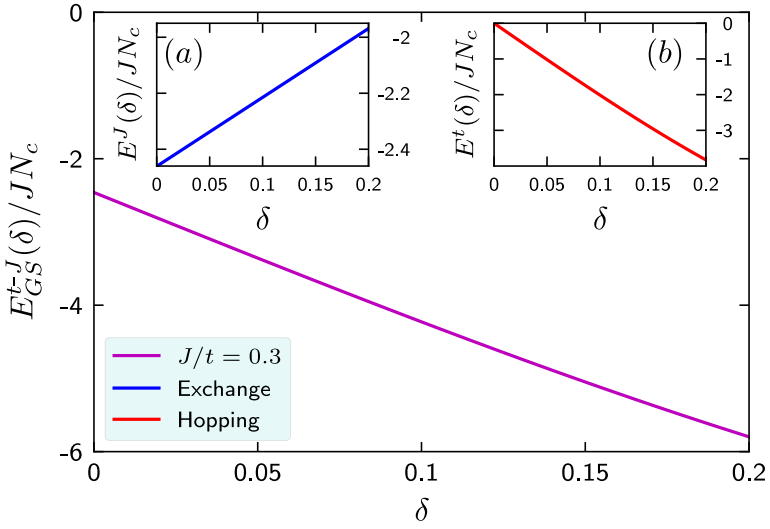

Figura 17 – Ground-state energy per unit cell for the AB_2 t-J chain as a function of δ for $J/t = 0.3$. In the insets, we illustrate the two energetic contribution due to (a) exchange and (b) hopping terms.

Thus, we find

$$\langle S^{A,z} \rangle(\delta) = \langle S^{A,z} \rangle + \frac{4\sqrt{2}}{\pi} t \sin(\pi\delta)(4S - 3q_1), \tag{4.26}$$

and

$$\langle S^{B_l,z} \rangle(\delta) = \langle S^{B_l,z} \rangle - \frac{4\sqrt{2}}{\pi} t \sin(\pi\delta)(4S - 3q_1), \text{ with } l = 1,2, \tag{4.27}$$

where $\langle S^{A,z} \rangle$ and $\langle S^{B_l,z} \rangle$ are given by Eqs. (3.40) and (3.41). Therefore, by performing the integration over the first BZ of the three contributions in Eqs. (4.26) and (4.27), we finally obtain:

$$\frac{S_{GS}(\delta)}{S_L} = 1 - 3.9086 \sin(\pi\delta), \tag{4.28}$$

where

$$S_L = \sum_{\alpha} \langle S^{\alpha,z} \rangle = 1/2, \tag{4.29}$$

is Lieb's reference value for the GS total spin per unit cell at half filling and zero-field (see Section 3.2.4). We stress that, as discussed in Section 3.2.4, Lieb's value $S_L = 1/2$ per unit cell at half filling is fixed regardless of the local quantum fluctuations of the sublattice magnetizations at sites A, B_1, and B_2, which do depend on the Coulomb coupling U, as shown by DMRG calculations in Ref. (10).

In Fig. 18 we plot the evolution of S_{GS}, normalized by S_L, as a function of δ, and compare it with the numerical data from DMRG and Lanczos techniques (9), for $J/t = 0.3$ (red squares) and $J/t = 0.1$ (blue circles). In the latter (former) case, the system undergoes a transition from the modulated itinerant ferrimagnetic phase to an incommensurate phase with zero (nonzero) S_{GS}. Notice that, in both cases, the transition is characterized by a decrease of S_{GS} from S_L to 0 or to a residual value, regardless of the value that S_{GS} takes after the transition. Indeed, at $J/t = 0.1$ and $\delta > 0.1$, the formation

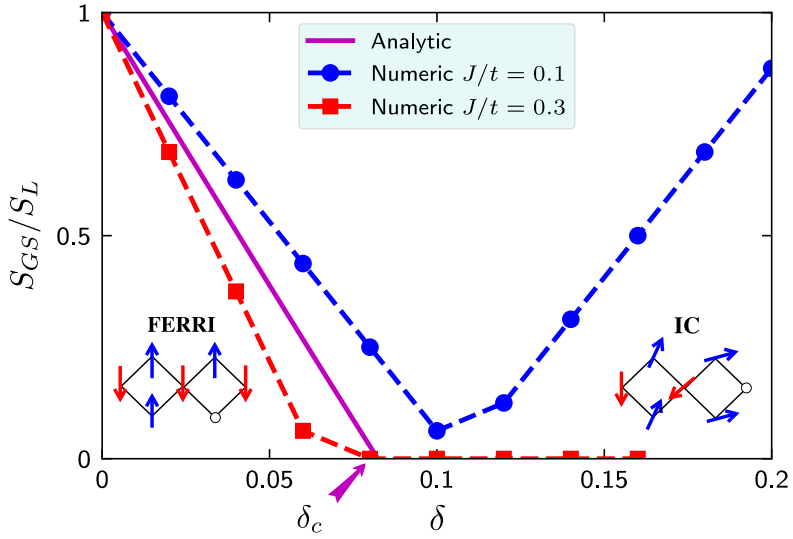

Figura 18 – Numerical (DMRG data) and analytical results of the ground-state total spin S_{GS} per unit cell (solid magenta line), normalized by its value in the undoped regime: $S_L = \frac{1}{2}$, as a function of hole doping δ for the indicated values of J/t. In the figure, $\delta_c \approx 0.08$ indicates the critical value of doping at which the magnetic order is suppressed and a second-order phase transition takes place. DMRG data taken from Ref. (9).

of magnetic polarons (onset of the Nagaoka phenomena that sets in as $U \to \infty$) with charge-density waves *in phase* with the modulation of the ferrimagnetic structure, as indicated by the DMRG data (9), leads to an incommensurate phase with nonzero S_{GS}.

Most importantly, we can observe in Fig. 18 that the value of S_{GS} decreases practically linearly with δ until the magnetic order is completely suppressed at $\delta_c \approx 0.08$. This behavior is supported by numerical results (9), particularly in the regime where the Nagaoka phenomenon is not manifested, that is, at $J/t = 0.3$, as indicated in Fig. 15, in which case charge-density waves are *in antiphase* with the modulation of the ferrimagnetic structure. In this regime, spin and charge quantum fluctuations destabilize the ferrimagnetic structure and triggers a transition to an incommensurate paramagnetic phase at δ_c, with $S_{GS} \sim (\delta - \delta_c) \to 0$.

Lastly, we remark that the main results of Part I form the body of a manuscript submitted for publication in the Journal of Physics: Condensed Matter, entitled *"Lieb and hole-doped ferrimagnetism, spiral, resonating valence-bond states, and phase separation in large-U AB_2 Hubbard chains"* (93).

5 EDGE STATES IN ONE-DIMENSIONAL LATTICES

5.1 Introduction

Among the greatest achievements of modern condensed matter physics is the discovery of graphene and topological insulators. As a result, new families of materials have emerged expanding the field of research in both basic and applied physics, as well as spanning across computational sciences and industry in general. In 2004, K. S. Novoselov and A. K. Geim isolated graphene for the first time, a material composed solely of carbon atoms (94). Shortly after, in 2010, the Nobel Prize in Physics was awarded jointly to K. S. Novoselov and A. K. Geim for groundbreaking experiments regarding the two-dimensional material graphene. One of the most outstanding properties of this material is its thickness of only one atom, which is why it can be considered as a real two-dimensional material (see Fig. 19). Also, due to the strong confinement of the electrons in its interior it shows many interesting properties that can be very useful in technological applications (95, 96).

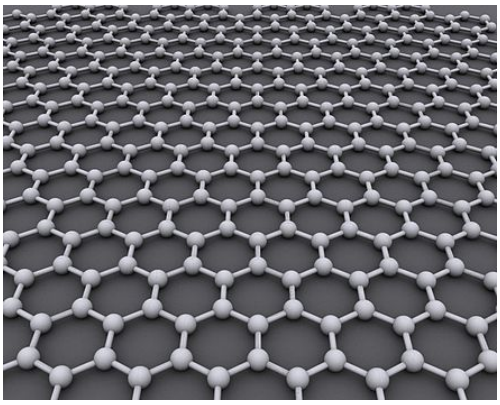

Figura 19 – A partial view of graphene, which is an allotrope (form) of carbon consisting of a single layer of carbon atoms arranged in a hexagonal lattice. Taken from Wikipedia.

On the other hand, in 2005 the quantum spin Hall insulator was theorized to exist in graphene by C. L. Kane and E. J. Mele (97). Remarkably, only two years later it was experimentally observed, in the group led by Shou-Cheng Zhang, the existence of topological states in HgCdTe quantum well structures (98) (see Fig. 20). This was the first determination of an intrinsic topological insulator. Here the definition of intrinsic is by reference to intrinsic semiconductors: its Fermi level lies in between the bulk conduction band minimum and the bulk valence band maximum and only intersects the metallic surface state. A couple of decades earlier, Klaus von Klitzing had discovered

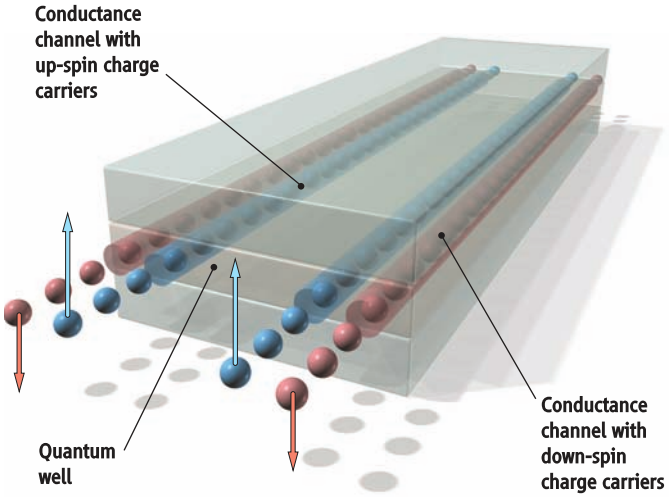

Figura 20 – Schematic view of the spin-polarized edge channels in a quantum spin Hall insulator. Taken from Ref. (98).

the quantum Hall effect in a two-dimensional electron gas, in the presence of a strong magnetic field (99). Both cases aroused great interest in the scientific community due to the potential applications that can provide the robustness and directionality of electron and spin transport in topological insulators.

Indeed, these discoveries generated great advances in various fields of physics. One of them is condensed matter that focuses on the discovery and classification of the different phases of matter, as well as explain the novel behaviors that emerge when many degrees of freedom interact. Furthermore, this sequence of breakthroughs allowed the connection between two scientific areas so far independent: topology (branch of mathematics) and condensed matter (branch of physics). So, in little more than 10 years, a new field of research was developed whose objective is the theoretical and experimental study of materials that behave as topological insulators.

Lastly, it is important to mention that, in 1982, D. Thouless and collaborators explained the very precise quantization of the Hall conductance in two-dimensional electron gases using topological concepts (100). Soon after, in 1983 Duncan Haldane derived a theory for spin chains that incorporated effects of topology in a crucial way (101, 102). He predicted, based on this, that chains with integer and half-integer spins should be qualitatively different, and this totally unexpected effect was later confirmed by experiments. As a result, in 2016 the Nobel Prize in Physics was awarded with one half to David J. Thouless, and the other half to F. Duncan M. Haldane and J. Michael Kosterlitz, for their theoretical discoveries of topological phase transitions and topological phases of matter.

5.2 Topological insulators

In recent years, physics and mathematics have found a new connection point in the area of topological insulators (103). Until 1980, the electrical properties of matter were described using the successfully band theory of solids, widely used in solid-state physics. In this way, the systems were classified into common insulators (trivial), semiconductors and metals, according to whether or not they present a gap in the electronic structure. However, in 1980 Klaus von Klitzing discovered, a novel material with unexplained and fascinating properties (99), which is now known as a topological insulator.

Roughly speaking, topology is a concept of classifying objects by their global properties (104). Two objects belong to the same topological class if and only if they can be continuously transformed into each other without violating certain sets of rules. In other words, topology describes the properties that remain intact when an object is stretched, twisted or deformed, but not if it is torn apart. In this view, topological insulators arise as a new phase of matter.

A topological insulator is characterized by the absence of electrical conduction in the bulk (hence its name of insulator) and by the presence of metallic states that carry current at the edges or faces, i.e., the surfaces are metallic because of its topological surface states. Metallic states are protected by system-specific symmetries such as inversion, time-reversal or chiral symmetry, among others (103, 105, 106). This protection makes the electrical conduction extremely robust against disorder or sample imperfections, a feature that is of great interest for possible applications in the industry in general. The electrical properties and robustness of these materials can be explained from their topological character, which is determined by calculating a mathematical invariant (100, 104). As a result, topological order is now considered a main ingredient of modern band theory.

The starting point in the development of this new branch of physics was mainly experimental, through the measurement of the integer quantum Hall effect (see Fig. 21) in two-dimensional electron gases (99). The theoretical connection with topology is, in fact, more recent in time. However, only through this connection were many of the previously obtained experimental results justified, in addition to allowing to make new predictions that expanded the field of study, the interest and the application of topological insulators.

5.3 Topological invariants

The first theoretical explanation of the integer quantum Hall effect was formulated in 1982 by David J. Thouless (100), a couple of years after its experimental discovery, based on a previous argument by Robert B. Laughlin (107). Specifically, it states that the

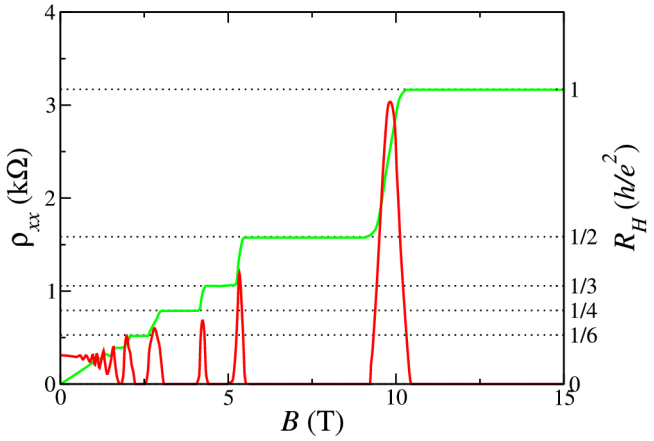

Figura 21 – Resistivities of the integer quantum Hall system, as functions of the magnetic field. The red line shows the longitudinal resistivity ρ_{xx}, it is zero as long as ρ_{xy} sits on a plateau level and spikes whenever ρ_{xx} changes from one plateau to the next. The green line denotes the Hall resistivity ρ_{xy}, it takes on a plateau form, i.e. it is constant over a range of magnetic fields. Image adapted from Ref. (99).

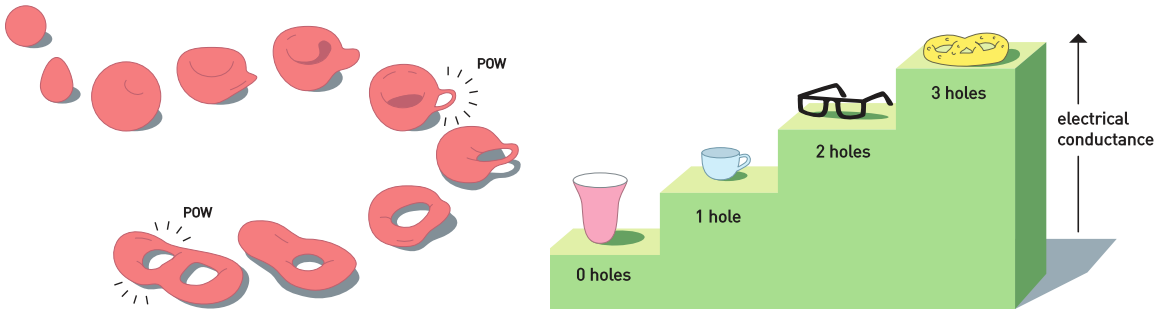

Figura 22 – Topology is interested in properties that change step-wise, like the number of holes in the above objects (left panel). Moreover, topology explains why electrical conductivity inside thin layers changes in integer steps (right panel). Taken from Ref. (108).

Hall conductance in a two-dimensional band insulator can be expressed in terms of the Berry curvature:

$$\sigma_{xy} = \frac{e^2}{\hbar}\int_{BZ}\frac{d\mathbf{k}}{(2\pi)^2}\Omega_{k_x,k_y} = n\frac{e^2}{h}, \tag{5.1}$$

with the Berry curvature defined as $\Omega^n(\mathbf{k}) = i\nabla_{\mathbf{k}}\langle\psi_n(\mathbf{k})|\nabla_{\mathbf{k}}|\psi_n(\mathbf{k})\rangle$, where $\psi_n(\mathbf{k})$ are the Bloch wave functions. The final result is consistent with what is observed experimentally: the conductance is quantized in integer units of e^2/h and is proportional to the number of edge states (see Fig. 21).

In topology it is possible to classify objects according to an invariant, that is, a property that does not change in the face of smooth deformations (104). A typical example of invariant is the number of holes in a material: it is possible to smoothly deform a sphere until it becomes a glass (0 holes), but to obtain a mug it is necessary to create a hole (the one in the handle), so the sphere and the mug belong to two

different topological groups (see Fig. 22). Similarly, the mug can be deformed to obtain a doughnut but not a pair of glasses (it has two holes). This whole idea can be extended to physics. Then, it is possible to use the notions of topology to distinguish trivial insulators from topological insulators.

On the other hand, topological invariants commonly used in physics count, instead of the number of holes in an object, the number of poles in the wave function of the material under study (100). For instance, the relevant invariant in two dimensions is the Berry phase, which is essentially the geometric phase acquired after an adiabatic loop in the Brillouin zone. The topological invariants are then a non-local measure (involving the wave function) that characterizes the bulk of the material.

5.4 Bulk-boundary correspondence

The bulk-boundary correspondence in Hermitian systems establishes a relation between a bulk property of a (translational-invariant) lattice, encoded in a topological invariant (obtained from the Bloch-type eigenstates), and what happens at its boundary (surface, edge, end). Let's consider a piece of (nontrivial) topological insulator. Outside the material we have vacuum. The vacuum is classified as a trivial insulator (109). In this way, if we go from inside the sample to outside, we need to change the topology. In other words, the topological invariant needs to change its value from nonzero to zero. However, from the previous definition of topology, we know that the topology cannot change if we deform our system in any continuous way. For instance, one cannot deform a sphere into a torus (or vice versa) without destroy the surface (see Fig. 22). The same applies to insulators, as one cannot deform a topological insulator into a trivial insulator without destroy the insulator. Hence, what we need is to change the topology when we cross the interface between our sample and the outside. To achieve this change of topology it is necessary to assume that our insulating state is destroyed when we traverse the interface, and this implies that the interface is a metal. In physical terms, this means that, at the interface between both insulators, the material behaves as a metal (a system without a gap in the band structure, where the invariant is not well defined). The conducting states that arise at the interface are called topological edge states.

The main difference between an edge state due to electrons located at the boundaries of the sample and the topological ones is in the robustness against defects and disorder in the system. As a property of the bulk, topological edge states are originated by the difference in topological orders of the contiguous or adjacent materials. This is why they do not depend on the atomic details of the interface and can not be destroyed by local edge perturbations (such as imperfections) (103). On the contrary, states that are formed by the existence of a boundary and independently of the topological order of the material, can be easily modified, destroyed or eliminated. This characteristic of

topological insulators is important among other reasons because, to define one phase of matter as different from another, the properties should not be easily destroyed by small perturbations.

The existence of topological edge states in a material is clearly reflected in the Hall conductivity. The Hall conductivity is determined by the topology of the quantum wave function and the topology is not affected by impurities. Also, it is directly related to the number of these edge states through the topological invariant, and thus inherits the robustness against perturbations such as disorder or interactions between particles. In fact, it is known that topological edge states are the responsible for the quantization of the conductivity in the integer quantum Hall effect of the two-dimensional electron gas under the action of an external magnetic field (topological insulator in contact with the vacuum, which is a trivial insulator) (103, 109). This is a very special quantum state of matter where interactions and impurities play no role. Therefore, the atomistic details of a sample are irrelevant when it comes to states stemming from the interaction between two materials of different topological order. The bulk determines what happens at the boundaries, i.e., the appearance of edge states and how many of them are. This result is what is known as bulk-edge correspondence (106).

6 EDGE STATES IN TRIMER LATTICES

The search for novel topological states of matter (100, 102, 110, 111) has rapidly expanded over the last decades since the discovery of topological insulators (97, 112, 98, 103, 105). Examples range from topological states in driven quantum systems (113, 114, 115) to artificial systems including ultracold matter (116, 117) and photonic waveguides (118, 119, 120). Although originally most of the studies focused on two-dimensional (2D) systems (121, 97), later on they evolved to three (122) and one dimensions (123, 124).

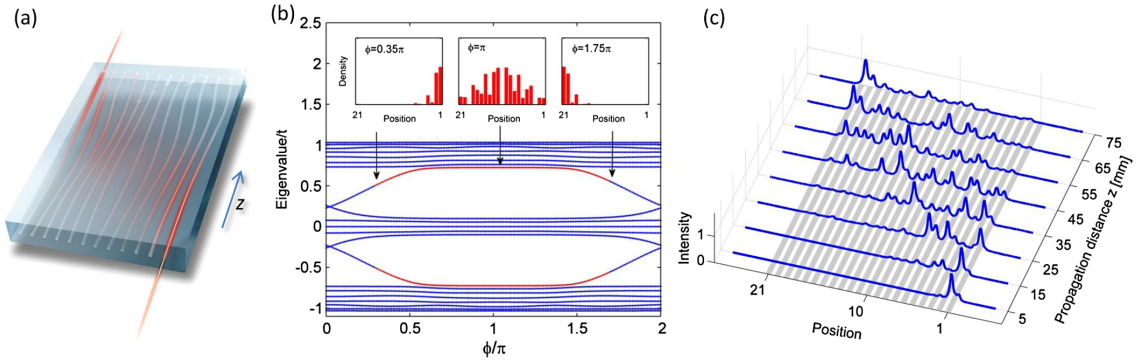

Figura 23 – Experimental observation of adiabatic pumping via topologically protected boundary states in a photonic quasicrystal. (a) An illustration of the adiabatically modulated photonic quasicrystal, constructed by slowly varying the spacing between the waveguides along the propagation axis z. The injected light experiences an adiabatically modulated Hamiltonian and is pumped across the sample. (b) The spectrum of the model as a function of the phase ϕ. The insets depict the spatial density of a boundary eigenstate as a function of the position at three different stages of the evolution. (c) Experimental results: Light was injected into the rightmost waveguide (site 1) at $z = 0$. The measured intensity distributions as a function of the position are presented at different stages of the adiabatic evolution. Taken from Ref. (125).

Quasicrystals (127), materials characterized by long-range orientational order but without the periodicity of crystals (see Fig. 23), appeared to be out of the topological chart until the work of Kraus and coworkers (125). They showed that lower dimensional quasiperiodic systems can feel the effect of a higher-dimensional "ancestor" crystal, through additional degrees of freedom ϕ that appear as remnants of the higher dimensionality (see Figs. 23 and 24). Shortly after, it was shown that crystal and quasicrystal band insulators are topologically equivalent (128). Because of these connections, together with the reduced complexity of low-dimensional lattices and also thanks to the advance in experimental techniques, research on topological states in 1D systems has been

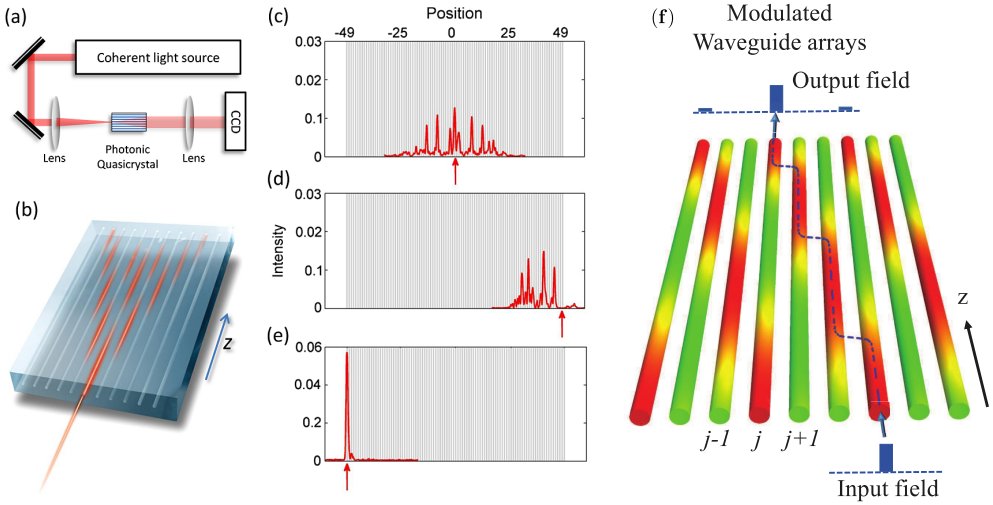

Figura 24 – Observation of topological boundary states in an Aubry-André-Harper photonic quasicrystal. (a) A sketch of the experimental setup. (b) An illustration of the conducted experiment. Light is injected into one of the waveguides and tunnels to neighboring waveguides as it propagates. (c)–(e) Experimental observation of the left boundary state for $\phi = \pi/2$. Light was initially injected into a single waveguide (red arrows). The measured outgoing intensity is plotted versus the injection position along the lattice. (c), (d) An excitation at the middle of the lattice (site 0) and at the rightmost site (site 49) results in a significant spread. (e) For an excitation at the leftmost site (site 49), the light remains tightly localized at the boundary, marking the existence of a boundary state. (f) Schematic view of a photonic modulated waveguide array, which provides an excellent platform for simulating conventional topological systems, as well as for the study of novel topological phases in photonics systems. Taken from Refs. (125) and (126).

reignited. Indeed, one can probe these states in ultracold atoms (116, 129), photonic crystals (125, 130) and even in photonic Fibonacci quasicrystals (131). In addition, adiabatic topological pumping (125, 131, 126) [see Figs. 23 and 24(f)] and discrete-time quantum walks (132, 133) have been investigated in 1D lattices. Also, experimental signatures of Majorana fermions have been identified in several 1D topological superconductors in the past few years (134, 135, 136).

In this quite general context, the study of trimer lattices has been the object of considerable theoretical (124, 137, 138) and experimental (139) interest because of their unique physical properties and very rich phase diagram (12, 9). Particularly, it has been reported that the existence of edge states located only at one edge (or end) of a Hermitian trimerized lattice, is due to a symmetry of the unit cell, which makes the Berry phase piecewise continuous rather than discrete (138). However, in a typical 1D Hermitian topological insulator, topological invariants take only one value of a discrete set of values, and the bulk-boundary correspondence ensures the appearance of, at least, a pair of localized edge states: one on the left and one on the right. In fact, the capacity to exhibit a single edge state on one side of a system has been recently attributed to

non-Hermitian systems (140), where the bulk-boundary correspondence is subject of intense debate and controversy (140, 141, 142, 143, 144).

6.1 Motivation

Motivated by the ability of photonic lattices to realize various optical devices (145), here we consider a simple, paradigmatic and nontrivial model consisting of a one-dimensional lattice with a three-site basis and examine in detail the edge states and their topological character. Interestingly, this model exhibits diverse in-gap edge states as the parameters are varied:

1. Chiral edge states, i.e., states that are localized only on one edge of the system without a counterpart on the opposite edge at the same energy, and which can be used for manipulating fundamental properties of light in a controllable way.

2. Usual topological states, i.e., one on each edge at the same energy.

Originally fueled by the first type of edge states, apparently violating the bulk-boundary correspondence we proceeded to find a subtle connection with the physics of super-lattices. Henceforth, unless otherwise indicated, when talking about chiral edge states we actually mean the edge modes located only at a single edge and belonging to the inversion-symmetry broken phase of the trimer lattice.

In this context, one may wonder, is it possible to relate the existence of these chiral edge states with a topological invariant defined within the bulk? Indeed, as we will show later in this Chapter, the chiral edge states of the trimer chain can be related to bulk topological numbers, but defined in an effective two-dimensional parent system. Furthermore, we show that, the edge states in the inversion-symmetry broken phase of the trimer lattice turn out to be robust against disorder. We also show that the topological phase transition point of the trimer lattice correlates with the topological phase transition in its associated parent system, in which case the Chern numbers are duplicated and their signs change.

This Chapter is organized as follows. In Section 6.2, we discuss general properties of the edge states of the trimer lattice, with special emphasis on those states that are localized only on one edge of the sample without a counterpart on the opposite edge. Moreover, in the Appendix B we apply the recursive boundary Green function method to study the regions in the parameter space where edge states appear. In Section 6.3, we analyze the symmetry exhibited by the trimer lattice and study its consequences for the edge states through the calculation of the Zak phase (146). In Section 6.4, we show that the edge states in the inversion-symmetry broken phase of the trimer lattice turn out to be robust to large amounts of disorder. In Section 6.5, we find a nontrivial correspondence between the chiral edge states of the trimer chain,

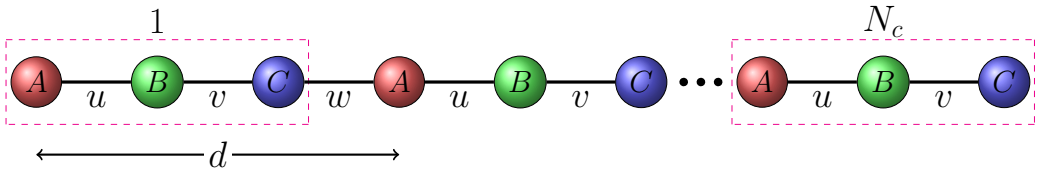

Figura 25 – Scheme representing a finite section of the trimerized lattice model with N_c unit cells, where u and v are the intracell hopping amplitudes, w is the intercell hopping amplitude, and d is the lattice spacing. Each unit cell contains three sites, A, B and C.

with that of an effective 2D model (Aubry-André-Harper model), which shows that the system can host states of topological origin, in much the same way as those in graphene ribbons with zigzag edges (147). Also, we show that, due to this subtle connection, the topological phase transition point of the trimer lattice allows us to find the corresponding topological phase transition point in its associated (two-dimensional) parent system.

6.2 The trimer chain

Consider a system of spinless (or spin-polarized) electrons hopping on a one-dimensional chain composed of N_c unit cells. Each unit cell hosts three distinct sites, which we denote as A, B and C (see illustration in Fig. 25); hence we can expect to find three bands. The length of the unit cell is set to unity ($d = 1$). We can model this trimerized lattice by the following tight-binding Hamiltonian:

$$H = \sum_{n=1}^{N_c} (u c^\dagger_{A,n} c_{B,n} + v c^\dagger_{B,n} c_{C,n} + w c^\dagger_{C,n} c_{A,n+1} + \text{h.c.}), \tag{6.1}$$

where $c^\dagger_{\alpha,n}$ ($c_{\alpha,n}$) denotes the creation (annihilation) operator at site α (which can be either A, B or C type) of the n-th unit cell and u and v are the intracell hopping amplitudes, whereas w is the intercell hopping amplitude. Assuming periodic boundary conditions (discrete translational invariance) along the length of the chain and performing Fourier transform of creation/annihilation operators,

$$\psi_n = (1/\sqrt{N_c}) \sum_k e^{ikn} \psi_k, \tag{6.2}$$

with $\psi_n = (c_{A,n}, c_{B,n}, c_{C,n})^T$, we can write the Hamiltonian in reciprocal space as $H = \sum_k \psi^\dagger_k H(k) \psi_k$, where

$$H(k) = \begin{pmatrix} 0 & u & we^{-ik} \\ u & 0 & v \\ we^{ik} & v & 0 \end{pmatrix}. \tag{6.3}$$

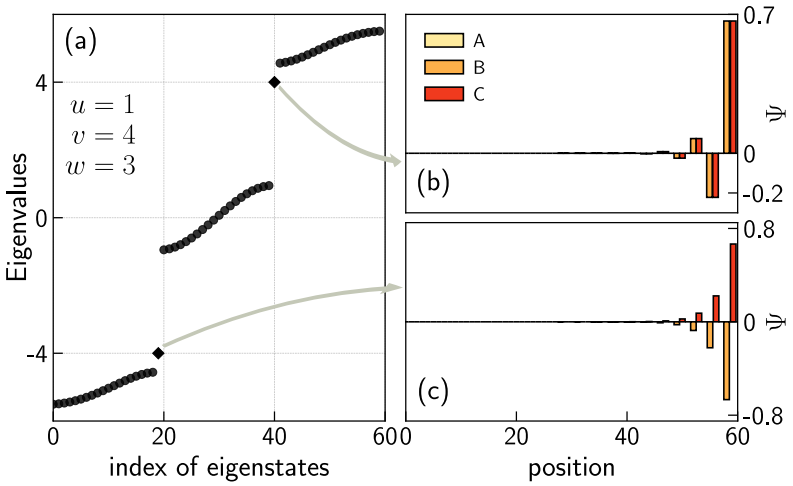

Figura 26 – Energy spectrum and wave functions of the Hamiltonian of Eq. (6.1) with open boundary conditions for $N_c = 20$ unit cells. (a) Energy spectrum of the system for intracell hopping amplitudes $u = 1$, $v = 4$ and intercell hopping amplitude $w = 3$. Panels (b) and (c) show the wave functions of the two edge states with energies $\varepsilon = \pm 4$, both marked as black diamonds in (a), localized on the right boundary of the system, respectively.

The spectrum of the above Hamiltonian consists of three dispersive bands, which only touch each other at the boundaries of the first Brillouin zone (BZ), $k = 0$ and π, when $|u| = |v| = |w|$, i.e., in the absence of trimerization. As the parameters are shifted from that condition, two band gaps appear in the band structure, both with the same value. Interestingly, these band gaps may host very peculiar edge states as those shown in Fig. 26, where we have plotted the energy spectrum of a finite trimer lattice for a set of hopping values of $u = 1$, $v = 4$, and $w = 3$.

Note the presence of two in-gap edge states, with energies $\varepsilon = \pm 4$, both localized on the right boundary of the system, with probability distribution at sites of type B and C [see Figs. 26(b) and 26(c)]. It is worth noting that our system does not exhibit chiral symmetry, and unlike the states in the Su-Schrieffer-Heeger (SSH) model (148, 106), the states shown in Figs. 26(b) and 26(c) are chiral in the sense that they are present on one edge of the sample, but not on the opposite edge. In this context, as we will show in Section 6.5, these states can be interpreted as inherited from a higher dimension, through a mapping onto an effective 2D model, which in fact presents robust chiral states along the edges.

In Fig. 27 we show the energy spectrum of a finite trimer lattice with $N_c = 20$ unit cells, as a function of the intercell hopping amplitude w, and with intracell hopping amplitudes of $u = 1$ and $v = 2$. We can observe a different number of in-gap edge states emerging as w changes. A closer analysis reveals three different regions, as shown in Fig. 27. The first one (white leftmost region) with no edge states for $w < u$,v, the second one [red (dark gray) middle region] with two edge states localized on the right boundary of the system for $u < w < v$, and the last one [yellow (light gray) rightmost region] with

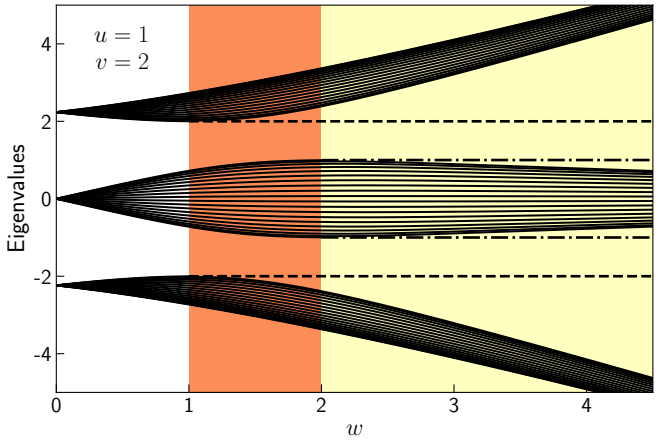

Figura 27 – Energy spectrum of the system under open boundary condition as a function of the intercell hopping amplitude w, for $N_c = 20$ unit cells and intracell hopping amplitudes of $u = 1$ and $v = 2$ (inversion-symmetry broken phase). The bulk states correspond to solid lines, whereas the edge states localized on the right (left) boundary are denoted with dashed (dash-dotted) lines. We highlight three different regions: white leftmost region with no edge states ($w < u$,v), red (dark gray) middle region with two in-gap edge states localized on the right boundary ($u < w < v$), and yellow (light gray) rightmost region with two pairs of edge states localized on both edges of the system (u,$v < w$).

two pairs of edge states localized on both ends of the system for $u < v < w$. Depending on whether $u < w < v$ or $v < w < u$, edge states will appear localized on the right or left boundaries of the system, respectively. Here we assume that $0 < u$,v,w for simplicity, but results can be easily derived in the general case. In fact, we use a recursive boundary Green function method (149) (see the Appendix B for details) to study the regions in the parameter space where edge states appear in a general framework.

This apparent violation of the bulk-boundary correspondence, also reported in Ref. (138) as two new phases characterized by piecewise continuous Berry phases, motivates us to look closer at this problem. In the following, we explore the localization properties and topological nature of the in-gap states.

6.3 Inversion-symmetric trimer chain

A general result of the classification of noninteracting topological phases (150, 151, 152) is that topological phases of matter in 1D can only exist through the imposition of symmetries on the system. Hence, in 1D and in the presence of either chiral (150, 151, 152, 153, 154) or inversion symmetry (155), topological phases will be protected as long as the symmetry is preserved. Therefore, it is convenient to analyze the symmetries of the Hamiltonian, which will allow us to determine if there is any symmetry protected topological phase.

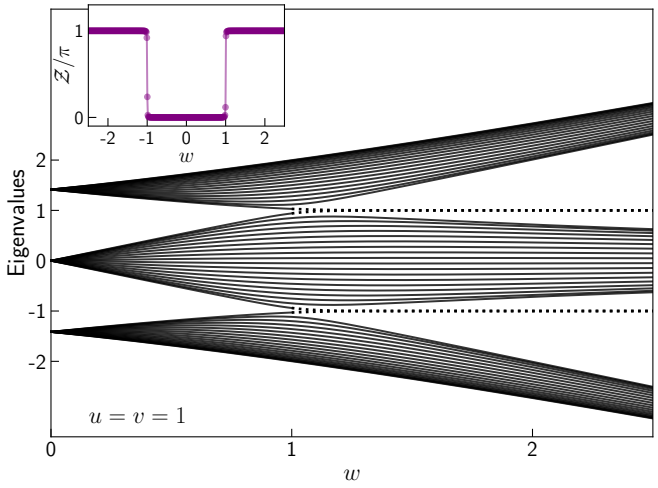

Figura 28 – Energy spectrum and Zak phase (inset) of the system under open boundary condition as a function of the intercell hopping amplitude w, for $N_c = 20$ unit cells and intracell hopping amplitudes $u = v = 1$ (inversion-symmetric phase). The bulk states correspond to solid lines, whereas edge states localized on both ends of the system are denoted with dotted lines. Note that, when the inversion symmetry is preserved, $|w| > 1$ ($|w| < 1$) corresponds to the topological (non-topological) phase of the trimer lattice.

Similar to the chirally symmetric (Hermitian) SSH model, the topological properties of the trimerized chain are regulated by the relative strength of the intercell and intracell hopping amplitudes. In contrast, important distinct features appear since the unit cells of the two models are different. For $u = v$, $H(k)$ is inversion symmetric, with the inversion center lying at the midpoint B between two sites A and C within a unit cell, i.e., $PH(k)P^{-1} = H(-k)$, where the inversion operator

$$P = \begin{pmatrix} 0 & 0 & 1 \\ 0 & 1 & 0 \\ 1 & 0 & 0 \end{pmatrix}, \; P^2 = 1; \; P = P^{-1}, \tag{6.4}$$

plays the equivalent role as the σ_x operator for the SSH model (106).

As mentioned before, if the spatial dimension is one and if no symmetry is assumed, there are no topological phases (150, 151, 152), i.e., all gapped Hamiltonians in 1D are equivalent to the same trivial phase. However, in 1D and in the presence of inversion symmetry P, one can classify different insulators by $\mathbb{Z}$, through a quantized topological index which can take only the values zero or π (modulo 2π), denoting the trivial and nontrivial topological insulators, respectively. This 1D topological invariant, which is intimately related to the existence of edge states through the bulk-boundary correspondence, is usually called the Zak phase (146, 147, 156) and is defined as $\mathcal{Z} = i \int_{-\pi}^{\pi} dk \langle \psi_k | \partial_k \psi_k \rangle$, where ψ_k are the Bloch wave functions. The Zak phase for the

lower band can be computed and is found to be

$$\mathcal{Z} = \begin{cases} 0 & \text{if } |u| = |v| > |w| \\ \pi & \text{if } |u| = |v| < |w| \end{cases}. \tag{6.5}$$

A nontrivial Zak phase implies that a pair of topologically protected edge states will appear at the boundaries of the system, one on the right and one on the left when we cut the chain. Figure. 28 shows the spectrum of the Hamiltonian under open boundary conditions for $|u| = |v| = 1$ (inversion-symmetric phase) as a function of w. A direct manifestation of the nontrivial Zak phase of π is the degenerate gapless modes (dotted black lines), with energies $\varepsilon = \pm 1$, appearing at the boundaries of the system. As we can see the two regions $|u| = |v| < |w|$ and vice versa correspond to two topologically distinct phases, i.e., the system undergoes a topological phase transition with gap closing at $|u| = |v| = |w|$, from a trivial insulator to an inversion symmetry protected topological insulator. This is a common example of a topological phase transition with gap closing, as one cannot continuously switch between the two phases without either closing the bulk energy gaps or breaking the inversion symmetry. It is worth noting that the spectrum depicted in Fig. 28 resembles that of the SSH model very closely. In fact, both are symmetrically arranged around zero energy and have in-gap edge states protected by inversion or chiral symmetry, which appear after the gap-closing-and-reopening transition (106).

Lastly, and similarly to the SSH model, the topological phase transition and edge states emergence in the trimer lattice (with $u = v$) can also be studied using the low-energy continuum theory (157). As mentioned before, the low-energy excitations of the trimer model are close to $k = 0$ and $k = \pi$. Near the band degeneracy point (where two bands cross) we can treat the other band as a perturbation. This procedure, together with an expansion around these points, generates two effective two-band Hamiltonians. Then, if we place a domain wall at $x = 0$, i.e., a Dirac mass term of the form:

$$m(x) = \begin{cases} > 0 & \text{for } x > 0 \\ < 0 & \text{for } x < 0 \end{cases}, \tag{6.6}$$

separating the two insulating phases, we can obtain a set of Dirac-like equations, leading to a solitonic solution with energies $E = u$ for $k = \pi$ and $E = -u$ for $k = 0$. These solutions describe the edge modes living at the domain wall, with the topological phase transition corresponding to the sign change of the Dirac mass term (157).

6.4 Edge states and robustness to disorder

Because of the bulk-boundary correspondence in Hermitian systems, nontrivial topological invariants imply the existence of gapless states exponentially localized at

the boundaries of the sample (gap closing at the transition; see Fig. 28). Thus, when the inversion symmetry is broken, it seems natural to expect the disappearance or at least the instability of these states. However, as seen in Figs. 26 and 27, there are still in-gap states which are localized only at one boundary of the system without an equivalent one at the opposite end. Also, as the robustness against disorder is a characteristic feature of edge states in the topological insulator phase, a natural question arises as to whether these chiral edge states are robust to disorder or not, since they are not protected by any symmetry.

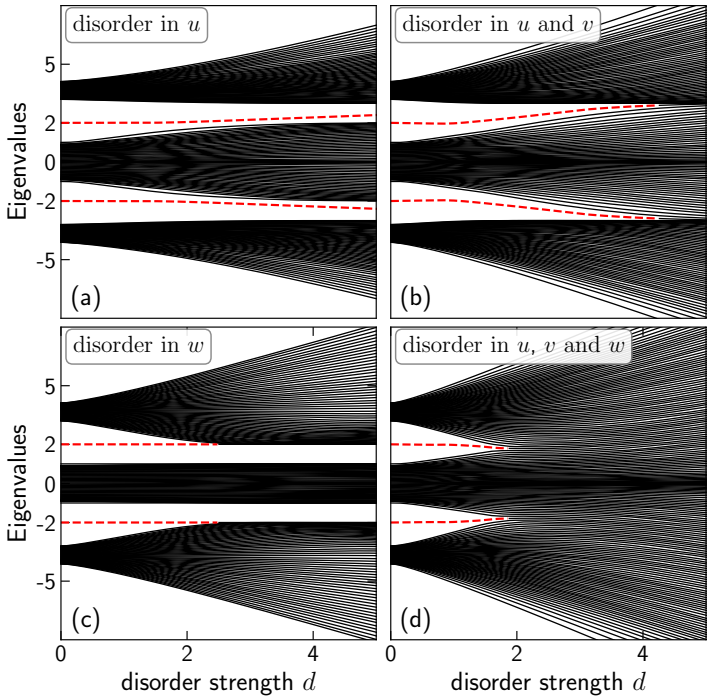

Figura 29 – Energy spectrum of a finite trimer lattice with $N_c = 60$ unit cells, under the effect of increasing amounts of disorder d: (a) in u, (b) in u and v, (c) in w, and (d) in u, v, and w. Dashed red lines indicate the right edge states. The starting points for all plots are $u = 1$, $v = 2$, and $w = 3$ (inversion-symmetry broken phase), and the results are the average over 100 simulations.

In order to gain insight into this question, we numerically investigate the robustness of the edge states against disorder in the inversion-symmetry broken phase of the trimer lattice. The Hamiltonian of Eq. (6.1) contains three hopping parameters: u, v and w on which we introduce random disorder, i.e., $u_n = u + d\gamma_n$, $v_n = v + d\gamma_n$ and $w_n = w + d\gamma_n$, where n is the cell index, γ_n is uniformly distributed between 1 and -1 and d is the disorder strength. For the sake of generality, we also allow the disorder to be different for each unit cell, and act on the hopping parameters u, v, and w independently.

Figure. 29 shows the results, averaged over 100 simulations, for four types of disorder as a function of the disorder strength d. The starting points for all plots are $u = 1$, $v = 2$ and $w = 3$. Disorder in the intracell hopping u and intercell hopping w is depicted in Figs. 29(a) and 29(c), respectively. On the other hand, in Fig. 29(b) we allow disorder to

act on u and v, independently. Lastly, Fig. 29(d) shows the spectrum of the system with disorder acting in u, v, and w, also independently.

We can observe that, even when details of the spectrum are modified, and the robustness of the right edge states (dashed red lines in Fig. 29) against the disorders are slightly different, the localized nature of the edge states remain. Moreover, the eigenvalues (of the right edge states) remain at $\varepsilon = \pm v$ until the disorder is strong enough to either cause the eigenvalues to reach the band (becoming extended) or close the band gap. Remarkably, these edge states are robust to large amounts of disorder and, as we will see next, we can associate a topological origin to them, originated from a map onto an effective model in a higher dimension. This contrasts with the case of the edge states of zigzag graphene ribbons, which have a topological origin rooted in a lower dimension (147), but are fragile to disorder.

6.5 Topological origin of edge states in the inversion-symmetry broken phase

The bulk-boundary correspondence dictates the existence of gapless edge states from bulk topological invariants. Remarkably, depending on the values of the hopping amplitudes, the trimer lattice can exhibit diverse in-gap edge states which "apparently" violate the bulk-boundary correspondence, i.e., states appear localized only at one end of the system without a counterpart at the opposite end. This, combined with the fact that these edge states turn out to be robust against disorder, makes one wonder about the bulk-boundary correspondence, and the nature/origin of these edge states in such a system.

To answer these questions and motivated by the fact that families of 1D band insulators, i.e., systems where the Hamiltonian depend periodically on a parameter ϕ (defining an effective 2D model), share the same topological classification as the quantum Hall effect (158, 125, 128), we model the trimer lattice through the so-called commensurate off-diagonal Aubry-André-Harper (AAH) model (159, 160). Before studying this specific Hamiltonian, it is important to add some general comments about the physics of AAH models involving diagonal and off-diagonal modulation terms, specifically, with regard to their topology. In Ref. (161) the authors have analytically proved the topological equivalence of incommensurate AAH models, regardless of whether the quasiperiodicity appears as an on-site (diagonal) or hopping (off-diagonal) modulation. This contrasts with the commensurate diagonal and off-diagonal AAH models, in which case there are regions in parameter space where the two models have different topological invariants (Chern numbers), implying that, in general, they are not topologically equivalent (126), as one cannot continuously deform from one into the other without closing the energy gap.

The commensurate off-diagonal AAH model can be described by the following tight-binding Hamiltonian:

$$H = \sum_{n=1}^{N} t[1 + \lambda \cos(2\pi bn + \phi) c_{n+1}^{\dagger} c_n] + \text{h.c.}, \tag{6.7}$$

where N is the number of lattice sites, $c_n^{\dagger}$ (c_n) is the creation (annihilation) operator at site n, t is the hopping amplitude which is set to be the unit of the energy ($t = 1$), and the parameter λ is the modulation amplitude of the coupling strength. The modulation periodicity is controlled by $b = p/q$ (p and q are coprime numbers), leading to a commensurate (incommensurate) modulation with the lattice, whenever b is rational (irrational). Here, our interest is to discuss the case of b rational or, more specifically, $p = 1$ and $q = 3$ ($b \equiv 1/3$), which leads to a trimerized model with three bands. On the other hand, the phase factor ϕ plays the role of an additional degree of freedom, which in our case allows us to obtain a whole family of different trimers.

A family of trimers, i.e., $\{H(\phi)|0 \leq \phi < 2\pi\}$, defines an effective model in two dimensions. Therefore, identifying ϕ as one component of the wave vector of a 2D system, we can map this 1D model to a 2D model, in such a way that the topological properties of our 1D trimer chain can be easily studied by using topological concepts for 2D systems (123, 125). Hence, assuming periodic boundary conditions on the system, Eq. (6.7), and performing Fourier transforms of creation/annihilation operators, Chern numbers for individual (n-th) bands can be defined in an effective 2D space, (k,ϕ), over the BZ $(0 \leq k < 2\pi/q, 0 \leq \phi < 2\pi)$ as

$$\nu_n = \frac{1}{2\pi} \int_0^{2\pi/q} dk \int_0^{2\pi} d\phi \left(\partial_k A_\phi - \partial_\phi A_k \right), \tag{6.8}$$

with the Berry connection $A_r = i \langle \psi(k,\phi) | \partial_r | \psi(k,\phi) \rangle$ ($r = k,\phi$), where $\psi(k,\phi)$ are the Bloch wave functions. We numerically calculate the Chern numbers for individual bands as a function of λ. We found that, when the modulation amplitude, $\lambda < \lambda_c$, the Chern numbers are $(\nu_1,\nu_2,\nu_3) = (-1,2,-1)$, while for $\lambda > \lambda_c$ the Chern numbers are $(\nu_1,\nu_2,\nu_3) = (2,-4,2)$, with $\lambda_c = 4$, predicting a topological phase transition where not only are the Chern numbers doubled, but they also change in sign, in agreement with results derived in the context of Thouless pumping (126). As noted in Ref. (126) this means that, if we perform a particle pumping experiment along the lattice, the propagation direction will change by the opposite, and it will be faster.

Figure. 30 shows the energy spectrum of the commensurate off-diagonal AAH model under open boundary condition for a lattice of finite length, $N = 60$, and two values of λ: Fig. 30 (a) for $\lambda = 0.5$ and Fig. 30 (b) for $\lambda = 5$. The bulk Bloch states are denoted with solid lines, whereas the edge states localized at the right (left) boundary correspond to dashed (dash-dotted) lines. By keeping $b = 1/3$ and scanning ϕ from zero to 2π one can observe in Fig. 30(a) that the two gaps are closed by a few modes,

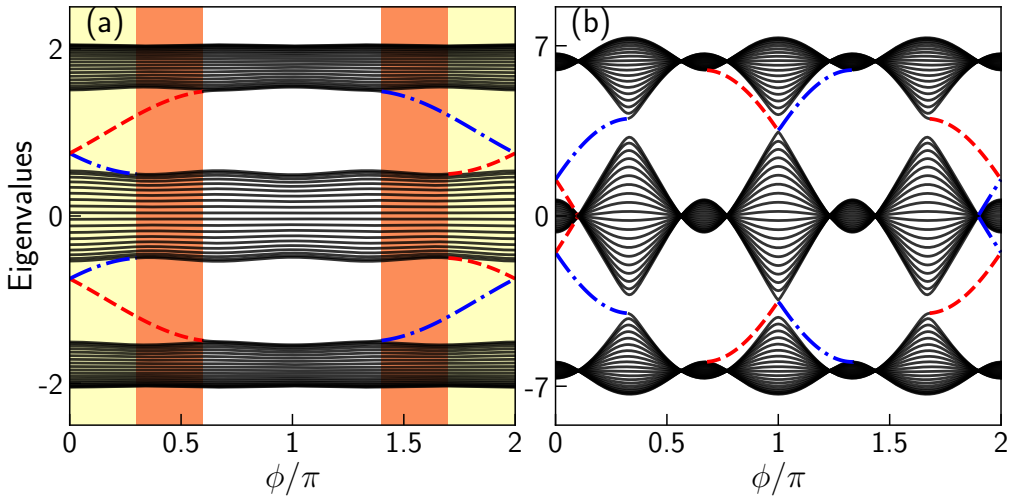

Figura 30 – Energy spectrum of the commensurate off-diagonal AAH model, Eq. (6.7), under open boundary condition as a function of ϕ, for $b = 1/3$, $N = 60$ sites, and two different values of λ: (a) $\lambda = 0.5$ and (b) $\lambda = 5$. The bulk Bloch states correspond to solid lines, whereas the edge states localized on the right (left) boundary are denoted with dashed (dash-dotted) lines. Note the correspondence between the highlighted yellow (light gray) and red (dark gray) areas in (a) and those in Fig. 27. Chern numbers for individual bands are: (a) $(\nu_1,\nu_2,\nu_3) = (-1,2,-1)$ before the transition and (b) $(\nu_1,\nu_2,\nu_3) = (2,-4,2)$ after the transition point, $\lambda_c = 4$.

reproducing all possible configurations that appear in Fig. 27. Indeed, each value of $\phi \in [0,2\pi)$ corresponds to a certain set of hopping values, that is, each cut as a function of ϕ defines a trimer. In Fig. 30(a) we have highlighted in white, red (dark gray), and yellow (light gray) the corresponding regions where there are no edge states, two edge states located either at the right (dashed lines) or left (dash-dotted lines) boundary of the system, and two pairs of edge states localized on both ends of the system, respectively. It is worth noting the correspondence between the highlighted yellow (light gray) and red (dark gray) areas in Fig. 30(a) and those in Fig. 27, in terms of localization and number of edge states. Also notice that the number of edge modes in Fig. 30(b) is twice that in Fig. 30(a), while the propagation direction is the opposite.

The individual members of the trimer's family are not topological in general, although they exhibit states located at the boundaries of the system. As discussed in Section 6.3, only when the inversion symmetry is preserved is an element of the family topological. These are the cases that have a crossing at the inversion-symmetry point, indicating the emergence of degenerate edge states protected by the inversion symmetry. On the other hand, only when scanning ϕ from zero to 2π we can obtain all the possible variants that the trimer lattice can assume. This suggests that the appearance of the chiral states has a topological origin because they are associated with a whole family, and only as a whole family we can define invariants (Chern numbers) and establish a bulk-boundary correspondence.

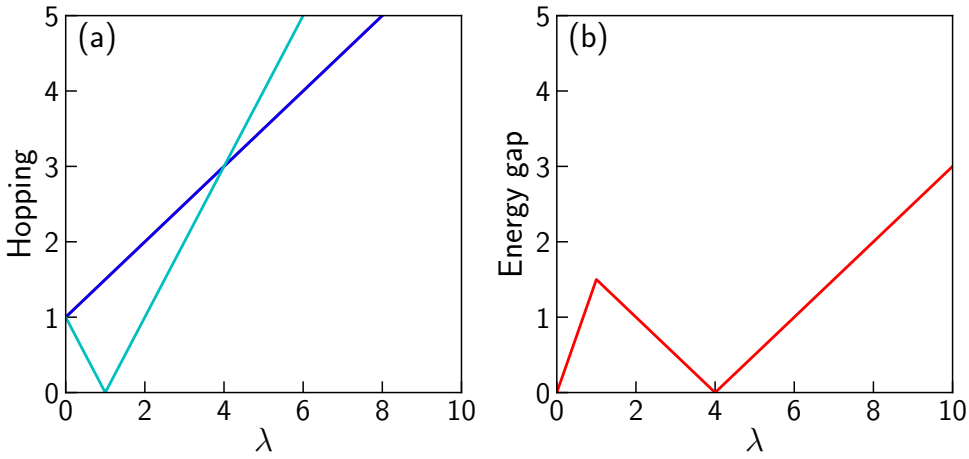

Figura 31 – (a) Hopping amplitudes and (b) energy gaps for the commensurate off-diagonal AAH model as a function of λ, for $b = 1/3$. In panel (a) the blue and cyan lines stand for u and w hopping amplitudes when $\phi = \pi$ ($u \equiv v$ for $\phi = \pi$), respectively. Note that the point of intersection between the two hopping amplitudes defines the transition point $\lambda_c = 4$. In panel (b) the two energy gaps shown in both Figs. 30(a) and 30(b) undergo a closing-and-reopening transition at $\lambda_c = 4$.

As mentioned before, as the hopping amplitude λ increases, the system undergoes a topological phase transition (126). The topological phase transition point can be found, analytically, by solving a cubic equation that results from Eq. (6.7) assuming periodic boundary conditions and $b = 1/3$ (126). Here we put forward an interesting connection between the transition point in 1D and 2D, whereby the precise determination of the closing gap and the transition point in 1D, correctly determines the corresponding position of closing gap and transition point in 2D, a property which can be extended to other systems with rational b and odd q.

The topological phase transition in the trimer lattice, as we saw in Section 6.3, occurs when $|u| = |v| = |w|$; thus the position corresponding to the closing gap in the effective 2D system is not changed, only modulated. In this way, we can identify

$$u = 1 + \lambda \cos(2\pi/3 + \phi), \tag{6.9}$$

$$v = 1 + \lambda \cos(4\pi/3 + \phi), \tag{6.10}$$

$$w = 1 + \lambda \cos(\phi). \tag{6.11}$$

The hopping amplitudes u and v are always equal when the phase factor is $\phi = \pi$; then we have $u = v = 1 + \lambda/2$ and $w = 1 - \lambda$. In fact, by equating

$$|1 + \lambda/2| = |1 - \lambda|, \tag{6.12}$$

we obtain the critical value $\lambda_c = 4$ for the topological phase transition [see Fig. 31(a)], in full agreement with that found in Ref. (126) in the context of Thouless pumping of

light in photonic waveguide arrays. Furthermore, as the topological phase transition is associated with an energy gap closing, we also calculate the evolution of the energy gap as a function of λ. The energy gap between the n-th and $(n+1)$-th bands, defined as $\triangle E_n = \min(E_{n+1} - E_n)$, is shown in Fig. 31(b). Lastly, we want to emphasize that this connection reinforces our suggestion that the trimer lattice can host states of topological origin.

Lastly, we remark that the main results of Part II form the body of a recent publication in Physical Review A, entitled *"Edge states in trimer lattices"* (162).

7 CONCLUSIONS

In the first part of this Thesis, we have presented a detailed analytical study of the large-U Hubbard model on the quasi-one-dimensional AB_2 chain. We used a functional integral approach combined with a perturbative expansion in the strong-coupling regime that allowed us to properly analyze the referred system at and away from half filling. The phenomenological motivation was largely discussed and a variety of compounds were mentioned, particularly those materials in which the line of trimers formed by spin-1/2 Cu^{+2} ions exhibit ferrimagnetism of topological origin. Therefore, the study of doping-induced phases on these materials appears as a promising challenge. At half filling, our model was mapped onto the quantum Heisenberg model, and its Lieb ferrimagnetic GS was analyzed through a spin-wave perturbative series expansion in powers of $1/S$. We have demonstrated that the GS energy, spin-wave modes, and sublattice magnetizations are in very good agreement with previous results. In the challenging hole doping regime away from half filling, the corresponding t-J Hamiltonian was derived. Further, under the assumption that charge and spin quantum correlations are decoupled, the evolution of the second-order spin-wave modes in the doped regime has unveiled the occurrence of spatially modulated spin structures and the emergence of phase separation in the presence of resonating-valence-bond states. The doping-dependent GS energy and total spin per unit cell, including both Zeeman and orbital contributions where also calculated, in which case the collapse of the spiral magnetic order at a critical hole concentration was observed. It is surprising and very interesting that the second-order spin- wave modes remain stable up to $\delta = 1/3$. Remarkably, our above-mentioned analytical results in the doped regime are in very good agreement with recent density matrix renormalization group studies, where our assumption of spin-charge decoupling is numerically supported by the formation of charge-density waves in anti-phase with the modulation of the ferrimagnetic structure. The comparison between the numerical and analytical findings have provided deep insights on underlying mechanisms associated with several quantities and phases at both the microscopic and macroscopic levels.

The reported results evidenced that the present approach, also used in a study on the compatibility between numerical and analytical outcomes of the large-U Hubbard model on the honeycomb lattice, was proved suitable for the AB_2 chain (a quasi-1D system), where the impact of charge and spin quantum fluctuations are expected to manifest in a stronger way. We thus conclude that our approach offers a quite powerful analytical description of hole-doping induced phases away from half filling in low-dimensional strongly-correlated electron systems, including superconducting ground states.

In the second part, motivated by analogy with photonic lattices, we have studied the edge states of a one-dimensional trimer lattice and examined its characteristics in the phases with and without inversion symmetry protection. Remarkably, we have shown that the edge states in the inversion-symmetry broken phase of the trimer model may appear located at a single edge. In particular, the emergence of degenerate edge states in the inversion-symmetric phase of the trimer model has been characterized through the calculation of the Zak phase. If the inversion symmetry is broken, we have demonstrated that the chiral edge states remain robust to large amounts of disorder. This contrasts, for example, with the case of the edge states of zigzag graphene ribbons which are less robust, and have a topological origin rooted in a lower dimension. In addition, through the mapping onto the commensurate off-diagonal Aubry-André-Harper model, we have captured the essentials of the whole family of trimers, which allows us to establish a direct connection between chiral edge modes in the two models, including the calculation of Chern numbers in this effective two-dimensional model. We thus suggest that the chiral edge modes of the trimer lattice have a topological origin inherited from this effective mapping. We have established a nontrivial connection between the topological phase transition point in the trimer lattice to that in its associated effective two-dimensional parent system. The topological phase transition point found here is in full agreement with results derived in the context of topological Thouless pumping in photonic lattices. This nontrivial connection strengthens our suggestion that the trimer lattice, in the inversion-symmetry broken phase, can host states of topological origin.

REFERENCES

[1] ANDERSON, P. W. More Is Different. *Science*, Washington, v. 177, n. 4047, p. 393–396, 1972.

[2] SACHDEV, S. *Quantum Phase Transitions*. Second. ed. Cambridge University Press, 2011.

[3] GIAMARCHI, T. *Quantum Physics in One Dimension*. Clarendon; Oxford University Press, 2004.

[4] CONTINENTINO, M. A. *Quantum Scaling in Many-Body Systems: An Approach to Quantum Phase Transitions*. 2. ed. Cambridge University Press, 2017.

[5] BAYM, G.; PETHICK, C. *Landau Fermi-liquid theory: concepts and applications*. John Wiley & Sons, 2008.

[6] HALDANE, F. D. M. 'Luttinger liquid theory' of one-dimensional quantum fluids. I. Properties of the Luttinger model and their extension to the general 1D interacting spinless Fermi gas. *J. Phys C*, v. 14, n. 19, p. 2585, 1981.

[7] COUTINHO-FILHO, M. D.; MONTENEGRO-FILHO, R. R.; RAPOSO, E. P.; VITORIANO, C.; OLIVEIRA, M. H. Magnetism and electronic correlations in quasi-one-dimensional compounds. *J. Braz. Chem. Soc.*, v. 19, p. 232, 2008.

[8] IVANOV, N. B. Spin models of quasi-1D quantum ferrimagnets with competing interactions. *Condensed Matter Phys*, v. 12, n. 3, p. 435–447, 2009.

[9] MONTENEGRO-FILHO, R. R.; COUTINHO-FILHO, M. D. Magnetic and non-magnetic phases in doped AB_2 *t-J* Hubbard chains. *Phys. Rev. B*, v. 90, p. 115123, Sep 2014.

[10] MONTENEGRO-FILHO, R. R.; COUTINHO-FILHO, M. D. Quasi-one-dimensional quantum ferrimagnets. *Physica A*, Amsterdam, v. 357, n. 1, p. 173, 2005.

[11] SILVESTRE, J.; HOFFMANN, R. Tetrahedral and square-planar one-dimensional chains: the interplay of crystal field and band width in MS2 compounds. *Inorg. Chem.*, v. 24, n. 24, p. 4108, 1985.

[12] MACÊDO, A. M. S.; DOS SANTOS, M. C.; COUTINHO-FILHO, M. D.; MACÊDO, C. A. Magnetism and Phase Separation in Polymeric Hubbard Chains. *Phys. Rev. Lett.*, v. 74, p. 1851–1854, Mar 1995.

[13] TIAN, G.-S.; LIN, T.-H. Quasi-one-dimensional organic unsaturated ferromagnetism: Some rigorous results. *Phys. Rev. B*, v. 53, p. 8196, Apr 1996.

[14] ALCARAZ, F. C.; MALVEZZI, A. L. Critical behaviour of mixed Heisenberg chains. *J. Phys. A*, v. 30, n. 3, p. 767, 1997.

[15] RAPOSO, E. P.; COUTINHO-FILHO, M. D. Quantum Critical Properties of Ferrimagnetic Hubbard Chains. *Phys. Rev. Lett.*, v. 78, p. 4853, Jun 1997.

[16] RAPOSO, E. P.; COUTINHO-FILHO, M. D. Field theory of ferrimagnetic Hubbard chains. *Phys. Rev. B*, v. 59, p. 14384, Jun 1999.

[17] SIERRA, G.; MARTÍN-DELGADO, M. A.; WHITE, S. R.; SCALAPINO, D. J.; DUKELSKY, J. Diagonal ladders: A class of models for strongly coupled electron systems. *Phys. Rev. B*, v. 59, p. 7973, Mar 1999.

[18] MARTÍN-DELGADO, M. A.; RODRIGUEZ-LAGUNA, J.; SIERRA, G. Universality classes of diagonal quantum spin ladders. *Phys. Rev. B*, v. 72, p. 104435, Sep 2005.

[19] LIEB, E.; MATTIS, D. Ordering Energy Levels of Interacting Spin Systems. *J. Math. Phys.*, v. 3, n. 4, p. 749, 1962.

[20] LIEB, E. H.; WU, F. Y. Absence of Mott Transition in an Exact Solution of the Short-Range, One-Band Model in One Dimension. *Phys. Rev. Lett.*, v. 20, p. 1445, Jun 1968.

[21] LIEB, E. H. Two theorems on the Hubbard model. *Phys. Rev. Lett.*, v. 62, p. 1201, Mar 1989.

[22] E. H. Lieb, in *The Hubbard Model: Its Physics and Mathematical Physics,* Nato ASI, Series B: Physics, edited by D. Baeriswyl, D. K. Campbell, J. M. P Carmelo, F. Guinea and E. Louis. Plenum, New York, 1995. v. 343.

[23] TASAKI, H. The Hubbard model - an introduction and selected rigorous results. *J. Phys. Condens. Matter*, v. 10, n. 20, p. 4353, 1998.

[24] TASAKI, H. From Nagaoka's Ferromagnetism to Flat-Band Ferromagnetism and Beyond: An Introduction to Ferromagnetism in the Hubbard Model. *Prog. Theor. Phys.*, v. 99, n. 4, p. 489, 1998.

[25] TIAN, G.-S. Lieb's Spin-Reflection-Positivity Method and Its Applications to Strongly Correlated Electron Systems. *J. Stat. Phys.*, v. 116, n. 1, p. 629, 2004.

[26] YAMAMOTO, S.; OHARA, J. Low-energy structure of the homometallic intertwining double-chain ferrimagnets $A_3Cu_3(PO_4)_4$ (A = Ca,Sr,Pb). *Phys. Rev. B*, v. 76, p. 014409, Jul 2007.

[27] MONTENEGRO-FILHO, R. R.; COUTINHO-FILHO, M. D. Frustration-induced quantum phase transitions in a quasi-one-dimensional ferrimagnet: Hard-core boson map and the Tonks-Girardeau limit. *Phys. Rev. B*, v. 78, p. 014418, Jul 2008.

[28] HIDA, K.; TAKANO, K. Frustration-induced quantum phases in mixed spin chain with frustrated side chains. *Phys. Rev. B*, v. 78, p. 064407, Aug 2008.

[29] SHIMOKAWA, T.; NAKANO, H. Ferrimagnetism of the Heisenberg Models on the Quasi-One-Dimensional Kagome Strip Lattices. *J. Phys. Soc. Jpn*, v. 81, n. 8, p. 084710, 2012.

[30] FURUYA, S. C.; GIAMARCHI, T. Spontaneously magnetized Tomonaga-Luttinger liquid in frustrated quantum antiferromagnets. *Phys. Rev. B*, v. 89, p. 205131, May 2014.

[31] MONTENEGRO-FILHO, R. R.; COUTINHO-FILHO, M. D. Doped AB_2 Hubbard chain: Spiral, Nagaoka and resonating-valence-bond states, phase separation, and Luttinger-liquid behavior. *Phys. Rev. B*, v. 74, p. 125117, Sep 2006.

[32] ESSLER, F. H. L.; FRAHM, H.; GÖHMANN, F.; KLÜMPER, A.; KOREPIN, V. E. *The one-dimensional Hubbard model*. Cambridge University Press, 2005.

[33] CARMELO, J. M. P.; SACRAMENTO, P. D. Pseudoparticle approach to 1D integrable quantum models. *Phys. Rep.*, v. 749, p. 1 – 90, 2018.

[34] HALDANE, F. D. M. "Fractional statistics" in arbitrary dimensions: A generalization of the Pauli principle. *Phys. Rev. Lett.*, v. 67, p. 937, Aug 1991.

[35] WU, Y.-S. Statistical distribution for generalized ideal gas of fractional-statistics particles. *Phys. Rev. Lett.*, v. 73, p. 922–925, Aug 1994.

[36] VITORIANO, C.; MONTENEGRO-FILHO, R. R.; COUTINHO-FILHO, M. D. Fractional exclusion statistics and thermodynamics of the Hubbard chain in the spin-incoherent Luttinger liquid regime. *Phys. Rev. B*, v. 98, p. 085130, Aug 2018.

[37] LOPES, A. A.; DIAS, R. G. Interacting spinless fermions in a diamond chain. *Phys. Rev. B*, v. 84, p. 085124, Aug 2011.

[38] LOPES, A. A.; ANTÓNIO, B. A. Z.; DIAS, R. G. Conductance through geometrically frustrated itinerant electronic systems. *Phys. Rev. B*, v. 89, p. 235418, Jun 2014.

[39] TORRICO, J.; ROJAS, M.; PEREIRA, M. S. S.; STRE ccKA, J.; LYRA, M. L. Spin frustration and fermionic entanglement in an exactly solved hybrid diamond chain with localized Ising spins and mobile electrons. *Phys. Rev. B*, v. 93, p. 014428, Jan 2016.

[40] MATSUDA, M.; KAKURAI, K.; BELIK, A. A.; AZUMA, M.; TAKANO, M.; FUJITA, M. Magnetic excitations from the linear Heisenberg antiferromagnetic spin trimer system $A_3Cu_3(PO_4)_4$ ($A =$ Ca, Sr, and Pb). *Phys. Rev. B*, v. 71, p. 144411, Apr 2005.

[41] DRILLON, M.; BELAICHE, M.; LEGOLL, P.; ARIDE, J.; BOUKHARI, A.; MOQINE, A. 1D ferrimagnetism in copper(II) trimetric chains: Specific heat and magnetic behavior of $A_3Cu_3(PO_4)_4$ with A = Ca, Sr. *J. Magn. Magn. Mater*, v. 128, n. 1, p. 83, 1993.

[42] BELIK, A. A.; MATSUO, A.; AZUMA, M.; KINDO, K.; TAKANO, M. Long-range magnetic ordering of $S = 1/2$ linear trimers in $A_3Cu_3(PO_4)_4$ ($A =$ Ca, Sr, and Pb) . *J. Solid State Chem.*, v. 178, n. 3, p. 709, 2005.

[43] GUO, W.; HE, Z.; ZHANG, S. Syntheses and magnetic properties of new compounds $Ca_3M_3(PO_4)_4$(M = Ni,Co) with a wave-like layer structure built by zigzag M-chains. *J. Alloys Compd.*, v. 717, p. 14, 2017.

[44] VERDAGUER, M.; GLEIZES, A.; RENARD, J. P.; SEIDEN, J. Susceptibility and magnetization of $CuMn(S_2C_2O_2)_2{\cdot}7.5H_2O$. First experimental and theoretical characterization of a quasi-one-dimensional ferrimagnetic chain. *Phys. Rev. B*, v. 29, p. 5144, May 1984.

[45] TENÓRIO, A. S. F.; MONTENEGRO-FILHO, R. R.; COUTINHO-FILHO, M. D. Quantum phase transitions in alternating spin-($\frac{1}{2}$,$\frac{5}{2}$) Heisenberg chains. *J. Phys. Condens. Matter*, v. 23, n. 50, p. 506003, 2011.

[46] STREČKA, J.; VERKHOLYAK, T. Magnetic Signatures of Quantum Critical Points of the Ferrimagnetic Mixed Spin-(1/2, S) Heisenberg Chains at Finite Temperatures. *J. Low. Temp. Phys*, v. 187, n. 5, p. 712–718, 2017.

[47] YAN, X.; ZHU, Z.-G.; SU, G. Combined study of Schwinger-boson mean-field theory and linearized tensor renormalization group on Heisenberg ferromagnetic mixed spin (S, σ) chains. *AIP Advances*, v. 5, n. 7, p. 077183, 2015.

[48] KIKUCHI, H.; FUJII, Y.; CHIBA, M.; MITSUDO, S.; IDEHARA, T.; TONEGAWA, T.; OKAMOTO, K.; SAKAI, T.; KUWAI, T.; OHTA, H. Experimental Observation of the 1/3 Magnetization Plateau in the Diamond-Chain Compound $Cu_3(CO_3)_2(OH)_2$. *Phys. Rev. Lett.*, v. 94, p. 227201, Jun 2005.

[49] GU, B.; SU, G. Comment on "Experimental Observation of the 1/3 Magnetization Plateau in the Diamond-Chain Compound $Cu_3(CO_3)_2(OH)_2$". *Phys. Rev. Lett.*, v. 97, p. 089701, Aug 2006.

[50] KIKUCHI, H.; FUJII, Y.; CHIBA, M.; MITSUDO, S.; IDEHARA, T.; TONEGAWA, T.; OKAMOTO, K.; SAKAI, T.; KUWAI, T.; OHTA, H. Kikuchi *et al.* Reply:. *Phys. Rev. Lett.*, v. 97, p. 089702, Aug 2006.

[51] OSHIKAWA, M.; YAMANAKA, M.; AFFLECK, I. Magnetization Plateaus in Spin Chains: "Haldane Gap" for Half-Integer Spins. *Phys. Rev. Lett.*, v. 78, p. 1984, Mar 1997.

[52] RULE, K. C.; WOLTER, A. U. B.; SÜLLOW, S.; TENNANT, D. A.; BRÜHL, A.; KÖHLER, S.; WOLF, B.; LANG, M.; SCHREUER, J. Nature of the Spin Dynamics and 1/3 Magnetization Plateau in Azurite. *Phys. Rev. Lett.*, v. 100, p. 117202, Mar 2008.

[53] HASE, M.; KOHNO, M.; KITAZAWA, H.; TSUJII, N.; SUZUKI, O.; OZAWA, K.; KIDO, G.; IMAI, M.; HU, X. 1/3 magnetization plateau observed in the spin-1/2 trimer chain compound $Cu_3(P_2O_6OH)_2$. *Phys. Rev. B*, v. 73, p. 104419, Mar 2006.

[54] AIMO, F.; KRÄMER, S.; KLANJ ssEK, M.; HORVATI cć, M.; BERTHIER, C.; KIKUCHI, H. Spin Configuration in the 1/3 Magnetization Plateau of Azurite Determined by NMR. *Phys. Rev. Lett.*, v. 102, p. 127205, Mar 2009.

[55] JESCHKE, H.; OPAHLE, I.; KANDPAL, H.; VALENTÍ, R.; DAS, H.; SAHA-DASGUPTA, T.; JANSON, O.; ROSNER, H.; BRÜHL, A.; WOLF, B.; LANG, M.; RICHTER, J.; HU, S.; WANG, X.; PETERS, R.; PRUSCHKE, T.; HONECKER, A. Multistep Approach to Microscopic Models for Frustrated Quantum Magnets: The Case of the Natural Mineral Azurite. *Phys. Rev. Lett.*, v. 106, p. 217201, May 2011.

[56] TAKANO, K.; KUBO, K.; SAKAMOTO, H. Ground states with cluster structures in a frustrated Heisenberg chain. *J. Phys. Condens. Matter*, v. 8, n. 35, p. 6405, 1996.

[57] OKAMOTO, K.; TONEGAWA, T.; TAKAHASHI, Y.; KABURAGI, M. Ground state of an $S = 1/2$ distorted diamond chain-model of $Cu_3Cl_6(H_2O)_2 \cdot 2H_8C_4SO_2$. *J. Phys. Condens. Matter*, v. 11, n. 50, p. 10485, 1999.

[58] OKAMOTO, K.; TONEGAWA, T.; KABURAGI, M. Magnetic properties of the S = 1/2 distorted diamond chain at T = 0. *J. Phys. Condens. Matter*, v. 15, n. 35, p. 5979, 2003.

[59] TENÓRIO, A. S. F.; MONTENEGRO-FILHO, R. R.; COUTINHO-FILHO, M. D. Quantum rotors on the AB_2 chain with competing interactions. *Phys. Rev. B*, v. 80, p. 054409, Aug 2009.

[60] FUJIHALA, M.; KOORIKAWA, H.; MITSUDA, S.; MORITA, K.; TOHYAMA, T.; TOMIYASU, K.; KODA, A.; OKABE, H.; ITOH, S.; YOKOO, T.; IBUKA, S.; TADOKORO, M.; ITOH, M.; SAGAYAMA, H.; KUMAI, R.; MURAKAMI, Y. Possible Tomonaga-Luttinger spin liquid state in the spin-1/2 inequilateral diamond-chain compound $K_3Cu_3AlO_2(SO_4)_4$. *Sci. Rep.*, v. 7, n. 1, p. 16785, 2017.

[61] MORITA, K.; FUJIHALA, M.; KOORIKAWA, H.; SUGIMOTO, T.; SOTA, S.; MITSUDA, S.; TOHYAMA, T. Static and dynamic magnetic properties of the spin-$\frac{1}{2}$ inequilateral diamond-chain compounds $A_3Cu_3AlO_2(SO_4)_4(A = K,Rb,Cs)$. *Phys. Rev. B*, v. 95, p. 184412, May 2017.

[62] DAGOTTO, E. Complexity in Strongly Correlated Electronic Systems. *Science*, Washington, v. 309, n. 5732, p. 257–262, 2005.

[63] HAN, T.-R. T.; ZHOU, F.; MALLIAKAS, C. D.; DUXBURY, P. M.; MAHANTI, S. D.; KANATZIDIS, M. G.; RUAN, C.-Y. Exploration of metastability and hidden phases in correlated electron crystals visualized by femtosecond optical doping and electron crystallography. *Sci. Adv.*, v. 1, n. 5, p. e1400173, 2015.

[64] DAGOTTO, E. Experiments on ladders reveal a complex interplay between a spin-gapped normal state and superconductivity. *Rep. Prog. Phys.*, v. 62, n. 11, p. 1525, 1999.

[65] KELLY, Z. A.; GALLAGHER, M. J.; MCQUEEN, T. M. Electron Doping a Kagome Spin Liquid. *Phys. Rev. X*, v. 6, p. 041007, Oct 2016.

[66] MAZIN, I. I.; JESCHKE, H. O.; LECHERMANN, F.; LEE, H.; FINK, M.; THOMALE, R.; VALENTÍ, R. Theoretical prediction of a strongly correlated Dirac metal. *Nat. Commun*, v. 5, p. 4261, 2014.

[67] GUTERDING, D.; JESCHKE, H. O.; VALENTÍ, R. Prospect of quantum anomalous Hall and quantum spin Hall effect in doped kagome lattice Mott insulators. *Sci. Rep*, v. 6, 2016.

[68] MIAO, P.; LIN, X.; LEE, S.; ISHIKAWA, Y.; TORII, S.; YONEMURA, M.; UENO, T.; INAMI, N.; ONO, K.; WANG, Y.; KAMIYAMA, T. Hole-doping-induced melting of spin-state ordering in $PrBaCo_2O_{5.5+x}$. *Phys. Rev. B*, v. 95, p. 125123, Mar 2017.

[69] WENG, Z. Y.; SHENG, D. N.; TING, C. S.; SU, Z. B. One-dimensional large-U Hubbard model: An analytical approach. *Phys. Rev. Lett.*, v. 67, p. 3318, Dec 1991.

[70] WENG, Z. Y.; SHENG, D. N.; TING, C. S.; SU, Z. B. Path-integral approach to the one-dimensional large- U Hubbard model. *Phys. Rev. B*, v. 45, p. 7850, Apr 1992.

[71] OLIVEIRA, M. H.; RAPOSO, E. P.; COUTINHO-FILHO, M. D. AB_2 Hubbard chains in the strong-coupling limit: Ferrimagnetism, Nagaoka and RVB states, phase separation, and Luttinger-liquid behavior. *Phys. Rev. B*, v. 80, p. 205119, Nov 2009.

[72] RIBEIRO, F. G.; COUTINHO-FILHO, M. D. Charge and spin quantum fluctuations in the doped strongly coupled Hubbard model on the honeycomb lattice. *Phys. Rev. B*, v. 92, p. 045105, Jul 2015.

[73] FRADKIN, E. *Field theories of condensed matter physics*. Second. ed. Cambridge University Press, 2013.

[74] NEGELE, J. W.; ORLAND, H. *Quantum many-particle systems*. Frontiers in physics. Addison-Wesley Pub. Co., 1988.

[75] TUNG, W. K. *Group theory in physics*. World Scientific, New York, 1985.

[76] SAKURAI, J. J.; NAPOLITANO, J. *Modern Quantum Mechanics*. 2. ed. Cambridge University Press, 2017.

[77] VITORIANO, C.; BRITO, F. B. D.; RAPOSO, E. P.; COUTINHO-FILHO, M. D. Magnetism of Ferrimagnetic Polymer Chains. *Mol. Cryst. Liq. Cryst*, v. 374, n. 1, p. 185, 2002.

[78] PATI, S. K.; RAMASESHA, S.; SEN, D. Low-lying excited states and low-temperature properties of an alternating spin-1–spin-1/2 chain: A density-matrix renormalization-group study. *Phys. Rev. B*, v. 55, p. 8894, Apr 1997.

[79] YAMAMOTO, S.; BREHMER, S.; MIKESKA, H.-J. Elementary excitations of Heisenberg ferrimagnetic spin chains. *Phys. Rev. B*, v. 57, p. 13610, Jun 1998.

[80] IVANOV, N. B. Magnon dispersions in quantum Heisenberg ferrimagnetic chains at zero temperature. *Phys. Rev. B*, v. 62, p. 3271, Aug 2000.

[81] YAMAMOTO, S. Bosonic representation of one-dimensional Heisenberg ferrimagnets. *Phys. Rev. B*, v. 69, p. 064426, Feb 2004.

[82] DA SILVA, W. M.; MONTENEGRO-FILHO, R. R. Magnetic-field–temperature phase diagram of alternating ferrimagnetic chains: Spin-wave theory from a fully polarized vacuum. *Phys. Rev. B*, v. 96, p. 214419, Dec 2017.

[83] NIGGEMANN, H.; UIMIN, G.; ZITTARTZ, J. Mixed Heisenberg chains: I. The ground-state problem. *J. Phys. Condens. Matter*, v. 9, n. 42, p. 9031, 1997.

[84] BULAEVSKI, L. N.; NAGAEV, E. L.; KHOMSKII, D. I. A new type of autolocalized state of a conduction electron in an antiferromagnetic semiconductor. *Sov. Phys. JETP*, v. 27, p. 836, 1968.

[85] ANDERSON, P. W. The Resonating Valence Bond State in La_2CuO_4 and Superconductivity. *Science*, Washington, v. 235, n. 4793, p. 1196–1198, 1987.

[86] VITORIANO, C.; COUTINHO-FILHO, M. D. Fractional statistics and quantum scaling properties of the integrable Penson-Kolb-Hubbard chain. *Phys. Rev. B*, v. 82, p. 125126, Sep 2010.

[87] VIDAL, J.; DOU ÇcOT, B.; MOSSERI, R.; BUTAUD, P. Interaction Induced Delocalization for Two Particles in a Periodic Potential. *Phys. Rev. Lett.*, v. 85, p. 3906, Oct 2000.

[88] GULÁCSI, Z.; KAMPF, A.; VOLLHARDT, D. Exact Many-Electron Ground States on the Diamond Hubbard Chain. *Phys. Rev. Lett.*, v. 99, p. 026404, Jul 2007.

[89] HATANO, N.; NELSON, D. R. Localization Transitions in Non-Hermitian Quantum Mechanics. *Phys. Rev. Lett.*, v. 77, p. 570, 1996.

[90] CHAKRABARTY, S.; DOBROSAVLJEVI cć, V.; SEIDEL, A.; NUSSINOV, Z. Universality of modulation length and time exponents. *Phys. Rev. E*, v. 86, p. 041132, Oct 2012.

[91] COOPER, B. R.; ELLIOTT, R. J. Spin-Wave Theory of Magnetic Resonance in Spiral Spin Structures: Effect of an Applied Field. *Phys. Rev.*, v. 131, p. 1043, 1963.

[92] A. R. Mackintosh and H. B. Møller, *Spin Waves,* in *Magnetic Properties of Rare Earth Metals,* edited by R. J. Elliott . Plenum Press, 1972.

[93] MARTINEZ ALVAREZ, V. M.; COUTINHO-FILHO, M. D. Itinerant ferrimagnetism on $AB\_\{2\}$ Hubbard chains: Charge and spin quantum fluctuations. *arXiv:1702.03609*, 2018.

[94] NOVOSELOV, K. S.; GEIM, A. K.; MOROZOV, S. V.; JIANG, D.; ZHANG, Y.; DUBONOS, S. V.; GRIGORIEVA, I. V.; FIRSOV, A. A. Electric Field Effect in Atomically Thin Carbon Films. *Science*, Washington, v. 306, n. 5696, p. 666–669, 2004.

[95] GEIM, A. K. Graphene: Status and Prospects. *Science*, Washington, v. 324, n. 5934, p. 1530–1534, 2009.

[96] AVOURIS, P.; XIA, F. Graphene applications in electronics and photonics. *MRS Bulletin*, v. 37, n. 12, p. 1225, 2012.

[97] KANE, C. L.; MELE, E. J. Quantum Spin Hall Effect in Graphene. *Phys. Rev. Lett.*, v. 95, n. 22, p. 226801, Nov. 2005.

[98] KÖNIG, M.; WIEDMANN, S.; BRÜNE, C.; ROTH, A.; BUHMANN, H.; MOLENKAMP, L. W.; QI, X. L.; ZHANG, S. C. Quantum Spin Hall Insulator State in HgTe Quantum Wells. *Science*, Washington, v. 318, n. 5851, p. 766–770, 2007.

[99] KLITZING, K. V.; DORDA, G.; PEPPER, M. New Method for High-Accuracy Determination of the Fine-Structure Constant Based on Quantized Hall Resistance. *Phys. Rev. Lett.*, v. 45, p. 494–497, Aug 1980.

[100] THOULESS, D. J.; KOHMOTO, M.; NIGHTINGALE, M. P.; DEN NIJS, M. Quantized Hall Conductance in a Two-Dimensional Periodic Potential. *Phys. Rev. Lett.*, v. 49, n. 6, p. 405–408, Aug. 1982.

[101] HALDANE, F. Continuum dynamics of the 1-d heisenberg antiferromagnet: Identification with the o(3) nonlinear sigma model". *Physics Letters A*, Amsterdam, v. 93, n. 9, p. 464 – 468, 1983.

[102] HALDANE, F. D. M. Nonlinear Field Theory of Large-Spin Heisenberg Antiferromagnets: Semiclassically Quantized Solitons of the One-Dimensional Easy-Axis Néel State. *Phys. Rev. Lett.*, v. 50, p. 1153–1156, Apr 1983.

[103] HASAN, M. Z.; KANE, C. L. *Colloquium* : Topological insulators. *Rev. Mod. Phys.*, v. 82, n. 4, p. 3045, Nov. 2010.

[104] NAKAHARA, M. *Geometry, topology and physics*. Second. ed. CRC Press, 2017.

[105] QI, X.-L.; ZHANG, S.-C. Topological insulators and superconductors. *Rev. Mod. Phys.*, v. 83, p. 1057–1110, Oct 2011.

[106] ASBÓTH, J. K.; OROSZLÁNY, L.; PÁLYI, A. *A Short Course on Topological Insulators*. Cham: Springer International Publishing, 2016. v. 919 of *Lecture Notes in Physics*.

[107] LAUGHLIN, R. B. Quantized hall conductivity in two dimensions. *Phys. Rev. B*, v. 23, p. 5632–5633, May 1981.

[108] FOR PHYSICS OF THE ROYAL SWEDISH ACADEMY OF SCIENCES, C. *Scientific background: Topological phase transitions and topological phases of matter*. 2016.

[109] VANDERBILT, D. *Berry Phases in Electronic Structure Theory: Electric Polarization, Orbital Magnetization and Topological Insulators*. Cambridge University Press, 2018.

[110] PRANGE, R.; GIRVIN, S. M. *The Quantum Hall effect*. Springer-Verlag, New York, 2nd ed., 1990.

[111] WEN, X.-G. Topological orders and edge excitations in fractional quantum Hall states. *Adv. Phys.*, v. 44, n. 5, p. 405–473, 1995.

[112] KANE, C. L.; MELE, E. J. Z_2 Topological Order and the Quantum Spin Hall Effect. *Phys. Rev. Lett.*, v. 95, p. 146802, Sep 2005.

[113] OKA, T.; AOKI, H. Photovoltaic Hall effect in graphene. *Phys. Rev. B*, v. 79, p. 081406, Feb 2009.

[114] LINDNER, N. H.; REFAEL, G.; GALITSKI, V. Floquet topological insulator in semiconductor quantum wells. *Nat. Phys.*, v. 7, n. 6, p. 490–495, June 2011.

[115] FOA TORRES, L. E. F.; PEREZ-PISKUNOW, P. M.; BALSEIRO, C. A.; USAJ, G. Multiterminal Conductance of a Floquet Topological Insulator. *Phys. Rev. Lett.*, v. 113, p. 266801, Dec 2014.

[116] ATALA, M.; AIDELSBURGER, M.; BARREIRO, J. T.; ABANIN, D.; KITAGAWA, T.; DEMLER, E.; BLOCH, I. Direct measurement of the Zak phase in topological Bloch bands. *Nature Physics*, v. 9, n. 12, p. 795–800, Dec. 2013.

[117] JOTZU, G.; MESSER, M.; DESBUQUOIS, R.; LEBRAT, M.; UEHLINGER, T.; GREIF, D.; ESSLINGER, T. Experimental realization of the topological Haldane model with ultracold fermions. *Nature*, London, v. 515, n. 7526, p. 237–240, Nov. 2014.

[118] HAFEZI, M.; DEMLER, E. A.; LUKIN, M. D.; TAYLOR, J. M. Robust optical delay lines with topological protection. *Nat. Phys.*, v. 7, n. 11, p. 907, 2011.

[119] RECHTSMAN, M. C.; ZEUNER, J. M.; PLOTNIK, Y.; LUMER, Y.; PODOLSKY, D.; DREISOW, F.; NOLTE, S.; SEGEV, M.; SZAMEIT, A. Photonic Floquet topological insulators. *Nature*, London, v. 496, n. 7444, p. 196, 2013.

[120] OZAWA, T.; PRICE, H. M.; AMO, A.; GOLDMAN, N.; HAFEZI, M.; LU, L.; RECHTSMAN, M.; SCHUSTER, D.; SIMON, J.; ZILBERBERG, O. et al. Topological photonics. *arXiv:1802.04173*, 2018.

[121] HALDANE, F. D. M. Model for a Quantum Hall Effect without Landau Levels: Condensed-Matter Realization of the "Parity Anomaly". *Phys. Rev. Lett.*, v. 61, n. 18, p. 2015–2018, Oct. 1988.

[122] HSIEH, D.; QIAN, D.; WRAY, L.; XIA, Y.; HOR, Y. S.; CAVA, R. J.; HASAN, M. Z. A topological Dirac insulator in a quantum spin Hall phase. *Nature*, London, v. 452, n. 7190, p. 970–974, apr 2008.

[123] LANG, L.-J.; CAI, X.; CHEN, S. Edge States and Topological Phases in One-Dimensional Optical Superlattices. *Phys. Rev. Lett.*, v. 108, p. 220401, May 2012.

[124] GUO, H.; CHEN, S. Kaleidoscope of symmetry-protected topological phases in one-dimensional periodically modulated lattices. *Phys. Rev. B*, v. 91, p. 041402, Jan 2015.

[125] KRAUS, Y. E.; LAHINI, Y.; RINGEL, Z.; VERBIN, M.; ZILBERBERG, O. Topological States and Adiabatic Pumping in Quasicrystals. *Phys. Rev. Lett.*, v. 109, p. 106402, Sep 2012.

[126] KE, Y.; QIN, X.; MEI, F.; ZHONG, H.; KIVSHAR, Y. S.; LEE, C. Topological phase transitions and Thouless pumping of light in photonic waveguide arrays. *Laser Photon. Rev.*, v. 10, n. 6, p. 995–1001, 2016.

[127] SHECHTMAN, D.; BLECH, I.; GRATIAS, D.; CAHN, J. W. Metallic Phase with Long-Range Orientational Order and No Translational Symmetry. *Phys. Rev. Lett.*, v. 53, p. 1951–1953, Nov 1984.

[128] MADSEN, K. A.; BERGHOLTZ, E. J.; BROUWER, P. W. Topological equivalence of crystal and quasicrystal band structures. *Phys. Rev. B*, v. 88, p. 125118, Sep 2013.

[129] HE, Y.; WRIGHT, K.; KOUACHI, S.; CHIEN, C.-C. Topology, edge states, and zero-energy states of ultracold atoms in one-dimensional optical superlattices with alternating on-site potentials or hopping coefficients. *Phys. Rev. A*, v. 97, p. 023618, Feb 2018.

[130] VERBIN, M.; ZILBERBERG, O.; KRAUS, Y. E.; LAHINI, Y.; SILBERBERG, Y. Observation of Topological Phase Transitions in Photonic Quasicrystals. *Phys. Rev. Lett.*, v. 110, p. 076403, Feb 2013.

[131] VERBIN, M.; ZILBERBERG, O.; LAHINI, Y.; KRAUS, Y. E.; SILBERBERG, Y. Topological pumping over a photonic Fibonacci quasicrystal. *Phys. Rev. B*, v. 91, p. 064201, Feb 2015.

[132] KITAGAWA, T.; RUDNER, M. S.; BERG, E.; DEMLER, E. Exploring topological phases with quantum walks. *Phys. Rev. A*, v. 82, p. 033429, Sep 2010.

[133] WANG, L.; LIU, N.; CHEN, S.; ZHANG, Y. Quantum walks in the commensurate off-diagonal Aubry-André-Harper model. *Phys. Rev. A*, v. 95, p. 013619, Jan 2017.

[134] MOURIK, V.; ZUO, K.; FROLOV, S. M.; PLISSARD, S. R.; BAKKERS, E. P. A. M.; KOUWENHOVEN, L. P. Signatures of Majorana fermions in hybrid superconductor-semiconductor nanowire devices. *Science*, Washington, v. 336, n. 6084, p. 1003–1007, 2012.

[135] DAS, A.; RONEN, Y.; MOST, Y.; OREG, Y.; HEIBLUM, M.; SHTRIKMAN, H. Zero-bias peaks and splitting in an Al–InAs nanowire topological superconductor as a signature of Majorana fermions. *Nat. Phys.*, v. 8, n. 12, p. 887, 2012.

[136] NADJ-PERGE, S.; DROZDOV, I. K.; LI, J.; CHEN, H.; JEON, S.; SEO, J.; MACDONALD, A. H.; BERNEVIG, B. A.; YAZDANI, A. Observation of majorana fermions in ferromagnetic atomic chains on a superconductor. *Science*, Washington, p. 1259327, 2014.

[137] JIN, L. Topological phases and edge states in a non-Hermitian trimerized optical lattice. *Phys. Rev. A*, v. 96, p. 032103, Sep 2017.

[138] LIU, X.; AGARWAL, G. S. The New Phases due to Symmetry Protected Piecewise Berry Phases; Enhanced Pumping and Non-reciprocity in Trimer Lattices. *Sci. Rep.*, v. 7, p. 45015, 2017.

[139] HUDA, M. N.; KEZILEBIEKE, S.; OJANEN, T.; DROST, R.; LILJEROTH, P. Tuneable topological domain wall states in engineered atomic chains. *arXiv:1806.08614*, 2018.

[140] LEE, T. E. Anomalous Edge State in a Non-Hermitian Lattice. *Phys. Rev. Lett.*, v. 116, n. 13, p. 133903, 2016.

[141] XIONG, Y. Why does bulk boundary correspondence fail in some non-Hermitian topological models. *Journal of Physics Communications*, v. 2, n. 3, p. 035043, 2018.

[142] MARTINEZ ALVAREZ, V. M.; BARRIOS VARGAS, J. E.; FOA TORRES, L. E. F. Non-Hermitian robust edge states in one dimension: Anomalous localization and eigenspace condensation at exceptional points. *Phys. Rev. B*, v. 97, p. 121401, Mar 2018.

[143] GONG, Z.; ASHIDA, Y.; KAWABATA, K.; TAKASAN, K.; HIGASHIKAWA, S.; UEDA, M. Topological Phases of Non-Hermitian Systems. *Phys. Rev. X*, v. 8, p. 031079, Sep 2018.

[144] MARTINEZ ALVAREZ, V. M.; BARRIOS VARGAS, J. E.; BERDAKIN, M.; FOA TORRES, L. E. F. Topological states of non-Hermitian systems. *Eur. Phys. J. Spec. Top.*, v. 227, p. 1295, Oct 2018.

[145] GARANOVICH, I. L.; LONGHI, S.; SUKHORUKOV, A. A.; KIVSHAR, Y. S. Light propagation and localization in modulated photonic lattices and waveguides. *Physics Reports*, v. 518, n. 1, p. 1 – 79, 2012.

[146] ZAK, J. Berry's phase for energy bands in solids. *Phys. Rev. Lett.*, v. 62, p. 2747–2750, Jun 1989.

[147] DELPLACE, P.; ULLMO, D.; MONTAMBAUX, G. Zak phase and the existence of edge states in graphene. *Phys. Rev. B*, v. 84, p. 195452, Nov 2011.

[148] SU, W. P.; SCHRIEFFER, J. R.; HEEGER, A. J. Solitons in Polyacetylene. *Phys. Rev. Lett.*, v. 42, p. 1698–1701, Jun 1979.

[149] PENG, Y.; BAO, Y.; VON OPPEN, F. Boundary Green functions of topological insulators and superconductors. *Phys. Rev. B*, v. 95, p. 235143, Jun 2017.

[150] SCHNYDER, A. P.; RYU, S.; FURUSAKI, A.; LUDWIG, A. W. W. Classification of topological insulators and superconductors in three spatial dimensions. *Phys. Rev. B*, v. 78, p. 195125, Nov 2008.

[151] KITAEV, A. Periodic table for topological insulators and superconductors. *AIP Conf. Proc.*, v. 1134, n. 1, p. 22, 2009.

[152] RYU, S.; SCHNYDER, A. P.; FURUSAKI, A.; LUDWIG, A. W. W. Topological insulators and superconductors: tenfold way and dimensional hierarchy. *New J. Phys.*, v. 12, n. 6, p. 065010, 2010.

[153] LIEU, S. Topological phases in the non-Hermitian Su-Schrieffer-Heeger model. *Phys. Rev. B*, v. 97, p. 045106, Jan 2018.

[154] YUCE, C. Edge states at the interface of non-hermitian systems. *Phys. Rev. A*, v. 97, p. 042118, Apr 2018.

[155] HUGHES, T. L.; PRODAN, E.; BERNEVIG, B. A. Inversion-symmetric topological insulators. *Phys. Rev. B*, v. 83, p. 245132, Jun 2011.

[156] RHIM, J.-W.; BEHRENDS, J.; BARDARSON, J. H. Bulk-boundary correspondence from the intercellular Zak phase. *Phys. Rev. B*, v. 95, p. 035421, Jan 2017.

[157] SHEN, S. Q. *Topological Insulators: Dirac Equation in Condensed Matter*. Springer, Berlin, Germany, 2012.

[158] THOULESS, D. J. Quantization of particle transport. *Phys. Rev. B*, v. 27, p. 6083, May 1983.

[159] HARPER, P. G. Single band motion of conduction electrons in a uniform magnetic field. *Proc. Phys. Soc. A*, v. 68, n. 10, p. 874, 1955.

[160] AUBRY, S.; ANDRÉ, G. Analyticity breaking and Anderson localization in incommensurate lattices. *Ann. Israel Phys. Soc*, v. 3, n. 133, p. 18, 1980.

[161] KRAUS, Y. E.; ZILBERBERG, O. Topological Equivalence between the Fibonacci Quasicrystal and the Harper Model. *Phys. Rev. Lett.*, v. 109, p. 116404, Sep 2012.

[162] MARTINEZ ALVAREZ, V. M.; COUTINHO-FILHO, M. D. Edge states in trimer lattices. *Phys. Rev. A*, v. 99, p. 013833, Jan 2019.

APÊNDICE A – PERTURBATIVE EXPANSION OF $\mathcal{L}_n(\tau)$

In this appendix we present the main steps of the derivation of the perturbative expansion of $\mathcal{L}_n$, in Eq. (2.30), up to $\mathcal{O}(J)$. In direct connection with the transformations in Eq. (2.35), it is convenient to define rotation matrices either symmetric or antisymmetric with respect to the exchange operation $B_1 \leftrightarrow B_2$:

$$\begin{aligned} U_i^{(b)} &= U_{iA}, \\ U_i^{(d,e)} &= \frac{1}{\sqrt{2}}(U_{iB_1} \pm U_{iB_2}), \end{aligned} \tag{A.1}$$

In the sequence, by substituting both the above transformations and its analogous in Eq. (2.35) into Eq. (2.30), we find that $\mathcal{L}_n(\tau)$ can be written as the sum of the following nine terms

$$\mathcal{L}_n(\tau) = \mathcal{L}_n^{(1)} + \mathcal{L}_n^{(2)} + \mathcal{L}_n^{(3)} + \mathcal{L}_n^{(4)} + \mathcal{L}_n^{(5)} + \mathcal{L}_n^{(6)} + \mathcal{L}_n^{(7)} + \mathcal{L}_n^{(8)} + \mathcal{L}_n^{(9)}, \tag{A.2}$$

where

$$\begin{aligned} \mathcal{L}_n^{(1)} &= \sum_{i\sigma\sigma'} b_{i\sigma'}^\dagger (U_i^{(b)\dagger}\partial_\tau U_i^{(b)})_{\sigma'\sigma} b_{i\sigma}, \\ \mathcal{L}_n^{(2)} &= \frac{1}{2}\sum_{i\sigma\sigma'} d_{i\sigma'}^\dagger \left[U_i^{(d)\dagger}\partial_\tau U_i^{(d)} + U_i^{(e)\dagger}\partial_\tau U_i^{(e)}\right] d_{i\sigma}, \\ \mathcal{L}_n^{(3)} &= \frac{1}{2}\sum_{i\sigma\sigma'} e_{i\sigma'}^\dagger \left[U_i^{(d)\dagger}\partial_\tau U_i^{(d)} + U_i^{(e)\dagger}\partial_\tau U_i^{(e)}\right] e_{i\sigma} \\ \mathcal{L}_n^{(4)} &= \frac{1}{2}\sum_{i\sigma\sigma'} d_{i\sigma'}^\dagger \left[U_i^{(d)\dagger}\partial_\tau U_i^{(e)} + U_i^{(e)\dagger}\partial_\tau U_i^{(d)}\right] e_{i\sigma} \\ \mathcal{L}_n^{(5)} &= \frac{1}{2}\sum_{i\sigma\sigma'} e_{i\sigma'}^\dagger \left[U_i^{(d)\dagger}\partial_\tau U_i^{(e)} + U_i^{(e)\dagger}\partial_\tau U_i^{(d)}\right] d_{i\sigma}, \\ \mathcal{L}_n^{(6)} &= -t\sum_{i\sigma\sigma'} \left[b_{i\sigma'}^\dagger \left(U_i^{(b)\dagger}U_i^{(d)} - \sqrt{2}\right)_{\sigma'\sigma} d_{i\sigma} + \text{H.c.}\right], \\ \mathcal{L}_n^{(7)} &= -t\sum_{i\sigma\sigma'} \left[b_{i\sigma'}^\dagger \left(U_i^{(b)\dagger}U_i^{(e)}\right)_{\sigma'\sigma} e_{i\sigma} + \text{H.c.}\right], \\ \mathcal{L}_n^{(8)} &= -t\sum_{i\sigma\sigma'} \left[d_{i\sigma'}^\dagger \left(U_i^{(d)\dagger}U_{i+1}^{(b)} - \sqrt{2}\right)_{\sigma'\sigma} b_{i+1\sigma} + \text{H.c.}\right], \\ \mathcal{L}_n^{(9)} &= -t\sum_{i\sigma\sigma'} \left[e_{i\sigma'}^\dagger \left(U_i^{(e)\dagger}U_{i+1}^{(b)}\right)_{\sigma'\sigma} b_{i+1\sigma} + \text{H.c.}\right]. \end{aligned}$$

Now, by inserting the expansions (2.49) and (2.50) into the above Lagrangians, and neglecting terms containing exclusively fields related to the high-energy bands, $\mathcal{L}_n(\tau)$

can be written in terms of the spinless Grassmann fields in a perturbative expansion up to order J as follows

$$\mathcal{L}_n^{(1)} = \sum_{i\sigma} \theta(-\sigma)(U_i^{(b)\dagger}\partial_\tau U_i^{(b)})_{\sigma,\sigma}\alpha_i^{(\frac{1}{2})\dagger}\alpha_i^{(\frac{1}{2})}, \tag{A.3}$$

$$\mathcal{L}_n^{(2)} = \sum_{i\sigma;\nu=d,e} \frac{\theta(\sigma)}{2}(U_i^{(\nu)\dagger}\partial_\tau U_i^{(\nu)})_{\sigma,\sigma}\alpha_i^\dagger\alpha_i, \tag{A.4}$$

$$\mathcal{L}_n^{(3)} = \sum_{i\sigma,\nu=d,e} \frac{\theta(\sigma)}{2}(U_i^{(\nu)\dagger}\partial_\tau U_i^{(\nu)})_{\sigma,\sigma}e_{i\uparrow}^\dagger e_{i\uparrow}, \tag{A.5}$$

$$\mathcal{L}_n^{(4)} = \sum_{\substack{i\sigma;\nu,\nu'=d,e \\ \nu\neq\nu'}} \frac{\theta(\sigma)}{2}(U_i^{(\nu)\dagger}\partial_\tau U_i^{(\nu')})_{\sigma,\sigma}\alpha_i^\dagger e_{i\uparrow}, \tag{A.6}$$

$$\mathcal{L}_n^{(5)} = [\mathcal{L}_n^{(4)}]^\dagger, \tag{A.7}$$

$$\begin{aligned}\mathcal{L}_n^{(6)} = &-\sum_{i\sigma\sigma'}\left(U_i^{(b)\dagger}U_i^{(d)} - \sqrt{2}\right)_{\sigma,\sigma'}\Big\{t\delta_{\sigma',\sigma}[\theta(-\sigma)\alpha_i^{(\frac{1}{2})\dagger}\beta_i \\ &- \theta(\sigma)\beta_i^{(\frac{1}{2})\dagger}\alpha_i] + t\theta(-\sigma)\delta_{\sigma',-\sigma}\alpha_i^{(\frac{1}{2})\dagger}\alpha_i \\ &+ \sqrt{2}\frac{t^2}{U}\delta_{\sigma',\sigma}\Big[\theta(-\sigma)\alpha_i^{(\frac{1}{2})\dagger}(\alpha_i^{(\frac{1}{2})} + \alpha_{i+1}^{(\frac{1}{2})}) \\ &+\theta(\sigma)(\alpha_i^\dagger + \alpha_{i-1}^\dagger)\alpha_i\Big] + \text{H.c.}\Big\},\end{aligned} \tag{A.8}$$

$$\begin{aligned}\mathcal{L}_n^{(7)} = &-\sum_{i\sigma\sigma'}\left(U_i^{(b)\dagger}U_i^{(e)}\right)_{\sigma,\sigma'}\Big\{t\theta(-\sigma)\delta_{\sigma',-\sigma}\alpha_i^{(\frac{1}{2})\dagger}e_{i\uparrow} \\ &+ t\delta_{\sigma',\sigma}[\theta(-\sigma)\alpha_i^{(\frac{1}{2})\dagger}e_{i\downarrow} - \theta(\sigma)\beta_i^{(\frac{1}{2})\dagger}e_{i\uparrow}] \\ &+\sqrt{2}\frac{t^2}{U}\delta_{\sigma',\sigma}\theta(\sigma)(\alpha_i^\dagger + \alpha_{i-1}^\dagger)e_{i\uparrow} + \text{H.c.}\Big\},\end{aligned} \tag{A.9}$$

$$\begin{aligned}\mathcal{L}_n^{(8)} = &-\sum_{i\sigma\sigma'}\left(U_i^{(d)\dagger}U_{i+1}^{(b)} - \sqrt{2}\right)_{\sigma,\sigma'}\Big\{t\delta_{\sigma',\sigma}[\theta(-\sigma)\beta_i^\dagger\alpha_{i+1}^{(\frac{1}{2})} \\ &- \theta(\sigma)\alpha_i^\dagger\beta_{i+1}^{(\frac{1}{2})}] + t\theta(\sigma)\delta_{\sigma',-\sigma}\alpha_i^\dagger\alpha_{i+1}^{(\frac{1}{2})} \\ &+ \sqrt{2}\frac{t^2}{U}\delta_{\sigma',\sigma}\Big[\theta(\sigma)\alpha_i^\dagger(\alpha_i + \alpha_{i+1}) \\ &+\theta(-\sigma)(\alpha_i^{(\frac{1}{2})\dagger} + \alpha_{i+1}^{(\frac{1}{2})\dagger})\alpha_{i+1}^{(\frac{1}{2})}\Big] + \text{H.c.}\Big\},\end{aligned} \tag{A.10}$$

$$\begin{aligned}\mathcal{L}_n^{(9)} = &-\sum_{i\sigma\sigma'}\left(U_i^{(e)\dagger}U_{i+1}^{(b)}\right)_{\sigma,\sigma'}\Big\{t\theta(\sigma)\delta_{\sigma',-\sigma}e_{i\uparrow}^\dagger\alpha_{i+1}^{(\frac{1}{2})} \\ &+ t\delta_{\sigma',\sigma}[\theta(-\sigma)e_{i\downarrow}^\dagger\alpha_{i+1}^{(\frac{1}{2})} - \theta(\sigma)e_{i\uparrow}^\dagger\beta_{i+1}^{(\frac{1}{2})}] \\ &+\sqrt{2}\frac{t^2}{U}\delta_{\sigma',\sigma}\theta(\sigma)e_{i\uparrow}^\dagger(\alpha_i + \alpha_{i+1}) + \text{H.c.}\Big\}.\end{aligned} \tag{A.11}$$

We remark that, in Eqs. (A.3)-(A.7) multiplicative terms of $\mathcal{O}(t/U)$ were neglected, since $(U_i^{(\nu)\dagger}\partial_\tau U_i^{(\nu)})_{\sigma,\sigma}$ scale with J [see Eq. (3.2)]. However, as we can see in the above equations, terms allowing interband transitions between low- and high-energy bands do exist in $\mathcal{L}_n$. In the following, we present the perturbative scheme (69, 71, 72) suitable to eliminate the referred high-energy states.

We consider that in the unperturbed ferrimagnetic state $|\Phi_0(N)\rangle$ at half-filled band ($N_e = N$ electrons) and total energy $E_0(N)$, the low-energy electronic modes (α_k,$e_{k\uparrow}$) are filled, while the high-energy (β_k,$e_{k\downarrow}$) ones are empty. In the context of a second-order Rayleigh-Schrödinger perturbation theory, consistent with the strong-coupling expansion up to $\mathcal{O}(t^2/U)$, the virtual excited states $|\gamma_k,\sigma\rangle$ contain $N-1$ electrons in the low-energy bands and one electron with spin σ promoted to a high-energy band, either β [with energy $E_k^\gamma = E_0(N-1) + E_k + U/2$] or $e_{k\downarrow}$ [with $E_k^\gamma = E_0(N-1) + U$]. Contributions to the perturbative Hamiltonian H_1 (see below) are thus generated from terms in Eqs. (A.8)-(A.11). Therefore, the energy shift or effective Hamiltonian, derived through

$$\Delta E = \sum_{k\sigma} \frac{\langle \Phi_0 | H_1 | \gamma_k,\sigma \rangle \langle \gamma_k,\sigma | H_1 | \Phi_0 \rangle}{E_0 - E_k^\gamma} \rightarrow \mathcal{H}_{eff}, \tag{A.12}$$

is identical to Eq. (2.56d), after cancellation of extra contributions from ΔE and the last terms of Eqs. (A.8)-(A.11), so that the remained terms in Eq. (2.56d) give rise to the quantum Heisenberg model at half filling in Chapter. (3).

Under the above scheme, the perturbative expansion of $\mathcal{L}_n(\tau)$ obtains in terms of lower-energy bands only, whose sum with $\mathcal{L}_0(\tau)$, Eq. (2.54), results in $\mathcal{L}_{eff}(\tau)$, Eq. (2.55).

APÊNDICE B – RECURSIVE BOUNDARY GREEN FUNCTION

In order to investigate the localization properties of the edge states and their relationship with the relative strength of the inter-and intra-cell hopping amplitudes of the trimer lattice Hamiltonian, in this Appendix we apply the recursive boundary Green function method which relates the presence or absence of edge states to the fixed points of the recursion (149).

Following the scheme laid out in Ref. (149), we can extend the system by adding sites until we obtain a trimer with N_c unit cells. This can be achieved in two ways, either by extending the system to the right or to the left. In any case, considering that the chain is long enough (large N_c limit), we expect that the boundary Green function becomes independent of the number of unit cells, but not on the specific boundary. Indeed, as we show next, in the inversion-symmetry broken phase of the trimer lattice, the right and left boundary Green functions behave differently.

The boundary Green function G_{3N_c} of a trimer chain with $3N_c$ sites can be related to the boundary Green function G_{3N_c-1} of a chain with $3N_c-1$ sites through the Dyson equation:

$$(g_{3N_c}^{-1} - V_{3N_c-1} G_{3N_c-1} V_{3N_c-1}^{\dagger}) G_{3N_c} = \mathbb{I}, \tag{B.1}$$

where $g_{3N_c}^{-1} = \mathbb{I}\varepsilon$ is the bare Green function and V_{3N_c-1} is associated with the hopping terms u, v and w. In this way, by iterating (three times) the recursion Eq. (B.1) from the right boundary we obtain a recursion for trimer chains with a number of sites multiple of three:

$$G_{3N_c}^{R} = \left(\varepsilon - v^2(\varepsilon - u^2(\varepsilon - w^2 G_{3N_c-3}^{R})^{-1})^{-1}\right)^{-1}. \tag{B.2}$$

Analogously, we can study the appearance of edges states localized on the left boundary of the trimer lattice by iterating (also three times) the recursion Eq. (B.1) from the left boundary

$$G_{3N_c}^{L} = \left(\varepsilon - u^2(\varepsilon - v^2(\varepsilon - w^2 G_{3N_c-3}^{L})^{-1})^{-1}\right)^{-1}. \tag{B.3}$$

Notice that the above equation can be obtained from Eq. (B.2) through the exchange $u \leftrightarrow v$. In what follows, we will describe how to obtain the right boundary Green function (G^R) and then extend the results to the left boundary Green function (G^L) through the exchange $u \leftrightarrow v$.

It is convenient to rewrite the recursion Eq. (B.2) as $G_{3N_c}^{R} - G_{3N_c-3}^{R} = \beta(G_{3N_c-3}^{R})$, where the β function is given by

$$\beta(x) = \left(\varepsilon - v^2(\varepsilon - u^2(\varepsilon - w^2 x)^{-1})^{-1}\right)^{-1} - x. \tag{B.4}$$

The zeros of the β function define the fixed-point boundary Green function. One can write the solution for the above quadratic equation as follows:

$$x = \frac{\varepsilon(w^2 - u^2 + \varepsilon^2 - v^2)}{2w^2(\varepsilon^2 - v^2)} \pm \sqrt{\left(\frac{\varepsilon(w^2 - u^2 + \varepsilon^2 - v^2))}{2w^2(\varepsilon^2 - v^2)}\right)^2 - \frac{(\varepsilon^2 - u^2)}{w^2(\varepsilon^2 - v^2)}}, \tag{B.5}$$

and making an expansion in power series of $(\varepsilon \pm v)$ we obtain

$$G^R_{\text{regular}} = \pm\frac{u^2 - 4v^2 - w^2}{8vw^2} + \mathcal{O}(\varepsilon \pm v), \tag{B.6}$$

$$G^R_{\text{singular}} = \frac{(w^2 - u^2)}{2w^2(\varepsilon \pm v)} \pm \frac{u^2 - 4v^2 - w^2}{8vw^2} + \mathcal{O}(\varepsilon \pm v). \tag{B.7}$$

The above regular and singular (right) boundary Green functions characterize the absence and presence of edge states localized on the right boundary of the system, respectively. In fact, the two poles $\varepsilon = \pm v$ of the singular boundary Green function indicate the energies of the edge states.

We know that a fixed point is stable when $\beta'(x) < 0$. Then, the region of the parameter space where edge states appear can be analyzed by studying the stability of the fixed-point Green functions under the recursion, which leads to

$$\beta'(G^R_{\text{regular}})\Big|_{\varepsilon=\pm v} = \frac{w^2}{u^2} - 1, \tag{B.8}$$

$$\beta'(G^R_{\text{singular}})\Big|_{\varepsilon=\pm v} = \frac{u^2}{w^2} - 1. \tag{B.9}$$

The emergence of edge states located at the right (left) boundary of the trimer lattice, with energies $\varepsilon = \pm v$ ($\varepsilon = \pm u$), are characterized by the singular boundary Green function G^R_{singular} (G^L_{singular}), which is stable for $|u| < |w|$ ($|v| < |w|$). On the other hand, the regular boundary Green function G^R_{regular} (G^L_{regular}), is stable for $|w| < |u|$ ($|w| < |v|$), which means that there are no edge states located at the right (left) boundary of the trimer lattice in this region of parameter space.

We conclude this Appendix by mentioning that the above results fully support the findings reported in Section 6.2.